The Mediterranean Journal of Measurement and Control

Volume 5 / Number 1 / 2009

ISSN: 1743-9310

Published by SoftMotor Ltd.

The Mediterranean Journal of Measurement and Control

Aims and Scope

The journal publishes papers from worldwide in the field of instrumentation, measurement, and control. Its scope encompasses cutting-edge research and development, education and industrial applications. The journal publishes peer-reviewed papers designed to appeal to both researchers and practitioners. It presents up-to-date coverage of the latest developments, offering a unique interdisciplinary perspective. It also includes invited papers, book reviews, conference notices, calls for papers, and announcements of new publications and special issues. The journal covers - but not limited to: All Aspects of Control Theory and its Applications (Linear, Nonlinear, Robust, State Space and Multivariable, Self-Tuning, Adaptive, Optimal, and others), System Identification and Parameter Estimation, and Mathematical Modeling and Simulation, Intelligent Systems and Applications (fuzzy logic, neural networks, genetic algorithms, and others), Machine Vision and Pattern Recognition, Mechatronics and Robotics, and Advanced Manufacturing Systems, Sensors, Measuring Instruments, and Signal Processing, Computing for Measurement, Control and Automation, and Industrial Networks and Communication protocols (FieldBuses, OPC, and others). Papers may be from the following categories: Design: Present a complete “how-to” guide. Connect design procedures to first principles. Explicitly state necessary heuristics and limits of applicability. Provide evidence that the procedures are practicable. Analysis: Clearly develop a fundamental, theoretical analysis of a practice-relevant issue. Explicitly state implications and recommendations for its application. Provide credible examples. Application: Present the results of new (or under-utilized) techniques or novel applications. Provide a complete description of results, including pilot- or plant-scale experimental data, and a revelation of heuristics and shortcomings.

WELCOME TO THE MEDITERRANEAN JOURNAL OF MEASUREMENT AND CONTROL

We would like to welcome you all to the fifth volume - first issue - of The Mediterranean Journal of Measurement and Control. This issue of the journal, comprising of five papers, is dedicated to the latest research work being done in the analyses of modeling and control of dynamic systems, power control, enhanced measurements, and artificial intelligence.

The first paper by Chen deals with sinusoidal model fitting that plays an important role in measuring the effective number of bits of an ADC. However, the most attractive fitting, four-parameter sine wave fitting based on the least square error principle, is nonlinear. An iterative approach to such a problem necessitates the initial frequency. In this paper, the complication of inappropriate initial values was reviewed firstly, and then an explicit approach was presented to obtain the initial frequency. This new approach makes use of three spectrum lines around the main lobe of the fast Fourier transform (FFT) and can work with a short record. Finally, it was tested by simulation signals contaminated with different levels of noise, with the lowest signal-to-noise being -3.01dB. The results from noise-free cases indicate that the frequency error of the proposed approach is no greater than 0.0006 times of the FFT resolution. Regarding to the noise cases, insofar as the simulated trials, the average difference between the empirical variance and the Cramer-Rao bound (CRB) is less than four dBs. The CRB can be reached after only one round of iteration starting from the initial frequency obtained from the proposed approach.

The second paper by Lourci deals with the stability problem of the input DC voltages in a five levels diode clamped inverter which is recalled and illustrated in this paper. A knowledge model of this converter using switching functions and a space vector PWM strategy is demonstrated in detail. To investigate the instability problem of the input DC voltages of the inverter, authors studied a cascade constituted by a two levels rectifier - five levels diode clamped inverter - induction motor. To solve this problem, the rectifier output voltage has been stabilized using the sliding mode control, while balancing the input DC voltages of the five levels diode clamped inverter by using redundant vectors of the space vector PWM strategy. The obtained results show the effectiveness of this method which can be used to stabilize the input DC voltages of the multilevel converters.

The third paper by Benghanem develops an explicit model for accurate simulation of the I-V characteristic of photovoltaic (PV) cells and modules under various climatic conditions is described. The proposed model is found to be reliable and accurate in the situations where the model is a good approximation of cell or module performance. The developed model has been compared with the traditional I-V characteristic and with some experimental results. The obtained results showed the effectiveness of the proposed model. Moreover, an experimental method is proposed to determine the series resistance and shunt resistance of the PV cells and modules.

The fourth paper by Saadaoui deals with PID controller design for time delay systems using genetic algorithms, where stabilizing regions of a PID controller applied to a class of time delay systems are computed using parametric methods. A necessary condition is used to obtain the admissible ranges of proportional and derivative gains. Then, for a fixed value of one of these parameters within this admissible range, stabilizing regions in the space of the remaining two parameters are determined. Stabilization being the most basic requirement in any controller design problem, once this property is guaranteed, a search among these stabilizing controllers those that satisfy other performance specifications can be established. This step is carried out using the genetic algorithm optimization method. Time domain measures of the closed loop system such as maximum percent overshoot, rise time and settling time are minimized using genetic algorithms and the stabilizing regions of the PID controller values. Examples are given to demonstrate the effectiveness of this proposed approach.

Finally, the fifth paper by Yeung proposes a decentralised controller design procedure for weakly coupled systems. A key feature of the design method is that the problem of designing a complete decentralised controller is replaced by several simpler local design problems. This is achieved by introducing a decomposition condition, which imposes local design constraints. This means that the design of each local controller is completely decoupled from other controllers. This has both design, and computational benefits. For the design, as long as each local controller satisfies the local decomposition condition, its design will be independent of the other controllers. In turn, this facilitates tuning and commissioning of the controller and the various design stages such as the choice of weighting functions. Most importantly this means that each of the loop-controllers is locally tunable. To achieve this, the decomposition condition is combined into a set of linear matrix inequalities (LMIs), then a sub-optimal robust solution for this type of control problem is obtained. The approach has been applied to several numerical examples and used for a case study of a gas turbine engine controller design.

January 2009

Dr. Mohamed H. Mahmoud
Editor-in-Chief

AN APPROACH TO INITIALIZE FOUR-PARAMETER SINE WAVE FITTING

K. F. Chen

College of Sciences, China Agricultural University, P. R. China

ABSTRACT

Sinusoidal model fitting plays an important role in measuring the effective number of bits of an ADC. However, the most attractive fitting, four-parameter sine wave fitting based on the least square error principle, is nonlinear. An iterative approach to such a problem necessitates the initial frequency. In this paper, the complication of inappropriate initial values was reviewed firstly, and then an explicit approach was presented to obtain the initial frequency. This new approach makes use of three spectrum lines around the main lobe of the fast Fourier transform (FFT) and can work with a short record. Finally, it was tested by simulation signals contaminated with different levels of noise, with the lowest signal-to-noise being -3.01dB. The results from noise-free cases indicate that the frequency error of the proposed approach is no greater than 0.0006 times of the FFT resolution. Regarding to the noise cases, insofar as the simulated trials, the average difference between the empirical variance and the Cramer-Rao bound (CRB) is less than four dBs. The CRB can be reached after only one round of iteration starting from the initial frequency obtained from the proposed approach.

Keywords

Four-Parameter Sine Wave, Least Square Error, Fast Fourier Transform (FFT), Cramer-Rao Bound, Analog-to-Digital Converter, Iteration.

1. INTRODUCTION

Fitting sinusoidal models to recorded data plays an important role in several communities, e.g., in connection with analog-to-digital converters (ADC) and digital oscilloscopes [1-4], chronobiology [5-9] (A proper noun "cosinor" is used), astrophysics [10-15], image processing [16-18], and vestibulo-ocular reflex [19-21]. Since the accuracy of estimated sine wave parameters is crucial in measuring the effective number of bits [4, 22], sinusoidal model fitting has been causing a stir in the ADC community for quite some time. Algorithms have been standardized in IEEE Standards 1057 and 1241.

Assume that the recorded data consist of the samples sequence $y_0, y_1, \ldots y_{N-1}$, collected at time instants $t_i = i\Delta t$ for $i = 0 \sim N-1$, where Δt is the sampling interval. The FPSW model is

$$x(t) = A_0 \cos(\omega_0 t + \varphi_0) + B_0 + n_t \tag{1}$$

where A_0, B_0, φ_0 and ω_0 are the four parameters, the amplitude, offset, initial phase and frequency, respectively; n_t is noise.

Eq. (1) has four parameters. If the frequency is known, the three-parameter fitting algorithm can be implemented readily, for the solution is explicit. A straightforward way to specify the frequency is the nominal input frequency. However, the nominal input frequency may not be always available. Moreover, in some cases, the three-parameter fitting may not be reliable although the frequency has a minor error. For example, Baccigalupi has shown that the uncertainty of only 0.01% around its nominal value can lead to significant error [23].

The most attractive algorithm derives from the principle of least square error (LSE), which is four-parameter sine wave (FPSW) fitting. It seeks parameters A, B, φ and ω to minimize the following error square sum:

$$\begin{aligned} E(A,B,\omega,\varphi) &= \sum_{i=0}^{N-1} [y_i - x(i\Delta t)]^2 \\ &= \sum_{i=0}^{N-1} [y_i - A\cos(\omega t_i + \varphi) - B]^2 \end{aligned} \tag{2}$$

It is equivalent to the *maximum-likelihood estimator* in the case of the *Gaussian noise*.

This estimator is intrinsically nonlinear, and is solved by the numerical iteration in most literature. To improve the numerical performance, some techniques to improve the iteration robustness were suggested, for example, *singular value decomposition* (SVD) [24], *hybrid Newton Gauss-Newton algorithm* [25], normalization [26, 27], *Gram-Schmidt orthogonalization* (GSO) [28], and others. The method based on the GSO is very efficient, and its computation burden in each round is down by an order of $O(3N)$, significantly lower compared to the SVD technique.

One paramount issue in iteration is the initial value, which is the central topic of this paper. An efficient approach to obtain the initial value for the FPSW fitting will be proposed and tested systematically. It will be demonstrated that the bias error of the proposed approach is no greater than 0.0006 times of the FFT resolution for noise free cases. The noisy cases show that the *Cramer-Rao bound* (CRB) can be reached after only one round of iteration with the initial frequency obtained by the new approach.

The rest of the paper is organized as follows: In Section 2, the complication with inappropriate initial values will be investigated. In Section 3, a new concise approach will be derived from the discrete spectrum property of a truncated sine wave. In Section 4, the new approach will be tested by simulated signals contaminated with different levels of noise. Finally, conclusions are summarized in Section 5.

*Corresponding author: *E-mail:* chenkuifu@gmail.com

 ISSN: 1743-9310

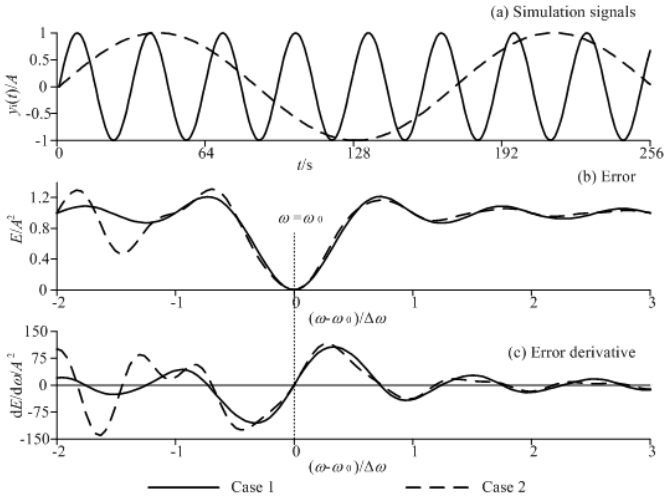

Figure 1. Illustrating the importance of the initial frequency in FPSW fitting

In (a), the simulation signal of the case 1 (solid line) covers 8.1487 cycles, and the case 2 (dashed line), 1.5 cycles. Other parameters of both cases are the same, $\varphi_0 = 0°$, $B_0 = 0$, $A_0 = 1$. The sampling size is $N = 256$, and sampling interval, $\Delta t = 1$ s. The vertical dot-line cross (b) and (c) shows that the global minimum of the error curve aligns with one zero of the derivative. However, the error derivatives in (c) have many other zeros. Starting from inappropriate initial frequency, the seeking zeros iteration can definitely converge to zeros other than ω_0.

2. INITIAL VALUES

This section will discuss the importance of good initial values for minimizing the error square sum in Eq. (2).

Minimizing $E(A, B, \varphi, \omega)$ in Eq. (2) is intrinsically nonlinear, which necessitates an iterative approach. With an iterative algorithm, convergence, computational efficiency and accuracy must be considered. They can be influenced by some or all of the following factors: initial values, method of calculation, stopping criteria [3], sampling density, and number of samples [29]. Further relevant factors include harmonic distortion, random noise, quantization error, and others [29]. For the case of a few cycles in record (CiR), some researchers have reported that the initial phase plays a role as well [30].

Of the aforementioned factors, the initial values are utmost important. Starting from an arbitrary initial value, the iteration may not converge. Or even though converged, but the results from different initial values may not converge to the unique global minimum due to possible trapping at a local minimum [29].

2.1 An Illustration

It must be pointed out that the frequency ω is prior among the four initial parameters, because the other three parameters can be determined readily by the three-parameter fitting if ω is known. To illustrate the importance of the initial frequency ω pictorially, Fig. 1 outlines two simplified cases of the error E of Eq. (2) varying with frequency.

The simulation signals in Fig. 1a are the perfect sinusoidal waves free of noise, which are generated by the model Eq. (1). Two line styles stand for two cases of ω_0, case 1: $\omega_0 = 0.2$ rad/s, and case 2: $\omega_0 = 0.0358$ rad/s, respectively. Other parameters are listed in the illustration of Fig. 1.

Saying strictly, E is a function of four variables, A, B, ω and φ. Therefore, E is a hyper-surface in a five-dimension space while varying all four variables. For highlighting the significance of the initial frequency, we assume that A, B and φ are the same as those used in generating y_i. We examine that the error E of this simplified case varies as the frequency ω, which is shown in Fig. 1b.

Both error curves are zero (the minimum) at $\omega = \omega_0$. To find the minimum E efficiently, most algorithms exclusively use the necessary condition when the error derivative is zero. The error derivative is shown in Fig. 1c. We can see that it is indeed zero when $\omega = \omega_0$. However, we can also find that the error derivatives have many other zeros, which are aligned with either the local minimums, or the local maximums of the error curves in Fig. 1b. Obviously, if the frequency is far from ω_0, an iterative approach of seeking the derivative's zeros will converge to the nearby local minimum or maximum of the error curves in Fig. 1b.

2.2 Some Remarks

To find the global minimum, some issues must be dealt with practically. The first is the practical criterion of the global minimum. An immediate idea is finding local minimums as many as possible, and picking up one from them. However, this cannot ensure that the smallest one is the actual global minimum definitely. Interestingly, the global minimum is zero in Fig. 1b, but it has to be pointed out that, in practice, the global minimum is not zero, due to the noise and model bias.

The second point is how the iteration being released from the local minimum trapping, which influences the computational efficiency significantly. Most algorithms are local convergent,

for example, the Newton method. A local convergent method will converge to the solution nearby the initial value. This property is reasonable generally, because most approaches to a nonlinear problem are based on approximating the nonlinearity with a linearity, which can work only with a relative small increment. Moreover, we are more familiar with the profile of the objective function close to the initial values than that far away from the initial values; therefore, we are more confident in the meaning of the solution nearby the initial values. In addition, if multiple solutions are interested, the local convergent method enables us to find them one by one.

However, for FPSW fitting, we are only interested in the global minimum. Spending too much time around the local minimum or local maximum is definitely inefficient. In practice, this may be compromised by comparing the error trend in the current converging route with the recorded minimum. If the former is significantly greater than the recorded, the current searching is interrupted.

The third point is how the iteration can be engaged in converging to the global minimum. One way is exhaustingly searching with the initial frequency scanned by a very small step. Obviously, this is not efficient. Another is randomly setting the initial frequency in the allowable bracket (so-called the evolutionary algorithm). However, both methods cannot guarantee success, particularly for the case when the local minimum is not well separated.

The fourth point is how to deal with the case with a few CiRs. The sampled signal with many CiRs has a little bit better behavior, compared to that with a few one. In Fig. 1, the error curve of case 1 (solid line, CiRs = 8.1487) and its derivative are approximately symmetrical about $\omega = \omega_0$, and the local minimums appear regularly with an interval about $\Delta\omega$ on both sides of $\omega = \omega_0$. The local maximums also intersperse those minimums uniformly. However, case 2 (dash line, CiRs = 1.5) is different, which can be due to the interference from the "negative" frequency, since this case covers only 1.5 cycles. Therefore, the behavior of the error and error derivative is more sophisticated; consequently, convergence to the global minimum necessitates a more meticulous requirement on the initial frequency.

It should be noted that Fig. 1b and Fig. 1c are only the simplified cases. During practical FPSW fitting, all four parameters change simultaneously. Thus, the properties of the error function are more difficult. As a result, converging to local minimums can occur more frequently.

2.3 Initial Values from Non-iterative Method

In IEEE standards, it was suggested that the initial frequency can be estimated by using a discrete Fourier transform (either on the full record or a portion of it), or by counting zero crossings, or simply by using the nominal (applied input) frequency [3]. More generally, the initial frequency can be obtained from any approach developed in the signal processing community. The requirement is non-iterative and of easy operation.

Interestingly, although the most attractive FPSW fitting is nonlinear, some concise non-iterative approaches have already been proposed in light of some approximations. These methods can certainly be utilized to obtain the initial frequency, too. For example, Zhang [31] has presented a non-iterative method, which is based on the property that four consecutive samples from a noise free FPSW model follow a linear equation. Baccigalupi has also presented a non-iterative approach according to the linear phase relationship for a noise free model [23].

Spectrum analysis is predominant in estimating frequencies, which are approximated with the frequencies corresponding to the eminent spectrum peaks. Indeed, as aforementioned, this method was suggested in IEEE Standards 1057 and 1241 to obtain the initial frequency of the FPSW fitting.

Most spectrum analysis utilizes the FFT. However, due to the frequency domain sampling of the canonical FFT, the frequency read from the FFT discrete spectrum line has the constant resolution limit $\Delta\omega = 2\pi/T$, and is subjected to the leakage [32-37]. The frequency sampling dense can be increased by the padding-zero technique [38] or the chirp Z-transform [39, 40]. The interpolated FFT is another approach to increase the frequency accuracy [41, 42]. Mishra [43] has verified this method for evaluating ADC. Most results listed in [43] are of frequency accuracy up to 0.01%.

The interpolated FFT method was tested generally on the simulation signal free of noise and with the CiRs greater than twenty in [43]. In ADC application, the case of a few CiRs appears frequently. Whether the interpolated FFT can work with this case is still an open question, but it can be predicted that its accuracy will deteriorate, since the interpolation is based on the cisoid model. For the case of a few CiRs, the negative frequency will interfere with the peak of the positive frequency materially. In addition, the interpolated FFT was mostly tested on the noise free simulation data in [43]. Actual data in the ADC application is subjected to noise definitely. Finally, although the frequency error is as low as 0.01% in [43], Baccigalupi has concluded that such error scale can still lead to significant error [23].

3. NEW PROPOSAL

In this section, the spectral property of a truncated sine wave will be investigated; then a new proposal to initializing the FPSW fitting will be derived.

3.1 Discrete Spectrum of Truncated Sine Wave

We have proposed an explicit approach based on the Hanning window [44]; however, windowing is seldom used in FSPW fitting. Therefore, an approach without windowing will be presented here.

To derive this approach, the noise term in Eq. (1) is temporally ignored. Accordingly, the remaining part can be expressed as the summation of the offset (its frequency is zero) and two cisoid waves with circular frequencies $\pm\omega_0$. From the view of the Fourier series analysis, the three Fourier coefficients corresponding to frequency 0 and $\pm\omega_0$ are finite. From the viewpoint of the Fourier transform, the frequency spectrum possesses three infinite peaks at 0 and $\pm\omega_0$.

As for practical signal collecting and processing, the infinite time presumption implied in the above argument is not applicable. All algorithms and measurements can only be applied to the data over a finite durative period. Assuming that the model Eq. (1) is truncated over [0, T], and the signal beyond [0, T] is zero, then its Fourier transform $X(\omega)$ becomes a continuous finite function as

$$\begin{aligned} X(\omega) &= \int_0^T x(t)\exp(-j\omega t)dt \\ &= \int_0^T [A_0\cos(\omega_0 t+\varphi_0)+B_0]\exp(-j\omega t)dt \end{aligned} \tag{3}$$

In light of the properties of the Fourier transform and the sine wave, $X(\omega)$ can be written explicitly as

$$\begin{aligned} X(\omega) = &\frac{\exp(j\varphi_0)D(\omega-\omega_0)}{\omega-\omega_0}+\frac{\exp(-j\varphi_0)D(\omega+\omega_0)}{\omega+\omega_0} \\ &+2\frac{B_0}{A_0}\frac{D(\omega)}{\omega} \end{aligned} \tag{4}$$

Here,

$$D(\omega) = A_0\exp\left(-\frac{j\omega T}{2}\right)\sin\frac{\omega T}{2} \tag{5}$$

Generally, the spectrum analysis is speeded up by the fast Fourier Transform (FFT). With regard to FFT, the frequency sampling interval $\Delta\omega$ is $2\pi/T$. Now, let us check three FFT spectrum lines at $\omega_1 = k_1\Delta\omega$, $\omega_2 = k_2\Delta\omega$, $\omega_3 = k_3\Delta\omega$, where all the $k_1 < k_2 < k_3$ are integers. It is easy to verify that

$$D(\omega_1-\omega_0) = D(\omega_2-\omega_0) = D(\omega_3-\omega_0) \tag{6}$$

and the third term of Eq. (4) is zero at ω_1, ω_2, ω_3 (temporally we assume $\omega_k \neq 0$). We denote that

$$\begin{cases} D^+ = \exp(j\varphi_0)D(\omega_k-\omega_0) \\ D^- = \exp(-j\varphi_0)D(\omega_k+\omega_0) \end{cases} \quad \text{for } k = 1\sim 3 \tag{7}$$

3.2 New Approach

According to Eq. (4) and (7), for any three consecutive spectrum lines at ω_1, ω_2, ω_3 ($\omega_k \neq 0$), they observe the following three simultaneous equations

$$\begin{cases} \dfrac{D^+}{\omega_1-\omega_0}+\dfrac{D^-}{\omega_1+\omega_0}-X(\omega_1)=0 \\ \dfrac{D^+}{\omega_2-\omega_0}+\dfrac{D^-}{\omega_2+\omega_0}-X(\omega_2)=0 \\ \dfrac{D^+}{\omega_3-\omega_0}+\dfrac{D^-}{\omega_3+\omega_0}-X(\omega_3)=0 \end{cases} \tag{8}$$

If D^+ and D^- are treated as the unknown variables, they occur linearly in Eq. (8). Thus if Eq. (8) is treated as homogeneous linear simultaneous equations, then the solution vector is $\{D^+, D^-, -1\}^T$. The existence of nonzero solution requires that the determinant of coefficient matrix be zero, that is

$$\begin{vmatrix} \dfrac{1}{\omega_1-\omega_0} & \dfrac{1}{\omega_1+\omega_0} & X(\omega_1) \\ \dfrac{1}{\omega_2-\omega_0} & \dfrac{1}{\omega_2+\omega_0} & X(\omega_2) \\ \dfrac{1}{\omega_3-\omega_0} & \dfrac{1}{\omega_3+\omega_0} & X(\omega_3) \end{vmatrix} = 0 \tag{9}$$

We can solve out the explicit expression of ω_0 as follows,

$$\omega_0 = \sqrt{\Pi_2/\Pi_0} \tag{10}$$

where

$$\Pi_0 = \begin{vmatrix} 1 & \omega_1 & X(\omega_1) \\ 1 & \omega_2 & X(\omega_2) \\ 1 & \omega_3 & X(\omega_3) \end{vmatrix}, \quad \Pi_2 = \begin{vmatrix} 1 & \omega_1 & \omega_1^2X(\omega_1) \\ 1 & \omega_2 & \omega_2^2X(\omega_2) \\ 1 & \omega_3 & \omega_3^2X(\omega_3) \end{vmatrix} \tag{11}$$

After ignoring numerical integration error, Eq. (10) holds for any nonzero ω_1, ω_2, ω_3.

In practice, ω_1, ω_2, ω_3 should be chosen to encompass the spectrum peak. More specifically, ω_2 is chosen to align with the highest one, ω_1 and ω_3 are one bin to ω_2, on the left and right, respectively. There are two reasons for doing so. First, the integration is more accurate around spectrum peaks. Secondly, the SNR of spectrum peaks is higher.

We must consider the special case of a very low frequency. For this case, $\omega_1 = 0$, we have

$$\frac{D^+}{\omega_1-\omega_0}+\frac{D^-}{\omega_1+\omega_0}-B_0=0 \tag{12}$$

Now the above theory of linear simultaneous equations is not applicable. To facilitate us to use this theory still, we substitute ω_1 with $-\omega_2$, as a result, $X(\omega_1) = X(-\omega_2) = X^*(\Delta\omega)$. Accordingly, Eq. (9) still holds true.

4. NUMERICAL EXAMPLES

In this section, Eq. (10) will be tested by firstly the noise free signal and then by the noise signals with six levels of SNR.

4.1 Simulation Environment and Parameters

The noise free signals are generated according to Eq. (1). Since the offset B_0 does not influence the numerical condition significantly [27], its value is simply set $B_0 = 0$. However, the offset of practically collected series will be removed before FFT. Therefore, $B_0 = 0$ occurs only in the case of coherent sampling, where an integer number of its cycles fit into a predefined sampling window. The signal amplitude affects the condition number of the normal matrix dramatically. Here, its value is set $A_0 = 1$, which is close to the optimal [26]. The sampling interval Δt and the sampling size N are 1s and 1024, respectively. Thus the sampling window is $T = N\Delta t = 1024$s.

Since we are interested more in the case of a few cycles in record, the simulation frequency ω_0 scans from $2\pi/T$ to $16\pi/T$, with a step $0.04\pi/T$. This means the CiR changes

from 1 to 8, with an increment 0.02. Thus we have ((8-1)/0.02)+1), i.e., 351different frequencies.

For the noise free case, we simulate 180 initial phases at each frequency. These initial phases φ_0 scan linearly from 0° to 179° with a step 1°. Thus there are 351×180 trials totally in the noise free case.

For the noise contaminated examples, only four initial phases, φ_0 = 0°, 45°, 90° and 135° are examined. For each combination of the frequency by phase, six noise levels, SNR= -3.01dB, 3.33dB, 5.00 dB, 10.00 dB, 26.99dB, 56.99dB, are tested. Each noise level simulates 1000 trials. Thus there are 351×4×6×1000 trials totally in the noise contaminated case. The random noise is generated by the *randn* function of MATLAB™.

After each simulation signal is generated, its offset is removed, and then the FFT is carried on. Three discrete spectrum lines are selected according to Section 3. The initial frequency is obtained by Eq. (10).

For the noise-contaminated case, two rounds of conventional FPSW fitting are carried.

4.2 Noise Free Case

The absolute frequency errors for four typical initial phases are presented in Fig. 2, where four panels stand for φ = 0°, 45°, 90° and 135° respectively. The abscissa is CiR, standing for the wave cycles in the recording window. Inspecting this figure leads to the following remarks:

1. The frequency from Eq. (10) is very precise. Insofar as the simulated examples, the maximum error is no greater than $0.0006\Delta\omega$, where $\Delta\omega$ is the resolution of canonical FFT. The maximum error appears in Fig. 2d, where the initial phase φ = 135°.
2. The sizes of four error curves are comparable. The global trends attenuate, but there are significant fluctuations. To the left, where the CiR is fewer, the error is larger. While the CiR increases from the left to the right, the error trend decreases.
3. The coherent sampling condition aligns with an integer CiR, where the error is very small, and approaches the horizontal axis. One reason is that, ω_0 exactly aligns with ω_2, which is the highest spectrum line. Under this condition, $X(\omega_1) = X(\omega_3) = 0$ exactly holds true, also Eq. (10) degenerates to $\omega_0 = \omega_2$.
4. The coherent sampling does not often happen in practical measurement. The worst case in FFT analysis is the sampling window covering an integer and a half periods of a signal. Four plots in Fig. 2 show that the frequency error with half-period sampling depends on the initial phase as well. The two curves on the left column have relatively smaller error around the half-integer CiRs, but the two on the right align with local peaks. However, readings from the FFT discrete spectrum lines are always accurate with coherent sampling, and inaccurate with half-period sampling.
5. The influence of the sampling dense on the accuracy is secondary. The effect of sampling dense is controversial. At least, the sampling dense should observe the Shannon sampling theory, that is, each period should cover at least two points. Since the sampling size *N* is constant when the CiR scans from the left to the right, there are much less sampling points in one period at the right end than at the left, but the decreasing magnitude of the frequency error is significant smaller than the fluctuation due to the coherent sampling and half-period sampling.

All the errors from 180 initial phases are pooled together in Fig. 3. The ordinate is the maximum error among 180 phases at each frequency. This is equivalent to the error envelope. This envelope verifies again that: 1) the maximum error is no greater than $0.0006\Delta\omega$; 2) The coherent sampling is the most accurate condition; 3) the accuracy attenuates non-monotonically as the CiR increases; 4) The influence of the sampling dense on the accuracy is secondary.

4.3 Noise Contaminated Case

In this case, we do not have exact solutions. What we can evaluate is the statistical performance. Generally, the two issues: bias and variance need considering. However for FPSW fitting, an unbiased estimation is generally assumed beforehand [45]. As a result, the variance is bound by the *Cramer–Rao bound* (CRB). For practical evaluation, we use the empirical variance or the *empirical mean square error* (eMSE) defined in [46].

Results from two levels of SNR = 3.33dB and 26.99dB are shown in Fig. 4. The thick dotted curves are the eMSE of the initial frequency from Eq. (10). Eight dotted curves are similar. All possess peaks around the half-integer of CiRs and troughs around the integer of CiRs. The peak infers a larger eMSE, and less accurate. The trough means more accurate. Again, this is consistent with the noise free case: coherent sampling means accurate. The fluctuation amplitude is around several dBs (standard deviation is 1.6dB), almost independent of the initial phase and noise level.

The thick line transgressing hollow circles is the theoretical CRB. We can see that the eMSE of Eq. (10) is greater than the CRB, which is the lowest bound of all possible estimators. The average difference is less than 4 dB between the CRB and the eMSE, which is listed in Table 1, where m_0 is the mean eMSE. The average operation here is carried over 351 different initial frequencies. Δ_0 is the mean difference between the CRB and the eMSE of the initial frequency. It is calculated by the difference at each frequency, so Δ_0 is not strictly equal to the CRB subtracting m_0 in Table 1.

With the initial frequency obtained by Eq. (10), two rounds of the normal FPSW fitting are carried out. The frequencies of the first round and the second round are denoted as ϖ_1 and ϖ_2, respectively.

The hollow circle in Fig. 4 stands for the eMSE of ϖ_1. We can see that this eMSE matches the CRB well; moreover, the small ripples of the CRB are followed by the eMSE. This match is almost independent of phases and noises levels. The cases of the other three noise levels lower than SNR = 3.33dB have similar performance, and are not shown for the sake of brevity.

In Table 1, m_1 and m_2, Δ_1 and Δ_2 have the similar definition as m_0 and Δ_0. The only difference is that the frequency in m_1 and Δ_1 is substituting the initial frequency with ϖ_1, and in m_2 and Δ_2 with ϖ_2. In the same vein as the initial frequency, $\Delta_1 \neq m_1$ – CRB and $\Delta_2 \neq m_2$ – CRB hold.

The above perfect match is also uncovered by Δ_1 in Table 1, which is close to zero, meaning that the difference is minor between the CRB and eMSE of the frequencies after one round of iteration. Moreover, m_2 is very close to m_1, and Δ_2 is of the comparable size of Δ_1.

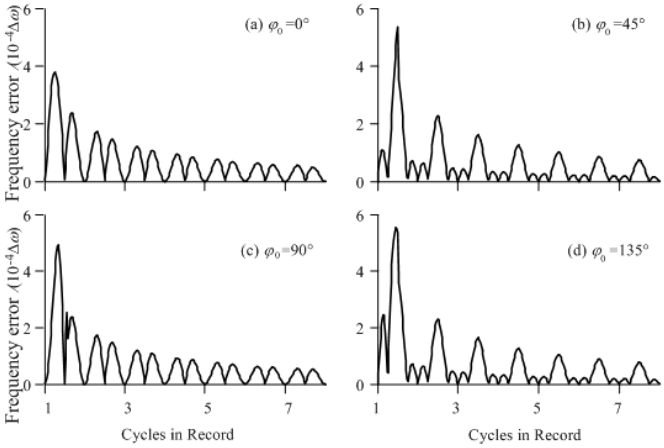

Figure 2. The absolute error of frequency calculated by Eq. (10)

(The simulation signals are generated by Eq. (1), and free of noise)

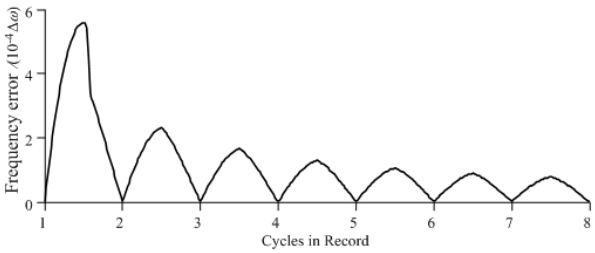

Figure 3. The envelope of frequency error

(All the frequency errors from 180 initial phases are pooled together, and the ordinate is the maximum at each frequency)

Table1. Statistical Performance of the proposed approach

No.	SNR/dB	φ_0/(°)	CRB/dB	Initial Value		First Round		Second Round	
				m_0/dB	Δ_0/dB	m_1/dB	Δ_1/dB	m_2/dB	Δ_2/dB
1	-3.01	0	-74.11	-70.47	3.65	-73.93	0.18	-73.99	0.13
		45	-74.59	-70.73	3.86	-74.37	0.22	-74.44	0.15
		90	-74.42	-70.92	3.49	-74.24	0.18	-74.29	0.13
		135	-73.94	-70.69	3.26	-73.81	0.13	-73.86	0.09
2	3.33	0	-80.46	-76.94	3.52	-80.42	0.04	-80.43	0.03
		45	-80.93	-77.22	3.71	-80.90	0.04	-80.91	0.02
		90	-80.76	-77.36	3.40	-80.72	0.04	-80.73	0.03
		135	-80.29	-77.13	3.15	-80.27	0.01	-80.28	0.00
3	5.00	0	-82.12	-78.62	3.50	-82.09	0.03	-82.10	0.02
		45	-82.60	-78.92	3.68	-82.59	0.01	-82.60	0.01
		90	-82.43	-79.05	3.38	-82.40	0.03	-82.41	0.02
		135	-81.95	-78.80	3.15	-81.93	0.03	-81.93	0.02
4	10.00	0	-87.12	-83.66	3.47	-87.13	0.00	-87.13	-0.01
		45	-87.60	-83.94	3.66	-87.59	0.01	-87.59	0.01
		90	-87.43	-84.08	3.35	-87.41	0.02	-87.42	0.01
		135	-86.95	-83.83	3.13	-86.97	-0.02	-86.97	-0.02
5	26.99	0	-104.11	-100.66	3.45	-104.11	0.01	-104.11	0.01
		45	-104.59	-100.95	3.64	-104.60	-0.01	-104.60	-0.01
		90	-104.42	-101.06	3.36	-104.41	0.00	-104.41	0.00
		135	-103.94	-100.84	3.10	-103.94	0.00	-103.94	0.00
6	56.99	0	-134.11	-130.67	3.44	-134.11	0.00	-134.11	0.00
		45	-134.59	-130.93	3.67	-134.59	0.00	-134.59	0.00
		90	-134.42	-131.05	3.37	-134.41	0.01	-134.41	0.01
		135	-133.94	-130.85	3.09	-133.96	-0.02	-133.96	-0.02

CRB and SNR stand for the Cramer–Rao bound and signal-to-noise ratio, respectively. $m_0 \sim m_2$ are the mean eMSE of the initial frequency, ϖ_1 and ϖ_2, iterating frequencies from the first and second round of the normal FPSW fitting The average operation here is carried over 351 different initial frequencies. $\Delta_0 \sim \Delta_2$ are the mean difference between the CRB and the eMSE of the frequency, ϖ_1 and ϖ_2.

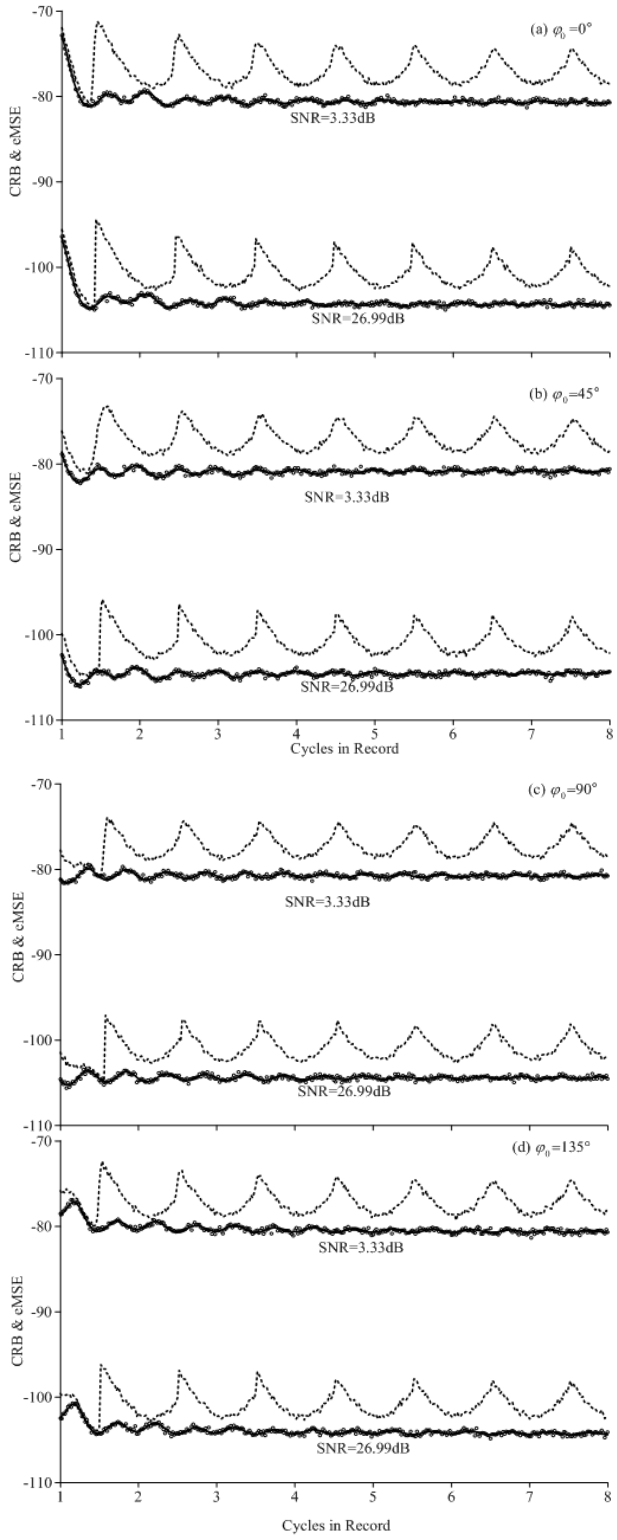

Figure 4. The statistical performance of Eq. (10)

(The thick dot curves are the eMSE of the initial frequencies from Eq(10). The thick lines transgressing hollow circles are the theoretical CRBs. The hollow circles stand for the eMSE of the frequencies from the first round of FPSW fitting with the initial frequency by Eq(10).)

These facts illustrate that the improvement benefit from the second round of iteration is very limited.

It should be stressed that the level of SNR = 3.33dB is very noisy. One example of the simulated signals is shown in Fig. 5, so we can have visual impact about the noise condition of the low SNR.

If the noise level increases further, some outliers can happen indeed. The results from the case of SNR = -3.01dB is shown in Fig. 6. We can see an obvious spine on the eMSE of the initial frequency in Fig. 6a, labeled by "X". Carefully checking data finds that this spine is due to the significant error of only one trial. For this trial, the noise forms a pseudo peak on the amplitude spectrum far away from the actual. Therefore, error has occurred when picking up ω_2.

This kind of error does occur in other three panels. The occurring times are 14 in Fig. 6a ($\varphi = 0°$), 4 in Fig. 6b ($\varphi = 45°$), 2 in Fig. 6c ($\varphi = 90°$), and 2 in Fig. 6d ($\varphi = 135°$). The incidence is only $(14+4+2+2)/(351\times4\times1000) = 1.56\times10^{-5}$, which is very low. Because of the smear effecting of averaging many trials, not all the mistakes of picking up ω_2 lead to significant spines. The data of the hollow circles in Fig. 6 have excluded the above outliers due to mistakes of picking up ω_2. The match between the eMSE and the CRB is not as good as in Fig. 4. It must be stressed that the mistake of picking up ω_2 never occurs in the trials of other five levels of SNR.

Insofar as we simulate, the initial frequency and two rounds of iteration is not sensitive to the initial phase. However, this mistake of picking up ω_2 somewhat depends on the initial phase. Whether this phenomenon has the same essence as phase dependence reported in the other literature still needs further studying.

5. CONCLUSIONS

Four-parameter sine wave fitting based on the least square error principle is nonlinear. An iterative approach to this problem necessitates the initial frequency. The importance of the initial frequency to the FPSW fitting is discussed in detail. An efficient approach to obtain the initial value for FPSW fitting is proposed, which makes use of three spectrum lines of the FFT. This approach has been validated by simulation data contaminated with different levels of noise.

The results from the noise free case show that: 1) The frequency error of the proposed approach is no greater than $0.0006\Delta\omega$, where $\Delta\omega$ is the FFT resolution; 2) While the CiR increases, the global trend of the frequency error attenuates, but there are significant fluctuations; 3) The coherent sampling condition has the best accuracy still. The accuracy with half-period sampling is dependent on the initial phase; 4) The influence of the sampling dense on the error is secondary.

Insofar as the simulation trials of the noise contaminated case, the results show, firstly, the eMSE of the proposed approach is more accurate with coherent sampling. The worst accuracy occurs with half-period sampling. Secondly, the average difference is the around 3.5 dB between the CRB and the eMSE of the proposed approach. Thirdly, the CRB can be reached after only one round of iteration starting from the initial frequency obtained by the proposed approach, and further rounds of iteration lead to little improvement.

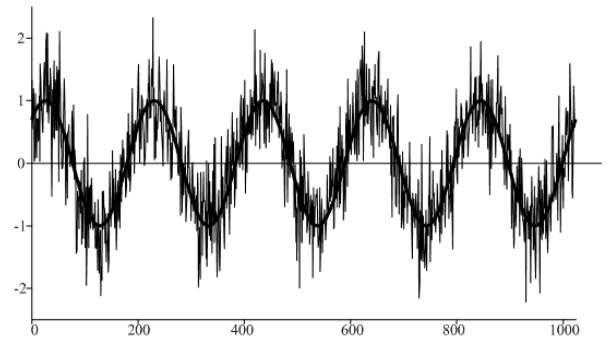

Figure 5. One example of simulation signals with SNR=3.33dB

(The thick line is the noise free data, and the fine zigzag stands for the noise contaminated data)

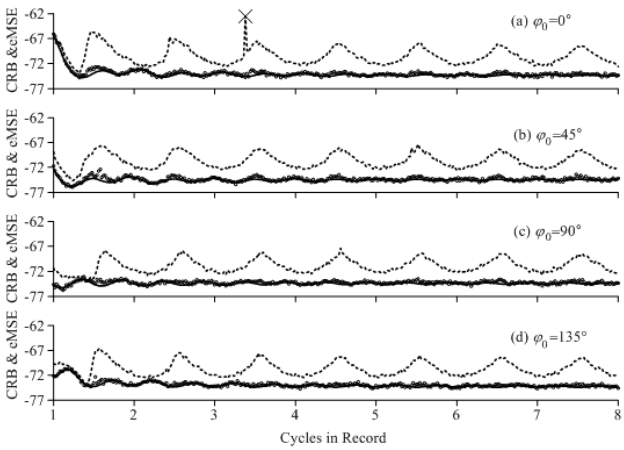

Figure 6. One simulated data series at SNR=-3.01dB

(An obvious spine on the eMSE of the initial frequency in (a), labeled by "X", is due to the significant error of only one trial. Other legends see Fig. 4)

REFERENCES

[1] C. Wegener, M. P. Kennedy, "Testing ADCs for static and dynamic INL-killing two birds with one stone", Computer Standards & Interfaces, Vol. 26, 2004, pp. 15-20.

[2] P. Arpaia, H. Schumny, "International standardization of ADC-based measuring systems-state of the art", Computer Standards & Interfaces, Vol. 19, 1998, pp. 173-188.

[3] T. Z. Bilau, T. Megyeri, A. Sarhegyi, J. Markus, I. Kollar, "Four-parameter fitting of sine wave testing result: iteration and convergence", Computer Standards & Interfaces, Vol. 26, 2004, pp. 51-56.

[4] J. J. Blaira, T. E. Linnenbrinkb, "Corrected RMS error and effective number of bits for sine wave ADC tests", Computer Standards & Interfaces, Vol. 26, 2003, pp. 43-49.

[5] E. Filipski, F. Delaunay, V. M. King, "Effects of chronic jet lag on tumor progression in mice", Canser Research, Vol. 64, 2004, pp. 7879-7885.

[6] R. A. Debon, E. Boselli, R. Guyot, B. Allaouchiche, "Chronopharmacology of intrathecal sufentanil for labor analgesia - Daily variations in duration of action", Anesthsiology, Vol. 101, 2004, pp. 978-982.

[7] T. Reilly, E. Bambacichi, "Methodological issues in studies of rhythms in human performance", Biological Rhythm Research, Vol. 34, 2003, pp. 321-336.

[8] I. C. Pasqua, C. R. C. Moreno, "The nutritional status and eating habits of shift workers: A chronobiological approach", Chronobiology International, Vol. 21, 2004, pp. 949-960.

[9] P. S. Albert, S. Hunsberger, "On analyzing circadian rhythms data using nonlinear mixed models with harmonic terms", Biometrics, Vol. 61, 2005, pp. 1115-1120.

[10] B. S. Gaudi, K. Z. Stanek, J. D. Hartman, M. J. Holman, B. A. McLeod, "On the rotation period of (90377) Sedna", Astrophysical Journal, Vol. 629, 2005, pp. L49-L52.

[11] S. Vig, S. K. Ghosh, D. K. Ojha, "Warp signatures of the Galactic disk as seen in mid infrared from Midcourse Space Experiment", Astronomy & Astrophysics, Vol. 436, 2005, pp. 867-877.

[12] V. D. Bychkov, L. V. Bychkova, J. Madej, "Catalog of stellar magnetic rotational phase curves", Astronomy & Astrophysics, Vol. 430, 2005, pp. 1143-1154.

[13] L. Homer, S. F. Anderson, B. Margon, R. A. Downes, E. Deutsch, "Optical identification of the X-ray burster X1746-370 in the globular cluster NGC 6441", Astronomical Journal, Vol. 123, 2002, pp. 3255-3262.

[14] J. L. Ortiz, A. Sota, R. Moreno, E. Lellouch, N. Biver, A. Doressoundiram, P. Rousselot, P. Gutierrez, R. Marquez, R. Delgado, V. Casanova, "A study of Trans-Neptunian object 55636 (2002 TX300)", Astronomy & Astrophysics, Vol. 420, 2004, pp. 383-388.

[15] J. Callaway, M. Storvik, P. Halonen, H. Hakko, P. Rasanen, J. Tiihonen, "Seasonal variations in [H-3] citalopram platelet binding between healthy controls and violent offenders in Finland", Human Psychopharmacology-Clinical and Experimental, vol. 20, 2005, pp. 467-472.

[16] N. Pears, B. J. Liang, Z. Z. Chen, "Mobile robot visual navigation using multiple features", EURASIP Journal on Applied Signal Processing, Vol. VL 2005, 2005, pp. 2250-2259.

[17] D. F. Wilson, S. A. Vinogradov, P. Grosul, A. Kuroki, J. Bennett, "Imaging oxygen pressure in the retina of the mouse eye", Advances In Experimental Medicine and Biology-Oxygen Transport to Tissue XXVI, D. F.ol. 566, 2005, pp. 159-165.

[18] J. Villa, J. A. Quiroga, J. A. Gomez-Pedrero, "Measurement of retardation in digital photoelasticity by load stepping using a sinusoidal least-squares fitting", Optics and Lasers in Engineering, Vol. 41, 2004, pp. 127-137.

[19] S. B. Yakushin, Y. Q. Xiang, T. Raphan, B. Cohen, "Spatial distribution of gravity-dependent gain changes in the vestibuloocular reflex", Journal of Neurophysiology, Vol. 93, 2005, pp. 3693-3698.

[20] X. H. Si, D. E. Angelaki, J. D. Dickman, "Response properties of pigeon otolith afferents to linear acceleration", Experimental Brain Research, Vol. 117, 1997, pp. 242-250.

[21] C.Siebold, E. Anagnostou, S. Glasauer, L. Glonti, J. Kleine, T. Tchelidze, U. Buttner, "Canal-otolith interaction in the fastigial nucleus of the alert monkey", Experimental Brain Research, Vol. 136, 2001, pp. 169-178.

[22] D. Bellan, A. Brandolini, L. di Rienzo, A. Gandelli, "Improved definition of the effective number of bits in ADC testing", Computer Standards & Interfaces, Vol. 19, 1998, pp. 231-236.

[23] A. Baccigalupi, "ADC testing methods", Measurement, Vol. 26, 1999, pp. 199-205.

[24] R. Pintelon, J. Schoukens, "An improved sine-wave fitting procedure for characterizing data acquisition channels", IEEE Transactions on Instrumentation and Measurement, Vol. 45, 1996, pp. 588-593.

[25] D. Haddadi, D. Dallet, P. Marchegay, "Hybrid Newton Gauss-Newton algorithm for time-domain analysis of A/D converters", IEEE Transactions on Circuits and Systems II-Analogy and Digital Signal Processing, Vol. 47, 2000, pp. 655-659.

[26] K. F. Chen, "Improving four-parameter sine wave fitting by normalization", Computer Standards & Interfaces, Vol. 29, 2007, pp. 184-190.

[27] K. F. Chen, Y. M. Xue, "On the condition of four-parameter sine wave fitting", Computer Standards & Interfaces, Vol. 29, 2007, pp. 174-183.

[28] K. F. Chen, Y. M. Xue, "Four-parameter sine wave fitting by Gram-Schmidt orthogonalization", Measurement, Elsevier, Vol. 41, 2008, pp. 76-87.

[29] M. F. da Silva, P. Ramos, A. C. Serra, "A new four parameter sine fitting technique", Measurement, Vol. 35, 2004, pp. 131-137.

[30] M. F. da Silva, A. C. Serra, "New methods to improve convergence of sine fitting algorithms", Computer Standards & Interfaces, Vol. 25, 2003, pp. 23-31.

[31] J. Q. Zhang, X. M. Zhao, X. Hu, J. W. Sun, "Sinewave fit algorithm based on total least-squares method with application to ADC effective bits measurement", IEEE Transactions on Instrumentation and Measurement, Vol. 46, 1997, pp. 1026-1030.

[32] A. Breitenbach, "Against spectral leakage", Measurement, Elsevier, Vol. 25 1999, pp. 135-142.

[33] J. Schoukens, Y. Rolain, R. Pintelon, "Analysis of windowing/leakage effects in frequency response function measurements", Automatica, Vol. 42, 2006, pp. 27-38.

[34] A. Testa, D. Gallo, R. Langella, "On the Processing of Harmonics and Interharmonics: Using Hanning Window in Standard Framework", IEEE Transactions on Power Delivery, Vol. 19, 2004, pp. 28-34.

[35] E. Nunzi, P. Carbone, D. Petri, "A procedure for highly reproducible measurements of ADC spectral parameters", IEEE Transactions on Instrumentation and Measurement, Vol. 52, 2003, pp. 1279-1283.

[36] R. M. Hidalgo, J. G. Fernandez, R. R. Rivera, H. A. Larrondo, "A simple adjustable window algorithm to improve FFT measurements", IEEE Transactions on Instrumentation and Measurement, Vol. 51, 2002, pp. 31-36.

[37] D. Belega, M. Ciugudean, D. Stoiciu, "Choice of the cosine-class windows for ADC dynamic testing by spectral analysis", Measurement, Vol. 40, 2007, pp. 361-371.

[38] B. Rust, "The fast fourier transform for experimentalists part III: Classical spectral analysis", Computing in Science and Engineering, Vol. 7, 2005, pp. 74-78.

[39] M. Aiello, A. Cataliotti, S. Nuccio, "A chirp-z transform-based synchronizer for power system measurements", IEEE Transactions on Instrumentation and Measurement, Vol. 54, 2005, pp. 1025-1032.

[40] I. Sarkar, A. T. Fam, "The interlaced chirp Z transform", Signal Processing, Vol. 86, 2006, pp. 2221-2232.

[41] E. Aboutanios, B. Mulgrew, "Iterative frequency estimation by interpolation on Fourier coefficients", IEEE Transactions on Signal Processing, Vol. 53, 2005, pp. 1237-1242.

[42] D. Agrez, "Interpolation in the frequency domain to improve phase measurement ", Measurement, Elsevier, Vol. 41, 2008, pp. 151-159.

[43] D. K. Mishra, "ADC testing using interpolated fast Fourier transform (IFFT) technique", International Journal of Electronics, Vol. 90, 2003, pp. 459-469.

[44] K. F. Chen, X. Cao, Y. F. Li, "Sine Wave Fitting to Short Records Initialized with the Frequency Retrieved from Hanning Windowed FFT Spectrum", Measurement, Elsevier, Vol. 42, 2009, pp. 127-135.

[45] T. Andersson, P. Handel, "IEEE Standard 1057, Cramer–Rao Bound and the Parsimony Principle", IEEE Transactions on Instrumentation and Measurement, Vol. 55, 2006, pp. 44-53.

[46] P. Handel, "Properties of the IEEE-STD-1057 four-parameter sine wave fit algorithm", IEEE Transactions on Instrumentation and Measurement, Vol. 49, 2000, pp. 1189-1193.

Biographies

Kui Fu Chen was born in Jiangsu, China, 1969. He received the Ph.D. in biomedical engineering from Peking Union Medical College in 2000, and ME in computational mechanics from China Agricultural University in 1994, and BE in engineering mechanics from Beijing Agricultural Engineering University in 1991. He was a one-year research student in signal processing in Shimane University, Japan, in 2000. In 1994, he joined the China Agricultural University (CAU). He was a postdoctoral researcher in the Neurological Science Institute, Oregon Health and Science University, from Oct. 2002 to May. 2004, and research associate in Rehabilitation Institute of Chicago from May. 2004 to Aug. 2005. Now he is an associate professor in College of Sciences, CAU. His interests include signal processing, biomechanical modeling, motor control, computational mechanics, and vibration analysis. He is a board member of random vibration committee of Chinese Vibration Engineering Association. He has published over 60 peer-reviewed papers. He was awarded: Excellent Teacher in Mechanics (China Association of Mechanics, 2006); Achievement in Science and Technology (Chinese Educational Committee and Chinese Agriculture Ministry, 1995).

STABILIZING AND BALANCING OF INPUT DC VOLTAGES OF FIVE LEVELS DIODE CLAMPED INVERTER BY COMBINING SPACE VECTOR MODULATION AND SLIDING MODE CONTROL

N. Lourci [1,*], E. M. Berkouk [2], D. Lalili [1]

[1] Laboratoire d'Etude et de Modelisation en Electrotechnique (LAMEL), Departement d'Electrotechnique, Universite de Jijel, Algerie

[2] Laboratoire de Commande des Processus (LCP), Departement d'Electrotechnique, Ecole Nationale Polytechnique, Alger, Algerie

ABSTRACT

The stability problem of the input DC voltages in a five levels diode clamped inverter is recalled and illustrated. A knowledge model of this converter using switching functions and a space vector PWM strategy is demonstrated in detail. To investigate the instability problem of the input DC voltages of the inverter, we study a cascade constituted by a two levels rectifier - five levels diode clamped inverter - induction motor. To solve this problem, we stabilize the rectifier output voltage using the sliding mode control and we balance the input DC voltages of the five levels diode clamped inverter by using redundant vectors of the space vector PWM strategy. The obtained results show the effectiveness of our method which can be used to stabilize the input DC voltages of the multilevel converters.

Keywords

Five Levels Inverter, Two Levels Rectifier, Induction Motor, Space Vector PWM, Current Hysteresis Strategy, Sliding Mode Control.

1. INTRODUCTION

Multilevel power conversion technology is a rapidly growing area of power electronics with strong potential for further development [1]. The most attractive applications of this technology are in the medium to high voltage range, and include motor drives, power distribution, power quality and power conditioning applications [2].

In general, multilevel power converters can be viewed as voltage synthesizers, in which the high output voltage is synthesized from many discrete smaller voltage levels [3].

The selection of the best multilevel topology and the best control strategy for each given application is often not clear and is subject to various engineering trade-offs [4, 5]. By narrowing this study to the DC/AC multilevel power conversion technologies that do not require power regeneration, several attractive topological, modulation and power semiconductor device choices present themselves [6-8].

*Corresponding author: *E-mail:* nabillourci@gmail.com

 ISSN: 1743-9310

The main drawback of multilevel inverter is the problem of voltage imbalance in DC capacitors. The currents in midpoints of DC link input produce ripple in the capacitor voltages. This ripple may cause low-order harmonic contents in the output voltages. Moreover, the imbalance of capacitor voltages will cause excessive voltage pressure on switching devices of the inverter. This problem becomes more complex with increase of level of the inverter, because of increasing of midpoints in the DC link input [9].

Several methods are proposed to suppress the unbalance of DC link capacitor voltages [10-15]. In this way, we propose in this paper to generate the input DC voltage of the five levels diode clamped inverter by a two levels rectifier. The rectifier output voltage obtained increase continually. In order to stabilize it, we propose to use the sliding mode control. The rectifier output voltage became stable, but the inverter input voltages remain instable. To resolve this problem, we propose an algorithm for balancing of DC link capacitor voltages, which explain how to choose desirable redundant vector on the base of measurement of load currents and DC link capacitors voltages and currents signs. The results obtained with this solution shows that the proposed solution is very efficient to solve the instability problem of the multilevel inverter.

In this paper, firstly we modelize the five levels diode clamped inverter. Then, we present a brief review of space vector modulation for this inverter. After that, we develop an algorithm for balancing of DC-link capacitor voltages. In this part, the inverter is fed by a constant input DC voltage. In the last part, we study a cascade constituted by a two levels rectifier - five levels diode clamped inverter - induction motor. We use the sliding mode control for the rectifier output voltage stabilization, and the space vector modulation redundant vectors for the input DC voltages balancing of the five levels diode clamped inverter. The proposed study is verified through simulation.

2. FIVE LEVELS DIODE CLAMPED INVERTER

Structure of five levels diode clamped inverter is shown in Fig. 1. Each arm is composed of four upper and lower switches with anti-parallel diodes. Four series DC-link capacitors split the DC-bus voltage in half. The necessary conditions for the switching states for the five levels inverter are that the DC-link capacitors should not be shorted, and the output current should be continuous [3, 5].

The connection function F_{ij} indicates the state of the switch TD_{ij}:

$$F_{ij} = \begin{cases} 1 & \text{if } TD_{ij} \text{ is closed} \\ 0 & \text{if } TD_{ij} \text{ is opened} \end{cases} \quad (i = 1\ldots3\ ,\ j = 1\ldots8) \quad (1)$$

We define as well the half arm connection functions by the following relations:

$$\begin{cases} F_{i1}^{b} = F_{i1}.F_{i2}.F_{i3}.F_{i4} \\ F_{i0}^{b} = F_{i5}.F_{i6}.F_{i7}.F_{i8} \\ F_{i1}^{bb} = (1-F_{i1}).F_{i2}.F_{i3}.F_{i4} \\ F_{i0}^{bb} = F_{i5}.F_{i6}.F_{i7}.(1-F_{i8}) \end{cases} \quad (2)$$

For an arm *i*, several complementary control laws are possible. The control law which lets an optimal control of this inverter is:

$$\begin{cases} F_{i5} = 1 - F_{i1} \\ F_{i6} = 1 - F_{i2} \\ F_{i7} = 1 - F_{i3} \\ F_{i8} = 1 - F_{i4} \end{cases} \quad (3)$$

As indicated in Table 1, each arm of the inverter can have five possible switching states P_2, P_1, O, N_1 or N_2.

The output voltage of the inverter relative to the middle point *N* are defined as follow:

$$\begin{bmatrix} v_1 \\ v_2 \\ v_3 \end{bmatrix} = \frac{1}{3}\begin{bmatrix} 2 & -1 & -1 \\ -1 & 2 & -1 \\ -1 & -1 & 2 \end{bmatrix} \left\{ \begin{bmatrix} F_{11}^{bb}+F_{11}^{b} \\ F_{21}^{bb}+F_{21}^{b} \\ F_{31}^{bb}+F_{31}^{b} \end{bmatrix} U_{c2} + \begin{bmatrix} F_{11}^{b} \\ F_{21}^{b} \\ F_{31}^{b} \end{bmatrix} U_{c1} - \begin{bmatrix} F_{10}^{bb}+F_{10}^{b} \\ F_{20}^{bb}+F_{20}^{b} \\ F_{30}^{bb}+F_{30}^{b} \end{bmatrix} U_{c3} - \begin{bmatrix} F_{10}^{b} \\ F_{20}^{b} \\ F_{30}^{b} \end{bmatrix} U_{c4} \right\} \quad (4)$$

Thus, the input current of the inverter are given as follow:

$$\begin{bmatrix} i_{d1} \\ i_{d2} \\ i_{d4} \\ i_{d5} \end{bmatrix} = \begin{bmatrix} F_{11}^{b} & F_{21}^{b} & F_{31}^{b} \\ F_{11}^{bb} & F_{21}^{bb} & F_{31}^{bb} \\ F_{10}^{bb} & F_{20}^{bb} & F_{30}^{bb} \\ F_{10}^{b} & F_{20}^{b} & F_{30}^{b} \end{bmatrix} \begin{bmatrix} i_1 \\ i_2 \\ i_3 \end{bmatrix} \quad (5)$$

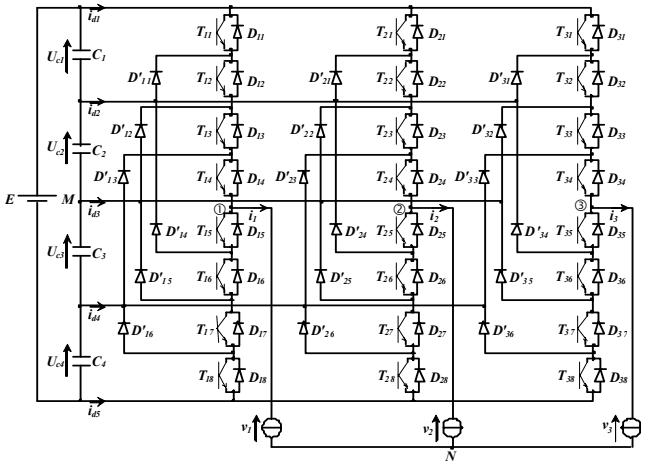

Figure 1. Five levels diode clamped inverter structure

Table 1. States of the five levels diode clamped inverter

State	TD_{i1}	TD_{i2}	TD_{i3}	TD_{i4}	v_{iM}
P_2	1	1	1	1	$U_{c1} + U_{c2}$
P_1	0	1	1	1	U_{c2}
O	0	0	1	1	0
N_1	0	0	0	1	$- U_{c3}$
N_2	0	0	0	0	$- U_{c3} - U_{c4}$

3. SPACE VECTOR MODULATION

The output voltage vector is defined as:

$$v_s = v_1 \,.\, e^{j\,0} + v_2 \,.\, e^{-j\frac{2\pi}{3}} + v_3 \,.\, e^{j\frac{2\pi}{3}} = v_\alpha + j\,.\,v_\beta \quad (6)$$

v_α and v_β are real and imaginary components of v_s in $(\alpha - \beta)$ plan.

This output voltage vector v_s can take several discrete positions in $(\alpha - \beta)$ plan, according to switching states of the inverter arms. These positions are indicated on the space vector diagram, given in Fig. 2. They are identified by combination of switching states of the arms, P_2, P_1, O, N_1 or N_2. For instance, the state P_2ON_1 indicates that the first arm is in state P_2 $(v_{1M} = U_{c1} + U_{c2})$, the second arm is in state O $(v_{2M} = 0)$ and the third arm is in state N_1 $(v_{3M} = -U_{c3})$.

Since each arm has five possible switching states, five levels diode clamped inverter has $5^3 = 125$ state. Some positions of output voltage vector are synthesized by more than one switching state. In Fig. 2, we can find 24 positions with no redundancy, 18 positions with two redundancies, 12 positions with three redundancies and 6 positions with four redundancies.

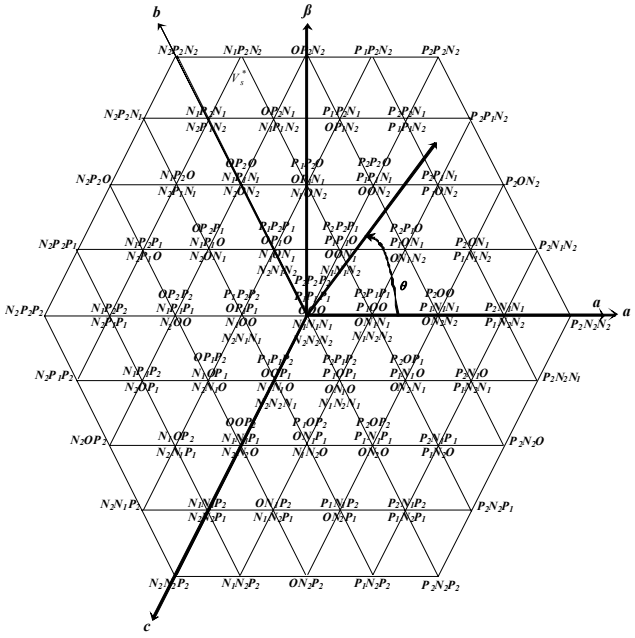

Figure 2. Space vector diagram of five levels inverter

The space vector diagram can be divided into six triangular sectors of 60° length. Each sector can be divided into sixteen small triangular regions.

Given the desired reference phase voltages, we define the reference voltage vector v_s^*, to be generated by the inverter:

$$\begin{aligned} v_s^* &= v_1^* \,.\, e^{j\,0} + v_2^* \,.\, e^{-j\,\frac{2\pi}{3}} + v_3^* \,.\, e^{j\,\frac{2\pi}{3}} \\ &= v_\alpha^* + j \,.\, v_\beta^* \\ &= m \,.\, V_{max} \,.\, e^{j\,\theta} \end{aligned} \tag{7}$$

$m(0 \le m \le 1)$ is the modulation index.

Having the components of the reference voltage vector, we deduce the triangular sector and the triangular region which includes it. During a sampling period T_s, the reference voltage vector v_s^* should be match with the average output vector combined by the three nearest vectors v_x, v_y and v_z, corresponding to the apexes of the triangular region which includes it [10].

4. BALANCING OF INTERMEDIARY CAPACITOR VOLTAGES

One important problem associated with multilevel inverters is imbalance of DC link capacitor voltages, due to currents flow from/to the midpoints between capacitors according to switching states and load conditions [4]. The simplest and most efficient manner to deal with this problem is to use the freedom choice of redundant vectors used to synthesize the output voltage vector. According to load currents, these vectors are distributed such that the DC capacitor voltages are balanced [11]. To do so, we firstly study the effect different redundant vectors on capacitor voltages.

4.1 Relationship between input and output currents

The capacitor currents in the left side of the inverter are expressed as:

$$\begin{cases} i_{c1} = \frac{1}{4}(-2\,i_{d1} + i_{d2} - i_{d4} - 2\,i_{d5}) \\ i_{c2} = \frac{1}{4}(-2\,i_{d1} - 3\,i_{d2} - i_{d4} - 2\,i_{d5}) \\ i_{c3} = \frac{1}{4}(2\,i_{d1} + i_{d2} + 3\,i_{d4} + 2\,i_{d5}) \\ i_{c4} = \frac{1}{4}(2\,i_{d1} + i_{d2} - i_{d4} + 2\,i_{d5}) \end{cases} \tag{8}$$

By replacing the input currents of the inverter by there expressions, we can write:

$$(i_{c1} \,,\, i_{c2} \,,\, i_{c3} \,,\, i_{c4})^t = \frac{1}{4} \,.\, A \,.\, (i_1 \,,\, i_2 \,,\, i_3)^t \tag{9}$$

where

$$A = \begin{bmatrix} -2F_{11}^b + F_{11}^{bb} - F_{10}^{bb} - 2F_{10}^b & -2F_{21}^b + F_{21}^{bb} - F_{20}^{bb} - 2F_{20}^b & -2F_{31}^b + F_{31}^{bb} - F_{30}^{bb} - 2F_{30}^b \\ -2F_{11}^b - 3F_{11}^{bb} - F_{10}^{bb} - 2F_{10}^b & -2F_{21}^b - 3F_{21}^{bb} - F_{20}^{bb} - 2F_{20}^b & -2F_{31}^b - 3F_{31}^{bb} - F_{30}^{bb} - 2F_{30}^b \\ 2F_{11}^b + F_{11}^{bb} + 3F_{10}^{bb} + 2F_{10}^b & 2F_{21}^b + F_{21}^{bb} + 3F_{20}^{bb} + 2F_{20}^b & 2F_{31}^b + F_{31}^{bb} + 3F_{30}^{bb} + 2F_{30}^b \\ 2F_{11}^b + F_{11}^{bb} - F_{10}^{bb} + 2F_{10}^b & 2F_{21}^b + F_{21}^{bb} - F_{20}^{bb} + 2F_{20}^b & 2F_{31}^b + F_{31}^{bb} - F_{30}^{bb} + 2F_{30}^b \end{bmatrix}$$

Table 2. Relationship between capacitor currents and load currents

Vector			$4i_{c1}$	$4i_{c2}$	$4i_{c3}$	$4i_{c4}$	Equation	Group
V_1	a	$P_2N_1N_1$	e	e	e	$-3e$	$e=-i_1$	1
	b	$P_1N_2N_2$	$-3e$	e	e	e		
V_2	a	P_2ON_1	e_1	e_1	e_2	e_3	$e_1=-i_1+i_2$, $e_2=-i_1-3i_2$ $e_3=3i_1+i_2$	2
	b	$P_1N_1N_2$	e_3	e_1	e_1	e_2		
V_3	a	$P_2P_1N_1$	e_1	e_2	e_2	e_3	$e_1=-i_1+2i_2$, $e_2=-i_1-2i_2$ $e_3=3i_1+2i_2$	3
	b	P_1ON_2	e_3	e_1	e_2	e_2		
V_4	a	$P_2P_2N_1$	e	e	e	$-3e$	$e=-i_1-i_2$	1
	b	$P_1P_1N_2$	$-3e$	e	e	e		
V_5	a	$P_1P_2N_1$	e_1	e_2	e_2	e_3	$e_1=2i_1-i_2$, $e_2=-2i_1-i_2$ $e_3=2i_1+3i_2$	3
	b	OP_1N_2	e_3	e_1	e_2	e_2		
V_6	a	OP_2N_1	e_1	e_1	e_2	e_3	$e_1=i_1-i_2$, $e_2=-3i_1-i_2$ $e_3=i_1+3i_2$	2
	b	$N_1P_1N_2$	e_3	e_1	e_1	e_2		
V_7	a	$N_1P_2N_1$	e	e	e	$-3e$	$e=-i_2$	1
	b	$N_2P_1N_2$	$-3e$	e	e	e		
V_8	a	N_1P_2O	e_1	e_1	e_2	e_3	$e_1=-i_1-2i_2$, $e_2=3i_1+2i_2$ $e_3=-i_1+2i_2$	2
	b	$N_2P_1N_1$	e_3	e_1	e_1	e_2		
V_9	a	$N_1P_2P_1$	e_1	e_2	e_2	e_3	$e_1=-2i_1-3i_2$, $e_2=2i_1+i_2$ $e_3=-2i_1+i_2$	3
	b	N_2P_1O	e_3	e_1	e_2	e_2		
v_{10}	a	$N_1P_2P_2$	e	e	e	$-3e$	$e=i_1$	1
	b	$N_2P_1P_1$	$-3e$	e	e	e		
v_{11}	a	$N_1P_1P_2$	e_1	e_2	e_2	e_3	$e_1=i_1+3i_2$, $e_2=i_1-i_2$ $e_3=-3i_1-i_2$	3
	b	N_2OP_1	e_3	e_1	e_2	e_2		
v_{12}	a	N_1OP_2	e_1	e_1	e_2	e_3	$e_1=i_1+2i_2$, $e_2=i_1-2i_2$ $e_3=-3i_1-2i_2$	2
	b	$N_2N_1P_1$	e_3	e_1	e_1	e_2		
v_{13}	a	$N_1N_1P_2$	e	e	e	$-3e$	$e=i_1+i_2$	1
	b	$N_2N_2P_1$	$-3e$	e	e	e		
v_{14}	a	ON_1P_2	e_1	e_1	e_2	e_3	$e_1=2i_1+i_2$, $e_2=-2i_1+i_2$ $e_3=-2i_1-3i_2$	2
	b	$N_1N_2P_1$	e_3	e_1	e_1	e_2		
v_{15}	a	$P_1N_1P_2$	e_1	e_2	e_2	e_3	$e_1=3i_1+i_2$, $e_2=-i_1+i_2$ $e_3=-i_1-3i_2$	3
	b	ON_2P_1	e_3	e_1	e_2	e_2		
v_{16}	a	$P_2N_1P_2$	e	e	e	$-3e$	$e=i_2$	1
	b	$P_1N_2P_1$	$-3e$	e	e	e		
v_{17}	a	$P_2N_1P_1$	e_1	e_2	e_2	e_3	$e_1=-3i_1-2i_2$, $e_2=i_1+2i_2$ $e_3=i_1-2i_2$	3
	b	P_1N_2O	e_3	e_1	e_2	e_2		
v_{18}	a	P_2N_1O	e_1	e_1	e_2	e_3	$e_1=-2i_1-i_2$, $e_2=2i_1+3i_2$ $e_3=2i_1-i_2$	2
	b	$P_1N_2N_1$	e_3	e_1	e_1	e_2		
v_{19}	a	P_2OO	e	e	$-e$	$-e$	$e=-2i_1$	4
	b	$P_1N_1N_1$	$-e$	e	e	$-e$		
	c	ON_2N_2	$-e$	$-e$	e	$-e$		
v_{20}	a	P_2P_1O	e_1	e_2	e_3	e_3	$e_1=-2i_1+i_2$, $e_2=-2i_1-3i_2$ $e_3=2i_1+i_2$	5
	b	P_1ON_1	e_3	e_1	e_2	e_3		
	c	ON_1N_2	e_3	e_3	e_1	e_2		
v_{21}	a	P_2P_2O	e	e	$-e$	$-e$	$e=-2i_1-2i_2$	4
	b	$P_1P_1N_1$	$-e$	e	e	$-e$		
	c	OON_2	$-e$	$-e$	e	$-e$		
v_{22}	a	P_1P_2O	e_1	e_2	e_3	e_3	$e_1=i_1-2i_2$, $e_2=-3i_1-2i_2$ $e_3=i_1+2i_2$	5
	b	OP_1N_1	e_3	e_1	e_2	e_3		
	c	N_1ON_2	e_3	e_3	e_1	e_2		

Vector			$4i_{c1}$	$4i_{c2}$	$4i_{c3}$	$4i_{c4}$	Equation	Group
v_{23}	a	OP_2O	e	e	$-e$	$-e$	$e=-2i_2$	4
	b	$N_1P_1N_1$	$-e$	e	e	$-e$		
	c	N_2ON_2	$-e$	$-e$	e	$-e$		
v_{24}	a	OP_2P_1	e_1	e_2	e_3	e_3	$e_1=-i_1-3i_2$, $e_2=3i_1+i_2$ $e_3=-i_1+i_2$	5
	b	N_1P_1O	e_3	e_1	e_2	e_3		
	c	N_2ON_1	e_3	e_3	e_1	e_2		
v_{25}	a	OP_2P_2	e	e	$-e$	$-e$	$e=2i_1$	4
	b	$N_1P_1P_1$	$-e$	e	e	$-e$		
	c	N_2OO	$-e$	$-e$	e	$-e$		
v_{26}	a	OP_1P_2	e_1	e_2	e_3	e_3	$e_1=2i_1+3i_2$, $e_2=2i_1-i_2$ $e_3=-2i_1-i_2$	5
	b	N_1OP_1	e_3	e_1	e_2	e_3		
	c	N_2N_1O	e_3	e_3	e_1	e_2		
v_{27}	a	OOP_2	e	e	$-e$	$-e$	$e=2i_1+2i_2$	4
	b	$N_1N_1P_1$	$-e$	e	e	$-e$		
	c	N_2N_2O	$-e$	$-e$	e	$-e$		
v_{28}	a	P_1OP_2	e_1	e_2	e_3	e_3	$e_1=3i_1+2i_2$, $e_2=-i_1+2i_2$ $e_3=-i_1-2i_2$	5
	b	ON_1P_1	e_3	e_1	e_2	e_3		
	c	N_1N_2O	e_3	e_3	e_1	e_2		
v_{29}	a	P_2OP_2	e	e	$-e$	$-e$	$e=2i_2$	4
	b	$P_1N_1P_1$	$-e$	e	e	$-e$		
	c	ON_2O	$-e$	$-e$	e	$-e$		
v_{30}	a	P_2OP_1	e_1	e_2	e_3	e_3	$e_1=-3i_1-i_2$, $e_2=i_1+3i_2$ $e_3=i_1-i_2$	5
	b	P_1N_1O	e_3	e_1	e_2	e_3		
	c	ON_2N_1	e_3	e_3	e_1	e_2		
v_{31}	a	$P_2P_1P_1$	$-3e$	e	e	e	$e=i_1$	6
	b	P_1OO	e	$-3e$	e	e		
	c	ON_1N_1	e	e	$-3e$	e		
	d	$N_1N_2N_2$	e	e	e	$-3e$		
v_{32}	a	$P_2P_2P_1$	$-3e$	e	e	e	$e=i_1+i_2$	6
	b	P_1P_1O	e	$-3e$	e	e		
	c	OON_1	e	e	$-3e$	e		
	d	$N_1N_1N_2$	e	e	e	$-3e$		
v_{33}	a	$P_1P_2P_1$	$-3e$	e	e	e	$e=i_2$	6
	b	OP_1O	e	$-3e$	e	e		
	c	N_1ON_1	e	e	$-3e$	e		
	d	$N_2N_1N_2$	e	e	e	$-3e$		
v_{34}	a	$P_1P_2P_2$	$-3e$	e	e	e	$e=-i_1$	6
	b	OP_1P_1	e	$-3e$	e	e		
	c	N_1OO	e	e	$-3e$	e		
	d	$N_2N_1N_1$	e	e	e	$-3e$		
v_{35}	a	$P_1P_1P_2$	$-3e$	e	e	e	$e=-i_1-i_2$	6
	b	OOP_1	e	$-3e$	e	e		
	c	N_1N_1O	e	e	$-3e$	e		
	d	$N_2N_2N_1$	e	e	e	$-3e$		
v_{36}	a	$P_2P_1P_2$	$-3e$	e	e	e	$e=-i_2$	6
	b	P_1OP_1	e	$-3e$	e	e		
	c	ON_1O	e	e	$-3e$	e		
	d	$N_1N_2N_1$	e	e	e	$-3e$		

Table 3. Effect of redundant vectors on capacitor voltages

Group	Possibility	a				b				c				d			
		U_{c1}	U_{c2}	U_{c3}	U_{c4}	U_{c1}	U_{c2}	U_{c3}	U_{c4}	U_{c1}	U_{c2}	U_{c3}	U_{c4}	U_{c1}	U_{c2}	U_{c3}	U_{c4}
6	P_1	↓	↑	↑	↑	↑	↓	↑	↑	↑	↑	↓	↑	↑	↑	↑	↓
	P_2	↑	↓	↓	↓	↓	↑	↓	↓	↓	↓		↓	↓	↓	↓	↑
5	P_1	↓	↓	↑	↑	↑	↓	↓	↑	↑	↑	↓	↓				
	P_2	↓	↑	↓	↓	↓	↓	↑	↓	↓	↓	↓	↑				
	P_3	↓	↑	↑	↑	↑	↓	↑	↑	↑	↑	↓	↑				
	P_4	↑	↓	↓	↓	↓	↑	↓	↓	↓	↓	↑	↓				
	P_5	↑	↓	↑	↑	↑	↑	↓	↑	↑	↑	↑	↓				
	P_6	↑	↑	↓	↓	↓	↑	↑	↓	↓	↓	↑	↑				
4	P_1	↑	↑	↓	↓	↓	↑	↑	↓	↓	↓	↑	↑				
	P_2	↓	↓	↑	↑	↑	↓	↓	↑	↑	↑	↓	↓				
3	P_1	↓	↓	↓	↑	↑	↓	↓	↓								
	P_2	↓	↑	↑	↓	↓	↓	↑	↑								
	P_3	↓	↑	↑	↑	↑	↓	↑	↑								
	P_4	↑	↓	↓	↓	↓	↑	↓	↓								
	P_5	↑	↓	↓	↑	↑	↑	↓	↓								
	P_6	↑	↑	↑	↓	↓	↑	↑	↑								
2	P_1	↓	↓	↓	↑	↑	↓	↓	↓								
	P_2	↓	↑	↑	↓	↓	↓	↑	↑								
	P_3	↓	↓	↑	↑	↑	↓	↓	↑								
	P_4	↑	↑	↓	↓	↓	↑	↑	↓								
	P_5	↑	↑	↓	↑	↑	↑	↑	↓								
	P_6	↑	↑	↑	↓	↓	↑	↑	↑								
1	P_1	↑	↑	↑	↓	↓	↑	↑	↑								
	P_2	↓	↓	↓	↑	↑	↓	↓	↓								

Table 4. Selection of redundancies

Group		1		2						3						4		5						6	
Possibility / Deviation case		P_1	P_2	P_1	P_2	P_3	P_4	P_5	P_6	P_1	P_2	P_3	P_4	P_5	P_6	P_1	P_2	P_1	P_2	P_3	P_4	P_5	P_6	P_1	P_2
C_1	$U_{c1}<U_{c2}<U_{c3}<U_{c4}$	a	b	b	a	b	a	b	a	b	a	b	a	b	a	a	c	c	a	c	a	c	a	d	a
C_2	$U_{c1}<U_{c2}<U_{c4}<U_{c3}$	a	b	b	b	b	a	a	a	b	a	b	a	b	a	a	c	c	a	c	a	b	a	c	a
C_3	$U_{c1}<U_{c3}<U_{c2}<U_{c4}$	a	b	b	a	b	a	b	a	b	a	b	a	b	a	a	c	c	b	b	a	c	a	d	a
C_4	$U_{c1}<U_{c3}<U_{c4}<U_{c2}$	a	b	b	a	b	a	b	a	b	b	b	a	a	a	a	b	b	b	b	a	a	a	b	a
C_5	$U_{c1}<U_{c4}<U_{c2}<U_{c3}$	a	b	b	b	b	a	a	a	b	b	b	a	a	a	a	b	b	c	c	a	b	a	c	a
C_6	$U_{c1}<U_{c4}<U_{c3}<U_{c2}$	a	b	b	b	b	a	a	a	b	b	b	a	a	a	a	b	b	c	b	a	a	a	b	a
C_7	$U_{c2}<U_{c1}<U_{c3}<U_{c4}$	a	b	b	a	b	a	b	a	b	a	a	b	b	a	a	c	c	a	c	b	b	a	d	b
C_8	$U_{c2}<U_{c1}<U_{c4}<U_{c3}$	a	b	b	b	b	a	a	a	b	a	a	b	b	a	a	c	c	a	c	b	c	a	c	b
C_9	$U_{c2}<U_{c3}<U_{c1}<U_{c4}$	a	b	b	a	a	b	b	a	b	a	a	b	b	a	b	c	c	a	a	b	c	b	d	b
C_{10}	$U_{c2}<U_{c3}<U_{c4}<U_{c1}$	b	a	a	a	a	b	b	b	a	a	a	b	b	b	b	c	c	a	a	b	b	b	a	b
C_{11}	$U_{c2}<U_{c4}<U_{c1}<U_{c3}$	b	a	a	b	b	a	a	b	a	a	a	b	b	b	a	c	c	a	c	b	b	a	c	b
C_{12}	$U_{c2}<U_{c4}<U_{c3}<U_{c1}$	b	a	a	b	a	b	a	b	a	a	a	b	b	b	b	c	c	a	a	b	c	b	a	b
C_{13}	$U_{c3}<U_{c1}<U_{c2}<U_{c4}$	a	b	b	a	a	b	b	a	b	a	b	a	b	a	b	a	a	b	b	c	a	b	d	c
C_{14}	$U_{c3}<U_{c1}<U_{c4}<U_{c2}$	a	b	b	a	a	b	b	a	b	b	b	a	a	a	c	a	a	b	b	c	c	c	b	c
C_{15}	$U_{c3}<U_{c2}<U_{c1}<U_{c4}$	a	b	b	a	a	b	b	a	b	a	a	b	b	a	b	a	a	b	a	c	c	b	d	c
C_{16}	$U_{c3}<U_{c2}<U_{c4}<U_{c1}$	b	a	a	a	a	b	b	b	a	a	a	b	b	b	b	a	a	b	a	c	a	b	a	c
C_{17}	$U_{c3}<U_{c4}<U_{c1}<U_{c2}$	b	a	a	a	a	b	b	b	a	b	b	a	a	b	c	a	a	b	b	c	a	c	b	c
C_{18}	$U_{c3}<U_{c4}<U_{c2}<U_{c1}$	b	a	a	a	b	a	b	b	a	b	a	b	a	b	b	a	a	b	a	c	a	b	a	c
C_{19}	$U_{c4}<U_{c1}<U_{c2}<U_{c3}$	b	a	a	b	b	a	a	b	a	b	b	a	a	b	c	b	b	c	c	a	b	c	c	d
C_{20}	$U_{c4}<U_{c1}<U_{c3}<U_{c2}$	b	a	a	b	b	a	a	b	a	b	b	a	a	b	c	b	b	c	b	a	a	c	b	d
C_{21}	$U_{c4}<U_{c2}<U_{c1}<U_{c3}$	b	a	a	b	a	b	a	b	a	b	a	b	a	b	c	b	b	c	c	b	b	c	c	d
C_{22}	$U_{c4}<U_{c2}<U_{c3}<U_{c1}$	b	a	a	b	a	b	a	b	a	b	a	b	a	b	c	a	a	c	a	b	b	c	a	d
C_{23}	$U_{c4}<U_{c3}<U_{c1}<U_{c2}$	b	a	a	b	a	b	a	b	a	b	b	a	a	b	c	a	a	c	b	c	a	c	b	d
C_{24}	$U_{c4}<U_{c3}<U_{c2}<U_{c1}$	b	a	a	b	a	b	a	b	a	b	a	b	a	b	c	a	a	c	a	c	a	c	a	d

4.2 Groups of redundant vectors

This relationship between capacitor currents i_{cj} ($j = 1…4$) and load currents i_i ($i = 1…3$) depends on the switching states of the inverter, in other words, depends on the output redundant vector. Table 2 resume relationships between load and capacitor currents for all the redundant vectors of the space vector diagram. Depending on the forms of these relationships (equations e, e_1, e_2 and e_3), we distinguish six groups of redundant vectors (see Table 2).

4.3 Effect of redundant vectors on capacitor voltages

Redundant vectors of each group can charge or discharge DC link capacitors, depending on load conditions, in other words on sign of equations e, e_1, e_2 and e_3.

For groups with one equation e (groups 1, 4 and 6), we have two possibilities of load conditions:

$$\begin{cases} P_1 : e > 0 \\ P_2 : e < 0 \end{cases} \tag{10}$$

For groups with three equations e_1, e_2 and e_3 (groups 2, 3 and 5), we have six possibilities of load:

$$\begin{cases} P_1 : e_1 < 0 , e_2 < 0 \text{ and } e_3 > 0 \\ P_2 : e_1 < 0 , e_2 > 0 \text{ and } e_3 < 0 \\ P_3 : e_1 < 0 , e_2 > 0 \text{ and } e_3 > 0 \\ P_4 : e_1 > 0 , e_2 < 0 \text{ and } e_3 < 0 \\ P_5 : e_1 > 0 , e_2 < 0 \text{ and } e_3 > 0 \\ P_6 : e_1 > 0 , e_2 > 0 \text{ and } e_3 < 0 \end{cases} \tag{11}$$

Each redundant vector can increase or decrease capacitor voltages, depending on the sign of capacitor currents. Table 3 shows the effect of redundant vectors on capacitor voltages. Signs (↑) and (↓) indicate increasing or decreasing voltage.

4.4 Choice of redundancies

For each case of redundancy, the vector which tends to cancel the unbalance in capacitor voltages will be selected. In other words, we select the vector which charge the undercharged capacitors, and discharge the overcharged ones.

To do so, we must measure capacitor voltages and their deviation case. Since there are four capacitors, we get 24 deviation cases (4x3x2), (C_1 through C_{24}).

For each group of redundancies, given the deviation case (C_m, $m = 1…24$) and load conditions (P_n, $n = 1, 2$ or $1…6$), the vector that will decrease the largest capacitor voltage and (if possible) increases the smallest capacitor voltage is selected.

For instance, let consider the first deviation case (C_1) and the first group of redundant vectors (group 1). The smallest voltage is U_{c1}, and the largest voltage is U_{c4}. From Table 3, if the load is in condition P_1 ($e > 0$), the redundancy a must be selected to increase U_{c1} and decrease U_{c4}, while if the load condition is in condition P_2 ($e < 0$), the redundancy b must be selected.

Table 4 shows the choices of redundancies in all operation conditions of the inverter.

4.5 Simulation results

Without use of balancing algorithm, see Fig. 3, DC bus voltages go away from the equilibrium conditions which are: $U_{c1} = U_{c2} = U_{c3} = U_{c4} = 200$ V. When the balancing algorithm is introduced, see Fig. 4, it is clear that after a transient period of 0.75 sec, capacitor voltages are kept in balancing conditions.

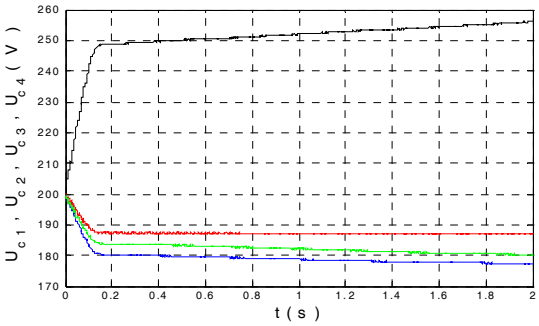

Figure 3. Capacitor voltages without balancing control

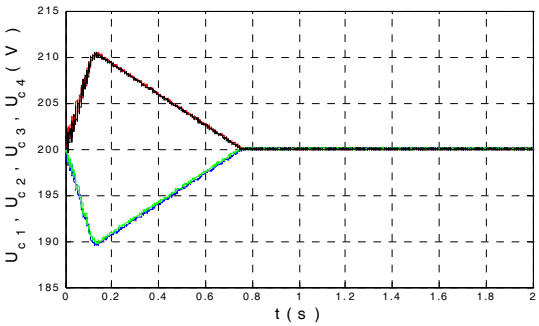

Figure 4. Capacitor voltages with balancing control

5. DC SUPPLY WITH TWO LEVELS RECTIFIER

Until now, we have supposed the input DC voltage of the inverter constant. In this part, we study a generation input DC voltage technique. For this, we propose a cascade constituted by a two levels rectifier - five levels diode clamped inverter which feeds an induction motor, see Fig. 5.

5.1 Modeling and control strategy of two levels rectifier

The two levels rectifier is constituted by three arms corresponding to each phases.

The complementary command of this rectifier is:

$$F_{i2} = 1 - F_{i1}, \quad (i = A, B, C) \tag{12}$$

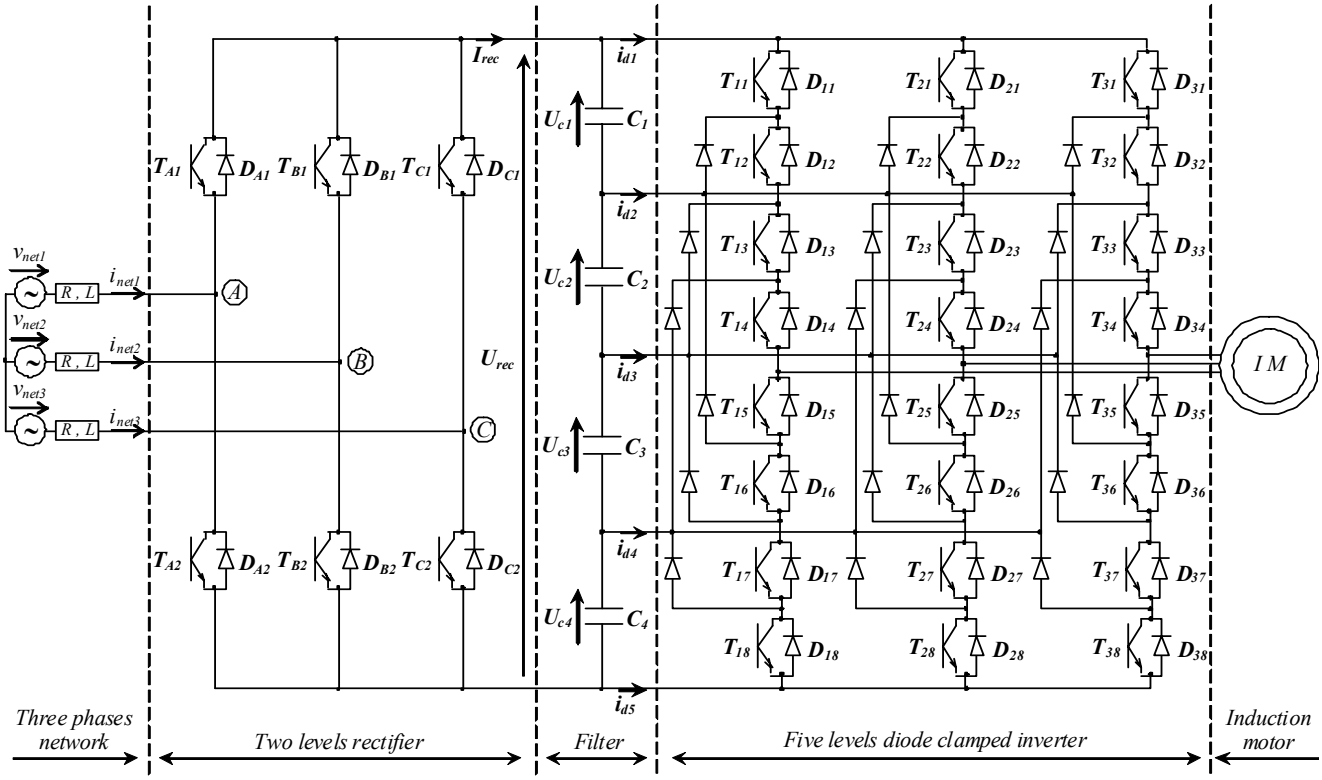

Figure 5. Cascade: two levels rectifier - five levels diode clamped inverter - induction motor

The rectifier output voltages are given by the following expressions:

$$\begin{bmatrix} V_A \\ V_B \\ V_C \end{bmatrix} = \frac{1}{3}\begin{bmatrix} 2 & -1 & -1 \\ -1 & 2 & -1 \\ -1 & -1 & 2 \end{bmatrix}\begin{bmatrix} F_{A1} \\ F_{B1} \\ F_{C1} \end{bmatrix} U_{rec} \qquad (13)$$

The output current can be written as follow:

$$I_{rec} = F_{A1}.i_{net1} + F_{B1}.i_{net2} + F_{C1}.i_{net3} \qquad (14)$$

To control this rectifier, we use the current hysteresis strategy. The principle of this strategy consists to compare the reference currents i_{refk} with the network currents i_{netk} and to deduce the switches state by using the following algorithm:

$$\begin{cases} if\ \ \varepsilon_k > \Delta\,\mathrm{i} \ \ : \ \ F_{i1} = 0 \\ if\ \ \varepsilon_k < \Delta\,\mathrm{i} \ \ : \ \ F_{i1} = 1 \\ \text{elseif} \ \ : \ \ \text{do not change the switches state} \end{cases} \qquad (15)$$

where:
$$\begin{cases} \Delta i : \text{is the width of the hysterisis band} \\ \varepsilon_k = i_{refk} - i_{netk},\ (k = 1, 2, 3) \\ i_{refk} = \sqrt{2} I_e \sin\left(\omega t - \dfrac{2(k-1)\pi}{3}\right),\ (k = 1, 2, 3) \end{cases}$$

5.2 Modeling of the intermediate filter

The intermediate filter is defined by the following equations, see Fig. 5:

$$\begin{cases} C_1 \dfrac{dU_{c1}}{dt} = I_{rec} - i_{d1} \\ C_2 \dfrac{dU_{c2}}{dt} = I_{rec} - i_{d1} - i_{d2} \\ C_3 \dfrac{dU_{c3}}{dt} = I_{rec} + i_{d4} + i_{d5} \\ C_4 \dfrac{dU_{c4}}{dt} = I_{rec} + i_{d5} \end{cases} \qquad (16)$$

5.3 Simulation results

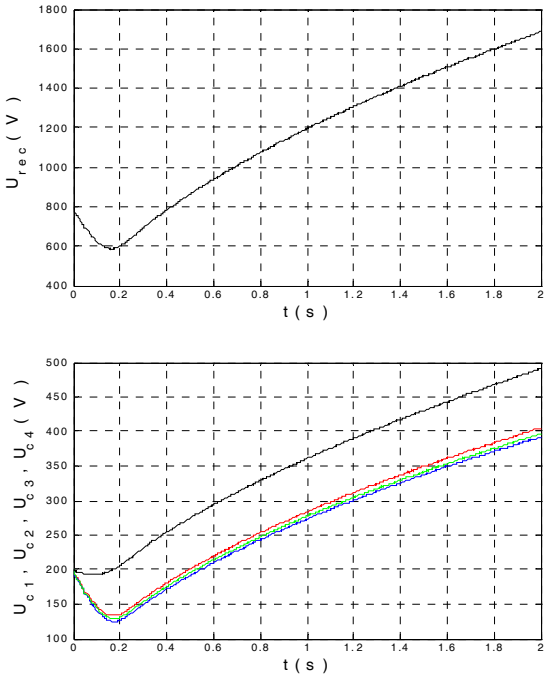

Figure 6. Rectifier output voltage and capacitor voltages without balancing control

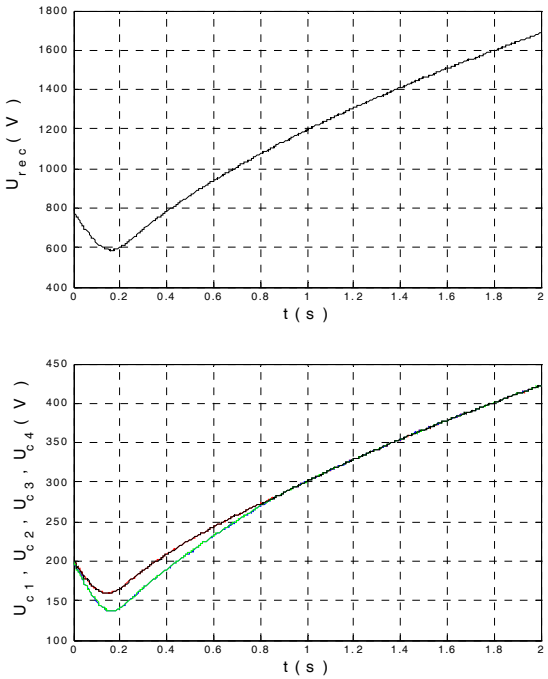

Figure 7. Rectifier output voltage and capacitor voltages with balancing control

Without balancing control, the output voltage of the two levels rectifier increases continually and the capacitor voltages are not constant, see Fig. 6. By introducing the balancing control, we can balance the capacitor voltages, but the rectifier output voltage remain always increasing, see Fig. 7.

6. DC VOLTAGE STABILIZATION

6.1 Voltage loop model

The modeling of this loop, see Fig. 8, is based on the principle of instantaneous power conservation with no loss hypothesis. This loop imposes efficacy network reference current.

The input and output power are calculated as:

$$\begin{cases} P_{input} = \sum_{k=1}^{3}\left(v_{netk}.i_{netk} - R.i_{netk}^2 - \frac{L}{2}\frac{di_{netk}^2}{dt} \right) \\ P_{output} = U_{rec}.I_{rec} = U_{rec}.(i_c + i_{load}) \end{cases} \quad (17)$$

By neglecting Joule losses and assuming sinusoidal grid currents, we get:

$$\sum_{k=1}^{3} v_{netk}.i_{netk} = \frac{L}{2}\sum_{k=1}^{3}\frac{di_{netk}^2}{dt} + U_{rec}.I_{rec} \quad (18)$$

We supposed the network current sinusoidal and in phase with corresponding voltage, we can write:

$$3.V_e.I_e = U_{rec}.I_{rec} \Rightarrow I_{rec} = \frac{3.V_e.I_e}{U_{rec}} \quad (19)$$

where V_e is the rms value of grid voltages, I_e is the rms value of grid currents.

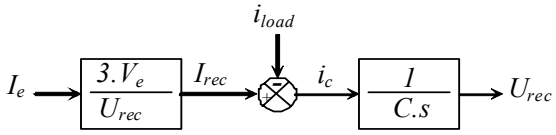

Figure 8. Voltage loop model

6.2 Sliding mode control

From Eq. (16), we can write:

$$\dot{U}_{rec} = \frac{I_{rec} - i_{load}}{C} \quad (20)$$

where

$$i_{load} = \frac{i_{d1} + 2\,.\,i_{d2} - i_{d4} - 2\,.\,i_{d5}}{4}$$

While combining Eq. (19) and (20), we obtain:

$$\dot{U}_{rec} = \frac{\frac{3 \,.\, V_e \,.\, I_e}{U_{rec}} - i_{load}}{C} \tag{21}$$

We would stabilize the rectifier output voltage. For that, we choose the sliding surface as follow:

$$S = U_{ref} - U_{rec} \tag{22}$$

Its derivative is:

$$\dot{S} = -\dot{U}_{rec} \tag{23}$$

The condition $S \cdot \dot{S} < 0$ assures the attraction of the trajectory toward the sliding surface [13]. To verify this condition, it's sufficient to choose:

$$\dot{S} = -k_1 \,.\, sign\,(S) - k_2 \,.\, S \tag{24}$$

where k_1, k_2 are positives constants.

Finally, we obtain:

$$I_e = \left[C \cdot \left(k_1 . sign\,(U_{ref} - U_{rec}) + k_2 (U_{ref} - U_{rec})\right) + i_{load}\right] \cdot \frac{4 \,.\, U_{rec}}{3 \,.\, V_e} \tag{25}$$

The general principle stabilization of two levels rectifier output voltage is shown in Fig. 9.

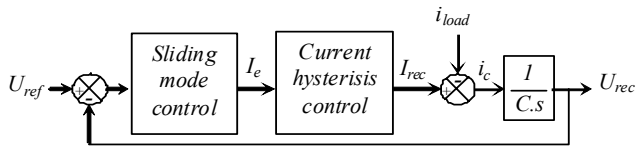

Figure 9. Stabilization algorithm of two levels rectifier output voltage

6.3 Application of stabilization algorithm of rectifier for the proposed cascade

We practice the algorithm stabilization elaborated previously, see Fig. 9, to control the rectifier of the cascade. The two levels rectifier is controlled by the current hysteresis strategy when the network reference currents amplitude feeding the rectifier is imposed by the voltage loop. The rectifier output voltage became constant and stable, see Fig. 10 and 11. The application of the balancing control permits to eliminate the unbalancing problem, and the capacitor voltages became all equal, see Fig. 11.

7. CONCLUSIONS

In this paper, we have studied the stability problem of the input DC link capacitors voltages in the five levels diode clamped inverter.

Firstly, we have assumed that the input DC voltage is constant and we have presented an algorithm for self balancing of DC link capacitors voltages using redundant vectors of the space vector PWM strategy. A comprehensive analysis of the DC link capacitor voltages balancing is presented using redundant vectors. Based on the measurement of load currents and determination of capacitor currents signs, the desirable redundant vector is detected. The validity of this algorithm is proved via simulation results.

Secondly, we have proposed to generate the input DC voltage by a two levels rectifier. We note the instability of the rectifier output voltage. We note that, the upper input DC voltages of the inverter are practically not equals to the lower one. This fact accentuates the problem of unbalance of the different input DC voltages sources of the five levels diode clamped inverter. To resolve these problems, we propose to stabilize the rectifier output voltage using the sliding mode control and to balance the DC link capacitors voltages using the algorithm for self balancing which uses redundant vectors of the space vector PWM strategy. The results obtained with this solution are so promising to stabilize the input DC voltages of the five levels diode clamped inverter, and to use this inverter in high voltage and great power applications such as electrical traction.

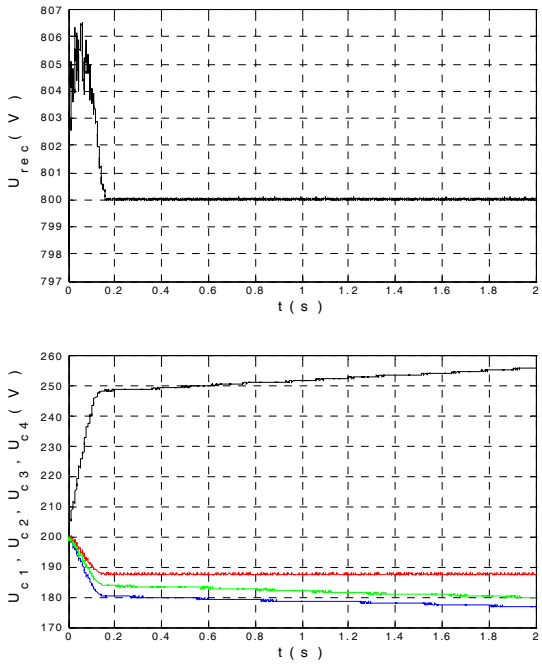

Figure 10. Rectifier output voltage and capacitor voltages without balancing control

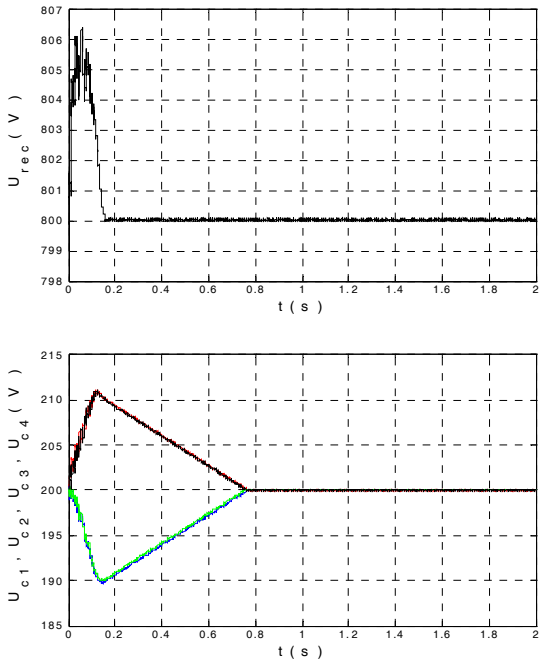

Figure 11. Rectifier output voltage and capacitor voltages with balancing control

Table 5. Simulation parameters

DC supply voltage	$E = 800\ V$
Space vector PWM	$m = 0.9$, $T_s = 166\ 10^{-6}\ s$
Induction motor	$p = 2$, $f = 50\ Hz$, $R_s = 4.85\ \Omega$, $R_r = 3.805\ \Omega$, $L_s = L_r = 0.274$, $M = 0.258\ H$
Filter	$C_1 = C_2 = C_3 = C_4 = C = 20\ mF$
Current hysterisis strategy	$\Delta i = 0.1\ A$, $I_e = 5\ A$ (without stabilization)
Three phases network	$V_e = 220\ V$, $R = 0.25\ \Omega$, $L = 10\ mH$
Sliding mode control	$k_1 = 40$, $k_2 = 20$

REFERENCES

[1] H. Gheraia, E. M. Berkouk, G. Manesse, “Modelling and Control of Seven Levels NPC Voltage Source Inverter: Application to High Power Induction Machine Drive”, European Physical Journal, Vol. 15, 2001, pp. 105-115.

[2] W. H. Liu, Q. Song, “6 kV / 1800 kVA Medium Voltage Drive With NPC Three-Level Inverter Using IGCTs”, Proc. IEEE Applied Power Electronics Conf. and Exposition, APEC2003, 9-13 Feb 2003, Vol. 1, pp.233-237.

[3] J. Rodriguez, J. S. Lai, F. Z. Peng, “Multilevel Inverters: A Survey of Topologies, Controls and Applications”, IEEE Transactions on Industrial Electronics, Vol. 49, No. 4, Aug. 2002, pp. 724-736.

[4] S. K. Mazumder, “A Novel Discrete Control Strategy for Independent Stabilization of Parallel Three-Phase Boost Converters by Combining Space-Vector Modulation With Variable-Structure Control”, IEEE Transactions on Power Electronics, Vol. 18, No. 4, July 2003, pp. 1070-1084.

[5] T. Ishida, K. Matsuse, T. Miyamoto, L. Huang, “Fundamental Characteristics of Five-Level Double Converters with Adjustable DC Voltages for Induction Motor Drives”, IEEE Transactions on Industrial Electronics, Vol. 49, No. 4, Aug. 2002, pp. 775-782.

[6] X. Wu, Y. Liu, L. Huang, “A Novel Space Vector Modulation Algorithm for Three-Level PWM Voltage Source Inverter”, Proc. IEEE Conf. on Computers, Communications, Control and Power Engineering, 28-31 Oct. 2002, TENCON'02, Vol. 3, pp. 1974-1977.

[7] Y. Liu, X. Wu, L. Huang, “Implementation of Three-Level Inverter Using a Novel Space Vector Modulation Algorithm”, Proc. IEEE Conf. on Power System Technology, PowerCon 2002, 13-17 Oct. 2002, Vol. 1, pp. 606-610.

[8] S. Wei, B. Wu, “A General Space Vector PWM Control Algorithm for Multilevel Inverters”, Eighteenth Annual IEEE on Applied Power Electronics Conf. and Exposition, APEC'03, 9-13 Feb 2003, Vol. 1, pp.562-568.

[9] A. Talha, E. M. Berkouk, M. S. Boucherit, “Study and Control of Two-Level PWM Rectifier-Clamping Bridge-Seven-Level NPC VSI Cascade: Application to PMSM Speed Control”, European Transactions on Electrical Power, Vol. 16, No. 1, Oct. 2005, pp. 93-107.

[10] O. Bouhali, B. Francois, E. M. Berkouk, C. Saudemont, “DC Link Capacitor Voltage Balancing in a Three-Phase Diode Clamped Inverter Controlled by a Direct Space Vector of Line-to-Line Voltages”, IEEE Transactions on Power Electronics, Vol. 22, No. 5, Sep. 2007, pp.1636-1648.

[11] J. Pou, R. Pindado, D. Boroyevich, P. Rodriguez, J. Vicente, “Voltage-Balancing Strategies for Diode-Clamped Multilevel Converters”, 35th Annual IEEE Power Electronics Specialists Conference, Aachen, Germany, 2004, pp. 3988-3993.

[12] S. Barkati, E. M. Berkouk, M. S. Boucherit, “Control of the DC Buses of a Seven-Level Diode-Clamped Inverter Using Type-2 Fuzzy Systems”, Mediterranean Journal of Measurement and Control, Vol. 2, No. 4, Oct. 2006, pp. 161-168.

[13] R. Chibani, G. Manesse, E. M. Berkouk, “A New Solution to the Unbalance Problem of the Input DC Voltages of a Five Levels NPC VSI by Using Sliding Mode Regulation”, 10th International Power Electronics and Motion Control, EPE-PEMC2002, Cavtat and Dubrovnik, Croatia, 2002.

[14] D. Lalili, E. M. Berkouk, F. Boudjema, N. Lourci, “Simplified Space Vector PWM Algorithm for Three-Level Inverter with Neutral Point Potential Control”, Mediterranean Journal of Measurement and Control, Vol. 3, No. 1, Jan. 2007, pp. 30-39.

[15] D.W. Kang, Y. H. Lee, B. S. Suh, C. H. Choi, D. S. Hyun, “An Improved Carrier-Based SVPWM Method Using Leg Voltage Redundancies in Generalized Cascaded Multilevel Inverter Topology”, IEEE Transactions on Power Electronics, Jan. 2003, Vol. 18, No. 1, pp. 180-187.

Biographies

Nabil Lourci was born in Jijel, Algeria, on 1976. He received the engineering degree and the master degree in Power Electronics from national polytechnic school of Algeria, in 1998 and 2000 respectively. Since 2001, he has been a lecturer in the Electrical Engineering department of Jijel University, Algeria. He is a researcher in electrical system study and modeling laboratory (LAMEL) at Jijel University. He is working in the field of power electronics, electrical drives, and renewable energy.

El Madjid Berkouk was born in Algeria, on 1968. He received his Engineering degree in 1991 in Electrical Engineering from the Polytechnic National School of Algiers, Algeria. In 1992 and 1995 he obtained, respectively, a Master of Science from ENSEEIHT (Toulouse) and Ph.D. from CNAM (Paris). From 1992 to 1996, he was teaching at the University of Paris XI. Since 1996, he is with the Polytechnic National school of Algiers as a Professor. His current research interests are power electronics and electrical drives.

Djaafer Lalili was born in Jijel, Algeria, on 1973. He received the engineering degree and the master degree in Power Electronics from national polytechnic school of Algeria, in 1996 and 1999 respectively. Since 2000, he has been a lecturer in the Electrical Engineering department of Jijel University, Algeria. He is a researcher in electrical system study and modeling laboratory (LAMEL) at Jijel University. He is working in the field of power electronics, electrical drives, and renewable energy.

NEW I-V CHARACTERIZATION MODEL FOR PHOTOVOLTAIC MODULES AND EXPERIMENTAL DETERMINATION OF INTERNAL RESISTANCES

M. Benghanem [1], S. N. Alamri [1], A. Mellit [2,*]

[1] Department of Physics, Faculty of Sciences, Taibah University, Medina, KSA

[2] Department of Electronics, Faculty of Sciences Engineering, LAMEL Laboratory, Jijel University, Algeria

ABSTRACT

In this paper, an explicit model for accurate simulation of the I-V characteristic of photovoltaic (PV) cells and modules under various climatic conditions is described. The proposed model is found to be reliable and accurate in the situations where the model is a good approximation of cell or module performance. The developed model has been compared with the traditional I-V characteristic and with some experimental results. The obtained results showed the effectiveness of our model. Moreover, an experimental method is proposed to determine the series resistance and shunt resistance of the PV cells and modules.

Keywords

I-V Characterization, Explicit Model, Simulation, Photovoltaic, Experimental Measurement, Series Resistance, Shunt Resistance.

1. INTRODUCTION

Photovoltaic involves the direct conversion of sunlight into electricity in thin layers of material known as semiconductors with properties intermediate between those of metals and insulators. Silicon, the material of microelectronics and the information age, is the most common semiconductor. In the latter half of the 20th century, silicon photovoltaic solar cells started to be used mainly to generate small amounts of electricity in remote areas where there was no conventional source of electricity. In the 21st century, photovoltaics will grow to maturity [1]. Estimation of the current-voltage (I-V) equation parameters is one of the most important tasks performed on solar cells and photovoltaic (PV) modules. Many techniques have been suggested and used to extract solar cells parameters. Probably, within those methods, curve-fitting technique is the most used. The basis of this technique is the determination of solar cells parameters from a wide set of measured coordinates. A higher level of confidence is obtained by applying error analysis and standard deviation calculations to curve fitting techniques as can be seen in [2-4].

*Corresponding author: *E-mail:* a.mellit@yahoo.co.uk

 ISSN: 1743-9310

To carry out efficient photovoltaic engineering, a suitable characterization of PV module electrical behavior (I-V curves) is necessary. Nevertheless, it is possible to predict PV module behavior under natural sunlight, through numerical or algebraic methods [5-9].

The determination of solar cell model parameters from experimental data is important in the design and evaluation of solar cells. The work described in this paper is to characterize the photovoltaic modules in real conditions. In addition, we give a method to determine the serial resistance R_S and the shunt resistance R_{Sh} of PV module. The serial resistance is mainly the sum of contact resistance on the front and back surfaces and the resistances of the bulk and the diffused layer on the top. The shunt resistance represents a parallel high-conductivity path across the p-n junction. The shunt resistance can affect the short-circuit current I_{SC} density as well. The PV performance depends on the values of R_{Sh} and R_S.

The resistances R_S and R_{Sh} need to be recognized and understood in order to analyze the cell and module performance. The most commonly used method for measuring the series resistance of a solar cell was firstly proposed by wolf and Rauschenbach [10]. This involves the measuring of the characteristic of a cell at two different illuminations.

Several other methods are available in the literature for the measurement of series and shunt resistances [11-15]. All these methods are based on single exponential model of solar cell, they assume that R_{Sh} is infinite and presume R_S to be independent of the intensity of illumination which may not be valid.

In this paper, firstly, we propose a new explicit model to simulate the I-V characterization by given a photovoltaic resistance for any materials properties of the solar cell. The photovoltaic resistance is given for silicon cell. Subsequently, we present an experimental method for determining and computing of both resistances R_S and R_{Sh} of a solar cell using the I-V characteristic based on the proposed explicit model.

This paper is organized as follows: A review of existing model for solar cell characteristic is presented in the next section. Section 3 provides a comparison between different models (explicit model, four parameters model and five parameters model). The proposed explicit model is described in Section 4, while an experimental method for calculation of R_S and R_{Sh} is given in the final section.

2. REVIEW OF EXISTING MODELS OF SOLAR CELL CHARACTERISTIC

Several models of PV module have been developed in literature [5-15]. The aim is to get the I-V characteristic in order to analyze and evaluate the PV systems performance. The difference between all models is the number of necessary

parameters used in the computational analysis. The most models used are:

- Explicit model
- Solar cell model using four parameters
- Solar cell model using five parameters
- Solar cell model using two exponential

2.1 Explicit model

This model needs four input parameters: the short-circuit current I_{SC}, the open-circuit voltage V_{OC}, the maximal current I_m, and the maximal voltage V_m [11]. The relation between the current I and the output voltage V is given by:

$$I = I_{SC}\left[1 - C_1\left(Exp\left(\frac{V}{C_2 . V_{OC}}\right) - 1\right)\right] \quad (1)$$

where

$$C_1 = \left(1 - \frac{I_m}{I_{SC}}\right).Exp\left(\frac{-V_m}{C_2.V_{OC}}\right)$$

and

$$C_2 = \frac{\frac{V_m}{V_{OC}} - 1}{Ln\left(1 - \frac{I_m}{I_{SC}}\right)}$$

2.2 Solar cell model using four parameters

The classical equation describing the I-V curve of a single solar cell is given by:

$$I = I_{Ph} - I_0.\left[Exp\left(\frac{q}{A.K.T}(V + R_S.I)\right) - 1\right] \quad (2)$$

Where I is the load current and V the output voltage, I_0 is the diode reverse saturation current, I_{Ph} is the photo-generated current, R_S is the series resistance, q is the electric charge, K the Boltzman constant, T is the temperature (K^o) and A is the ideality factor.

The four parameters of this model are: I_{Ph}, I_0, R_S, and A.

In this model, the effect of shunt resistance is not taking in account. Eq. (2) describes the I-V curve quite well, but the parameters cannot be measured in a simple manner. Therefore, a fit based on a smaller number of parameters which can be measured easily have been developed in [12], these include:

- The open circuit voltage V_{OC}.
- The short-circuit current I_{SC}.
- The maximum power P_m.

2.3 Solar cell model using five parameters

In this model, the effect of shunt resistance is considered [13]. Fig. 1 shows a solar cell equivalent circuit including series resistance R_S and shunt resistance R_{Sh}.

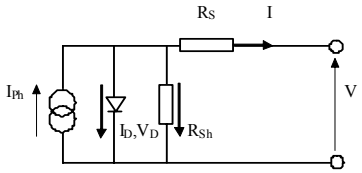

Figure 1. Solar cell equivalent circuit including series resistance and shunt resistance

The mathematical description of this circuit is given by the following equation:

$$I = I_{Ph} - I_0.\left[Exp\left(\frac{q}{A.K.T}(V + R_S.I)\right) - 1\right] - \frac{V + R_S.I}{R_{Sh}} \quad (3)$$

The five parameters of this model are: I_{Ph}, I_0, R_S, R_{Sh} and A. For a given temperature and solar irradiation, these parameters are determined by using the open-circuit voltage V_{OC}, the short-circuit current I_{SC}, the voltage V_m and the current I_m at the maximum power point and the slopes of curve near V_{OC} and I_{SC}.

Thus

$$\left(\frac{dV}{dI}\right)_{V=Voc} = -R_{SO} \quad (4)$$

$$\left(\frac{dV}{dI}\right)_{I=Isc} = -R_{Sh0} \quad (5)$$

The following equations are obtained:

$$A = \frac{V_m + I_m.R_{S0} - V_{OC}}{V_t\left[Ln\left(I_{SC} - \frac{V_m}{R_{Sh}} - I_m\right) - Ln\left(I_{SC} - \frac{V_{OC}}{R_{Sh}}\right) + \left(\frac{I_m}{I_{SC} - \frac{V_{OC}}{R_{Sh0}}}\right)\right]} \quad (6)$$

where

$$V_t = \frac{K.T}{q}$$

$$I_0 = \left(I_{SC} - \frac{V_{OC}}{R_{Sh}}\right).Exp\left(-\frac{V_{OC}}{A.V_t}\right) \quad (7)$$

$$R_S = R_{S0} - \frac{A.V_t}{I_0}.Exp\left(-\frac{V_{OC}}{A.V_t}\right) \quad (8)$$

$$I_{Ph} = I_{SC}.\left(1+\frac{R_S}{R_{Sh}}\right) + I_0.\left(Exp\left(\frac{I_{SC}.R_S}{A.V_t}\right)-1\right) \quad (9)$$

$$R_{Sh} = R_{Sh0} \quad (10)$$

2.4 Solar cell model using two exponential

The solar cell equivalent circuit including series resistance R_S, shunt resistance R_{Sh}, two exponential-type ideal junction, a constant photo-generated current source is shown in Fig. 2.

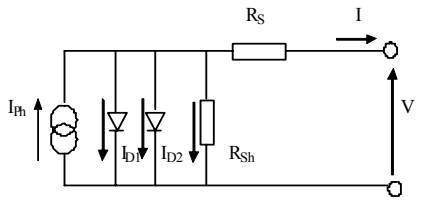

Figure 2. Solar cell equivalent circuit for model with two exponential

The mathematical description of this circuit is given by the following equation [14]:

$$I = I_{Ph} - I_{01}.\left[Exp\left(\frac{q}{A_1.K.T}(V+R_S.I)\right)-1\right] - I_{02}.\left[Exp\left(\frac{q}{A_2.K.T}(V+R_S.I)\right)-1\right] - \frac{V+R_S.I}{R_{Sh}} \quad (11)$$

The parameters of this model I_{Ph}, A_1, A_2, I_{01}, I_{02}, R_S and R_{Sh} are determined by the following approximations [14]:

$$I_{Ph} = I_{SC}$$

$$I_{01} = \frac{1}{2}.\frac{I_{Ph}}{\left(Exp\left(-\frac{e.V_{OC}}{K.T}\right)-1\right)} \quad (12)$$

$$I_{02} = \frac{1}{2}.\frac{I_{Ph}}{\left(Exp\left(-\frac{e.V_{OC}}{2.K.T}\right)-1\right)} \quad (13)$$

R_S is obtained by derivation of Eq. (11) at $V = V_{oc}$:

$$R_S = \left[\frac{dV}{dI}\Big|_{V=Voc} + \frac{1}{X_{1V}+X_{2V}+\frac{1}{R_{Sh}}}\right] \quad (14)$$

with

$$X_{1V} = -\frac{e.I_{01}}{K.T}.Exp\left(-\frac{e.V_{OC}}{K.T}\right) \quad (15)$$

$$X_{2V} = -\frac{e.I_{02}}{A.K.T}.Exp\left(-\frac{e.V_{OC}}{A.K.T}\right) \quad (16)$$

If we consider $\frac{1}{R_{Sh}} \ll (X_{1v}+X_{2v})$, we can obtain a simplified relation for R_S as:

$$R_S = -\left[\frac{dV}{dI}\Big|_{V=Voc} + \frac{1}{X_{1V}+X_{2V}}\right] \quad (17)$$

The shunt resistance R_{Sh} is deduced from Eq. (14) with $I = I_{SC}$

$$R_{Sh} = -\frac{1}{\left[\frac{1}{\left(\frac{dV}{dI}\Big|_{I=Isc}+R_S\right)}+X_{1i}+X_{2i}\right]} \quad (18)$$

where

$$X_{1i} = \frac{I_{01}}{V_t}Exp\left(\frac{I_{SC}.R_S}{V_t}\right) \quad (19)$$

$$X_{2i} = \frac{I_{02}}{A.V_t}Exp\left(\frac{I_{SC}.R_S}{A.V_t}\right) \quad (20)$$

3. COMPARISON WITH EXPERIMENTAL CHARACTERISTIC

3.1 Explicit model

Fig. 3 shows the I-V characteristic by using the explicit model, as can be seen this model gives a best representation of I-V curve. However, the limitation of this method is that it doesn't take in account the serial resistance R_S and the shunt resistance R_{Sh}.

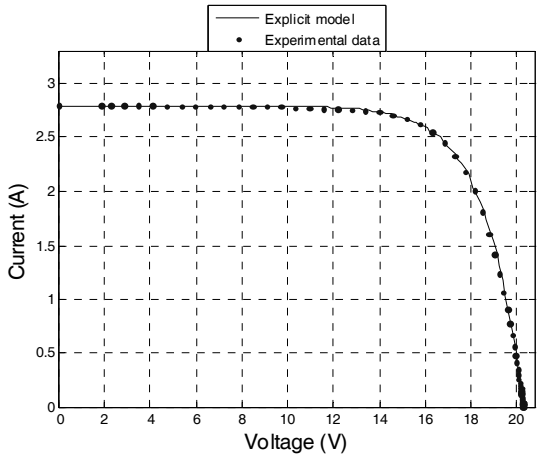

Figure 3. The I-V characterization using explicit model at 800 W/m^2 and 45^{o}C

3.2 Four parameters model

This method is based on single exponential model of solar cell and assumes that R_{Sh} is infinite, an assumption that may not be valid for the cell having low R_{Sh} values.

Fig. 4 shows the I-V curve given by this method. According to this figure, we can clearly observe that a difference between experimental I-V curve and those simulated in non-linear region near the maximum power point.

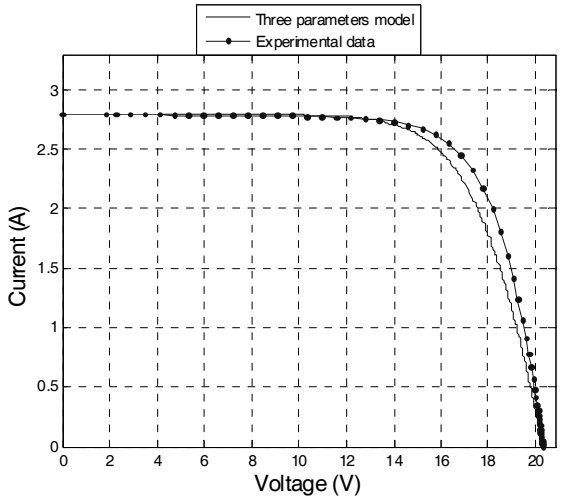

Figure 4. I-V characterization using three parameters model at 800 W/m^2 and 45^{o}C

3.3 Five parameters model

The I-V characterization of the five parameters model is shown in Fig. 5. The five parameters model is shown to give accurate reliable results but gives non-physical values at low illuminations [14]. In order to evaluate the accuracy of the models, a statistical tests was used [15], and root mean square error (RMSE). The RMSE is given as follow:

$$RMSE = \left(\frac{1}{n} \sum_{i=1}^{n} (I_{si} - I_{mi})^2 \right)^{1/2} \quad (21)$$

Where n is the number of data, I_{si} is the i^{th} simulated current and I_{mi} is the i^{th} measured current. The RMSE test provides information on the short-term performance of the simulation model. The lower value of RMSE means the more accuracy for the model used.

The RMSE values of the models were calculated. Table 1 shows the RMSE values obtained from the models presented. The RMSE average values, which are a measure of the accuracy of estimation, have been found to be the lowest for five parameters model (RMSE = 0.022) at illumination of 800 W/m^2. This means the good estimation of I-V characterization by using a five parameters model than the three parameters model and the explicit model for the illumination of 800 W/m^2.

Table 1. RMSE values for each model

Solar irradiation (Wh/m^2)	1000	800
Temperature (°C)	25	45
	RMSE	RMSE
Explicit model	0.039	0.027
Three parameters model	0.047	0.104
Five parameters model	0.095	0.022

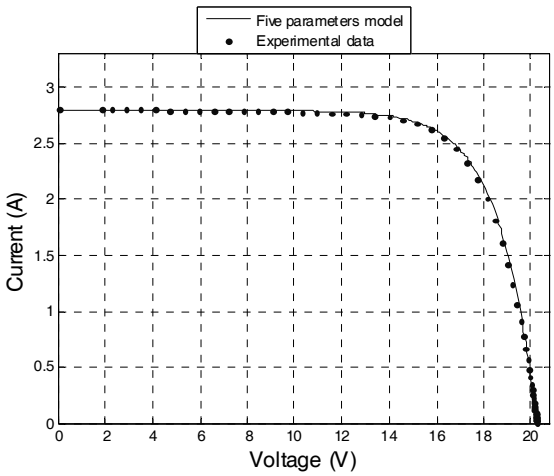

Figure 5. I-V characterization using five parameters model at 800 W/m^2 and 45^{o}C

4. THE PROPOSED EXPLICIT MODEL

Measurements of peak-power and internal series resistance under natural ambient conditions need mathematical corrections of the measured I-V characteristic, considering irradiance and cell temperature.

The purpose of I-V characteristic approximation by means of equivalent circuit diagrams lies in the explicit calculability of matching problems between solar generators and several loads. The equivalent circuit diagram for the effective solar cell characteristic is given by Fig. 6.

The effective solar cell characteristic is given by the following model:

$$I = I_{ph} - I_0\left(e^{\frac{V+R_{PV}.I}{V_T}} - 1\right) \tag{22}$$

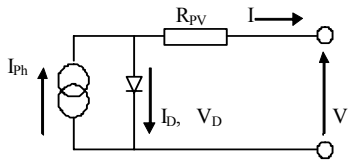

Figure 6. Equivalent circuit diagram for effective solar cell characteristic

The explicit version is:

$$V = V_T.Ln\left(\frac{I_{ph} - I + I_0}{I_0}\right) - R_{PV}.I \tag{23}$$

Where R_{PV} is the photovoltaic resistance, not to be confused with the serial resistance RS.

Therefore, we need to determine the following parameters: R_{PV}, V_T, I_0 and I_{Ph}. Based on the following the following simplification:

$$Exp\left(\frac{V + R_{PV}.I}{V_T}\right) \rangle\rangle 1 \text{ and } I_{Ph} = I_{SC}$$

The I-V curve can be expressed as:

$$I = I_{SC}\left[1 - \left(\frac{I_0}{I_{SC}}\right).Exp\left(\frac{V + R_{PV}.I}{V_T}\right)\right] \tag{24}$$

then

$$V = V_T.Ln\left(\frac{I_{CS} - I}{I_0}\right) - R_{PV}.I \tag{25}$$

Since I_0, V_T and R_{PV} are unknown, three conditions are required to enable use of this fit:

1. If $I = 0$, then $V = V_{OC}$.
2. At the maximum power point the fit is tangent to the hyperbola $P_m = V.I$
3. The slope S at the open circuit voltage is to be considered.

The condition (1) yields:

$$V_{OC} = V\big|_{I=0} = V_T.Ln\left(\frac{I_{SC}}{I_0}\right)$$

or

$$V_T = \frac{V_{OC}}{Ln\left(\frac{I_{SC}}{I_0}\right)} \tag{26}$$

and then

$$I_0 = I_{SC}.e^{-\frac{V_{OC}}{V_T}} \tag{27}$$

The condition (2) can be expressed as:

$$V\big|_{I=I_m} = \frac{P_m}{I_m} \tag{28}$$

$$\left.\frac{\partial V}{\partial I}\right|_{I=I_m} = \frac{\partial}{\partial I}\left(\frac{P_m}{I}\right)\Bigg| = -\frac{P_m}{I_m^2} \tag{29}$$

Differentiating Eq. (29) according to (25), we get:

$$\frac{\partial V}{\partial I} = -\frac{V_T}{\left(I_{Sc} - I\right)} - R_{PV}$$

For $I = I_m$, we get:

$$\left.\frac{\partial V}{\partial I}\right|_{I=I_m} = -\frac{V_T}{\left(I_{SC} - I_m\right)} - R_{PV} = -\frac{P_m}{I_m^2} \tag{30}$$

then

$$R_{PV} = \frac{V_m}{I_m} - \frac{V_T}{\left(I_{SC} - I_m\right)} \tag{31}$$

By substituting Eq. (26) in (31), we get:

$$R_{PV} = \frac{V_m}{I_m} - \frac{V_{OC}}{\left(I_{SC} - I_m\right).Ln\left(\frac{I_{SC}}{I_0}\right)} \tag{32}$$

It was found that a typical value of the ratio (I_0/I_{SC}) for a silicon cell at 25°C and 1000 W/m^2 ranges from approximately 10^{-7}-10^{-10}, see [12, 13]. So, in order to reduce the number of measurements, we may assume that $(I_0/I_{SC}) = 10^{-7}$, at least. Substituting this value into Eq. (24) and (26) yields:

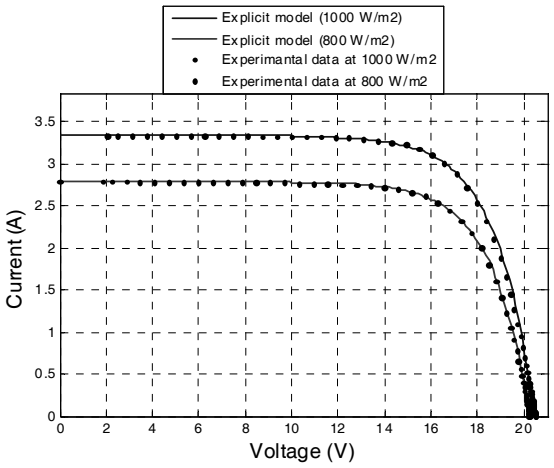

Figure 7. I-V curve for two illuminations (explicit model)

$$V_T = \frac{V_{OC}}{Ln10^7} = \frac{V_{OC}}{16.11}$$
$$I = I_{SC}\left[1 - 10^{-7}.Exp\frac{16.11}{V_{OC}}(V + R_{PV}.I)\right] \quad (33)$$

And then Eq. (33) yields:

$$V = \left[\frac{V_{OC}}{16.11}.Ln\frac{10^7(I_{SC} - I)}{I_{SC}}\right] - R_{PV}.I$$

Eq. (32) yields:

$$R_{PV} = \frac{V_m}{I_m} - \frac{V_{OC}}{16.11\left(I_{SC} - I_m\right)} \quad (34)$$

The condition (3) yields:

$$S = \left.\frac{dV}{dI}\right|_{I=0} = -\frac{V_T}{\left(I_{Sc}\right)} - R_{PV}$$

then

$$V_T = -\left(S + R_{PV}\right).I_{SC} \quad (35)$$

Substituting Eq. (35) into (31), we get:

$$R_{PV} = \frac{V_m}{I_m} + \frac{\left(S + R_{PV}\right).I_{SC}}{\left(I_{SC} - I_m\right)}$$

then

$$R_{pv} = -S\frac{I_{sc}}{I_m} + \frac{Vm}{I_m}\left(1 - \frac{I_{sc}}{I_m}\right) \quad (36)$$

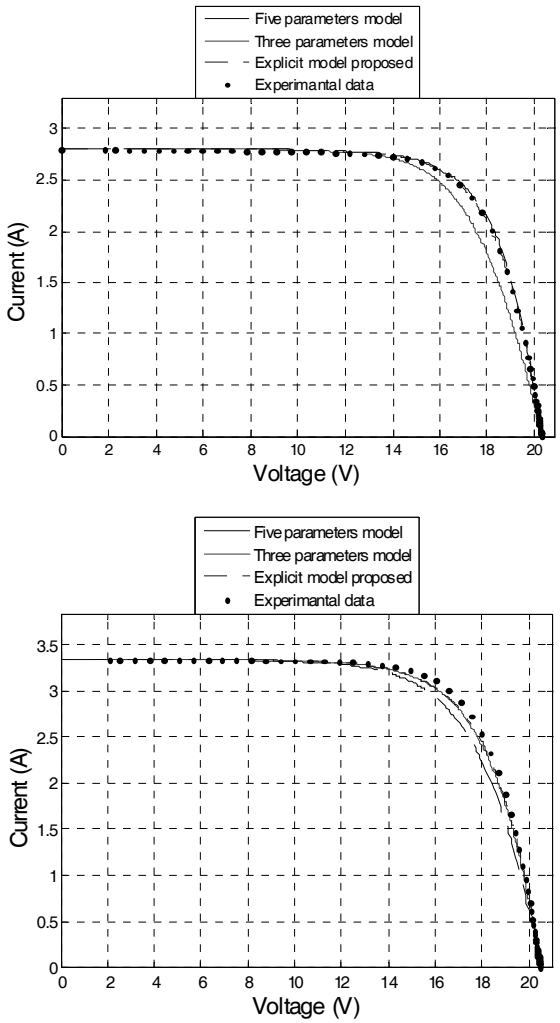

Figure 8. a) Simulation and experimental I-V curve (illumination 800 W/m^2); b) Simulation and experimental I-V curve (illumination 1000 W/m^2)

The slope *S* is then given by the approximate function [15]:

$$S = \frac{V_{OC}}{I_{SC}}\left(\alpha_1.\frac{I_{p\max}.V_{p\max}}{I_{SC}.V_{OC}} + \alpha_2.\frac{V_{p\max}}{V_{OC}} + \alpha_3.\frac{I_{p\max}}{I_{SC}} + \alpha_4\right)$$

With the equation-constants:

$$\alpha = \begin{pmatrix} -5.411 \\ 6.450 \\ 3.417 \\ -4.422 \end{pmatrix}$$

We note that Eq. (36) is independent of material properties of the solar cell.

The R_{PV} is calculated using Eq. (34) for silicon cell or using Eq. (36) for any material properties of the solar cell. The value of R_{PV} is substituted into Eq. (22) to find the I-V curve of a single solar cell.

Fig. 7 shows a good agreement between experimental I-V curve and those given by the proposed explicit model for different illuminations.

Fig. 8 (a) and (b) show a comparison between the I-V curve estimated by the proposed explicit model, other model presented in the present study and the experimental data.

In order to show the accuracy of the proposed model, we have calculate the RMSE values, it should be noted that the obtained RMSE for the proposed explicit model is 0.01 for illumination of 800 W/m^2, and 0.03 for the illumination of 1000 W/m^2, which are very satisfactory.

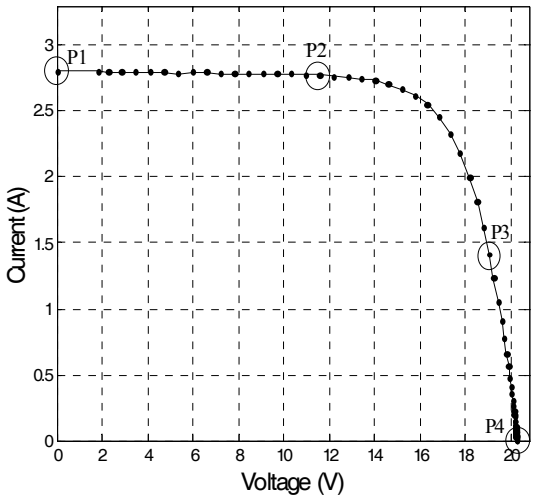

Figure 9. Experimental working points

5. NEW EXPERIMENTAL METHOD FOR CALCULATION OF R_S AND R_{SH}

The shunt resistance R_{Sh} is calculated near the two points P_1 and P_2 on the illuminated I-V characteristic. P_1 is near the short-circuit point and thus corresponds to a low value of voltage. P_2 is near the maximum power point and therefore corresponds to a higher voltage.

The series resistance R_S is calculated near the two points P_3 and P_4 on the illuminated I-V characteristic. P_4 is near the open-circuit point ($V = V_{OC}$) and P_3 is near the maximum power point.

The choice of the four working points P_1, P_2, P_3 and P_4 is deduced after several iteration using the algorithm given below, and the optimal choice is given by, see Fig. 9:

$I_1 = I_{SC}$ (V = 0 V) for the point P_1.

I_2= 95% of ISC for the point P_2.

I_3 = 50% of ISC for the point P_3.

I_4 = 0 (V = V_{OC}) for the point P_4.

Determination of the working points V_1, V_2, V_3 and V_4 with Eq. (23).

$V_i = V(I_i)$, $\quad i$ = 1 to 4.

Algorithm

$V_4 = V_{OC}$, I_4 = 0;

V_m, I_m, I_{SC} and RSM are fixed;

I_3 varies from 0 to I_{SC};

From each value of I_3, we get V_3 (Eq. (23)) and then we calculate R_S using the relation:

$$R_S = \frac{V_4 - V_3}{I_3 - I_4} \tag{37}$$

If the calculated value of R_S is not equal to RSM, we increase the value of I_3 until the value of R_S reaches the measured value RSM. We have find that I_3 is equal to 50% of I_{SC}.

The shunt resistance R_{Sh} is given by the relation:

$$R_{Sh} = \frac{V_2 - V_1}{I_1 - I_2} \tag{38}$$

The following examples show the accuracy of this method.

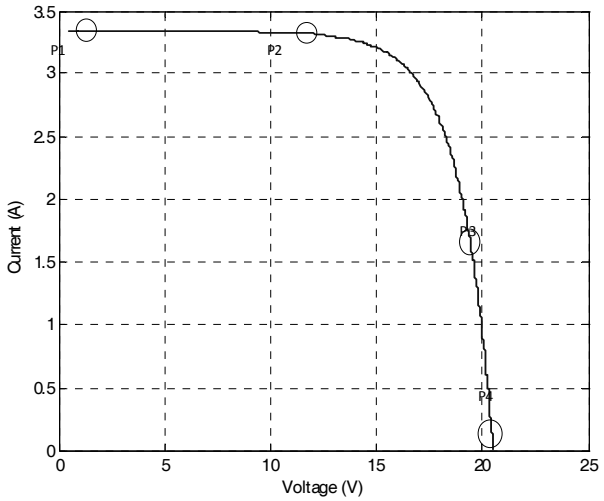

Figure 10. I-V characteristic for the PV-module BP585F

Example 1: Monocrystalline PV-Module Isophoton

V_{OC} =20.51 V

V_m =16.58 V

I_m = 3.01 A

I_{sc} = 3.34 A

Fig. 10 shows the I-V characteristic of the PV-module Isophoton. We have found R_S = 0.64Ω and R_{Sh} = 89.42Ω.

Example 2: Monocrystalline PV-Module BP585F

V_{OC} = 22.3 V

V_m = 18 V

I_m = 4.72 A

I_{sc} = 5 A

We have found: R_S = 0.50Ω and R_{Sh} = 77.75Ω

Fig. 11 shows the I-V characteristic for experimental manipulation of the PV-Module BP585F.

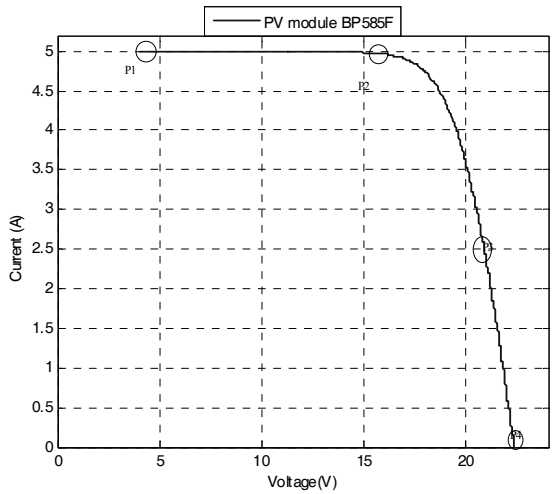

Figure 11. Experimental working points for Monocrystalline PV-Module Isophoton

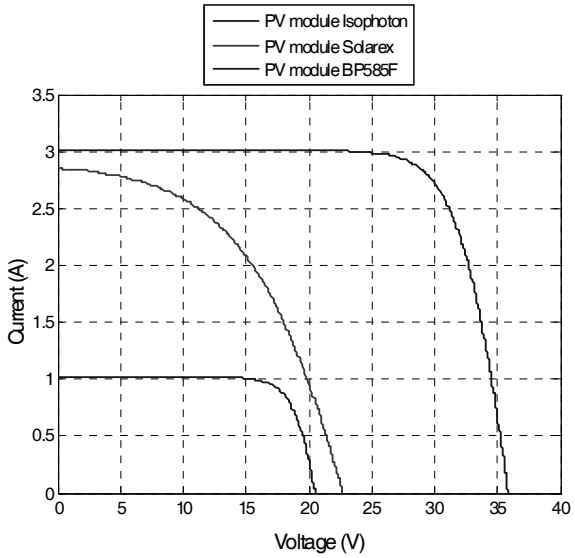

Figure 12. I-V characterization for different modules using the proposed explicit model

Example 3: I-V curve approximation

The I-V curve for some modules by using the proposed explicit model is shown in Fig. 12.

The values of series and shunt resistance are given in Table 2. According to this table, we note that for the same illumination, the series resistance of the PV module BP585F is the lowest while the highest value of shunt resistance is given by the PV module Isophoton.

Table 2. Values of series and shunt resistances for different PV modules

PV modules	Isophoton	BP585F	MSX 40
R_S (Ω)	0.64	0.50	3.06
R_{Sh} (Ω)	89.42	77.75	63.83

6. CONCLUSIONS

A new explicit model for I-V characteristic of photovoltaic module has been described. It has been demonstrated that the proposed model estimate the parameters value of the I-V curve with a good accuracy. Also, the experimental method for determining of serial resistance R_S and shunt resistance R_{Sh} is more convenient. A theoretical expression given in Eq. (36) gives the photovoltaic resistance R_{PV} for any materials properties of the solar cell, and if we use the silicon cell the photovoltaic resistance is given by Eq. (34). The value of R_{PV} is substituted into Eq. (22) to find the I-V curve of a single solar cell or PV module.

ACKNOWLEDGEMENT

The authors gratefully acknowledge the Deanship of Scientific Research Taibah University who financially supported this work, under contracted research project 33/427.

REFERENCES

[1] M. A. Green, “Photovoltaics: technology overview”, Energy Policy, Vol. 28,2000, pp. 989-998.

[2] D. S. H. Chan, J. R. Phillips, J. C. H. Phang, “A comparative study of extraction methods for solar cell model parameters”, Solid-state Electronics, Vol. 29, No. 3, 1986, pp. 329-337.

[3] M. Haouari-Merbah, M. Belhamel, I. Tobias, J. M. Ruiz, “Extraction and analysis of solar cell parameters from illuminated current-voltage curve”, Solar Energy Materials and Solar Cells, Vol. 87, 2005, pp. 225-233.

[4] A. Garrigos, J. M. Blanes, J. A. Carrasco, J. B. Ejea, “Real time estimation of photovoltaic modules characteristics and its application to maximum power point operation”, Renewable Energy, Vol. 32, 2007, pp. 1059-1076.

[5] G. Blaesser, D. Munro, “Guidelines for the assessment of photovoltaic plants”, Document C. Issue 2. Report EUR 16340 EN, Commission of the European Communities, Joint Research Centre of Ispra, 1995.

[6] M. A. Green, “Solar cells: operating principles, technology and system applications”, New Jersey: Prentice-Hall, 1982, ISBN: 9780138222703.

[7] C. R. Osterwald, “Translation of device performance measurement to reference conditions“, Solar cells Vol. 18, 1986, pp. 269-79.

[8] B. Marion, "A method for modelling the current-voltage curve on a PV module for outdoor conditions", Progress in Photovoltaics: Research and Applications 2002, Vol. 10, pp. 205-214.

[9] B. Marion, S. Rummel, A. Anderberg, "Current-voltage curve translation by bilinear interpolation", Progress in Photovoltaics: Research and Applications, Vol. 12, 2004, pp. 593-607.

[10] M. Wolf, H. Rauschenbach, "Series Resistance Effects on Solar Cell Measurements", Advanced Energy Conversion, Vol. 3, 1963, pp. 455-479.

[11] G. W. Hart," Residential photovoltaic system simulation electrical aspect", IEEE, 1982, pp. 281-288.

[12] S. Singer, B. Rozenshtein, S. Saurazi, "Characterization of PV array output using a small number of measured parameters", Solar Energy, Vol. 32, No. 5, 1984, pp. 603-607.

[13] Y. Hishikawa, Y. Imura, T. Oshiro, "Irradiance-dependence and translation of the I-V characteristics of crystalline silicon solar cells", 28th IEEE PV Specialist Conference, Anchorage, AK, 2000, pp. 1464-1467.

[14] J. A. Gow, C. D. Manning, "Development of a photovoltaic array model for use in power-electronics simulation studies", Proc. IEEE Elect. Power Appl., Vol. 146, No. 2, 1999, pp. 193-200.

[15] C. Bendel, A.Wagner, "Photovoltaic measurement relevant to the energy yield", WCPEC-3, World Conference on Photovoltaic Energy Conversion, Osaka, Japan, 2003, No. 7P-B3-09, pp. 1-4.

Biographies

Mohamed Benghanem is an Associate Professor at Taibah University, Faculty of Sciences, Madinah, Saudi Arabia. He his Regular associate at International Centre of Theoretical Physics, ICTP, Italy since 2004. He obtained his BE, MSc and Ph.D. in Electrical Engineering from Polytechnic School and USTHB University, Algiers, respectively. His research interests are Solar instrumentations, data acquisition systems, and renewable energy systems.

Saleh N. Alamri is an Associate Professor of Applied Physics in the Physics Department, Faculty of Sciences, Taibah University, Madinah, Saudi Arabia. He holds a Ph.D. degree in thin film Cds/CdTe Solar Cells from Durham University, England (1999). His research interests are Thin films deposition and characterization.

Adel Mellit was born in Algiers, Algeria on July 21, 1974. He received his B. Elect. Eng. (Hons) from University of Blida in 1997 and MSc in Electronics option Renewable Energy from University of Sciences Technologies Algiers in 2002, and Ph.D. in Electronics option Renewable Energy from University of Sciences Technologies (USTHB) Algiers in 2006. His research interest includes the application of the artificial intelligence techniques in photovoltaic power supply systems, meteorological data modeling, and weather forecasting. He has authored and co-authored more then 45 technical papers in international journals and conferences, Also he is serving as a reviewer for different journals and conferences. To date, he has received more than 50 citations of his work. He is also junior associate member at the International Center for Theoretical Physics (ICTP) Italy. Currently he is assistant professor at Jijel University, Department of Electronics/LMD.

PID CONTROLLER DESIGN FOR TIME DELAY SYSTEMS USING GENETIC ALGORITHMS

K. Saadaoui *, A. Moussa, M. Benrejeb
U.R. LA.R.A Automatique, Ecole Nationale d'Ingenieurs de Tunis, Tunisia

ABSTRACT

In this paper, stabilizing regions of a PID controller applied to a class of time delay systems are computed using parametric methods. A necessary condition is used to obtain the admissible ranges of proportional and derivative gains. Then, for a fixed value of one of these parameters within this admissible range, stabilizing regions in the space of the remaining two parameters are determined. Stabilization being the most basic requirement in any controller design problem, once this property is guaranteed we can search among these stabilizing controllers those that satisfy other performance specifications. This step is carried out using the genetic algorithm optimization method. Time domain measures of the closed loop system such as maximum percent overshoot, rise time and settling time are minimized using genetic algorithms and the stabilizing regions of the PID controller values. Examples are given to demonstrate the effectiveness of our proposed approach.

Keywords

Stability, Time Delay Systems, PID Controller, Genetic Algorithms.

1. INTRODUCTION

Many industrial systems are represented by plants with time delay. For this reason, stabilization and control of time delay systems continue to be active areas of research [1]. Recently, there has been a great interest in computing stabilizing regions in the parameter space of simple controllers, such as PID or first order controllers. The main motivation for considering such controllers comes from the desire to reduce controller complexity and to determine as low order a controller as possible for a given high order or complex plant [2, 3].

Several computational methods have been proposed to find the set of all stabilizing first order and PID controllers for delay free linear time invariant systems [2-4]. Computing the set of all stabilizing PID controllers for special classes of time delay systems was also addressed. Using a generalization of the Hermite-Biehler theorem the set of all stabilizing PI and PID controllers are determined for first order systems with dead time in [5] and [6], respectively. We refer the reader to [7] for a detailed explanation of theses methods. In [8] a graphical method was used to determine all stabilizing parameters of a PID controller applied to second order plants with dead time. In [9], the same problem is addressed for n^{th}-order all pole plants, that are systems with a pole of multiplicity n, with dead time.

This paper is an extension of the results in [5-9] to all poles plants with dead time. The new method used is characterized by the application of a necessary condition to get admissible ranges of one of the controllers' parameters. The necessary condition is a consequence of a lemma given in [10]. The D-decomposition method [11, 12] is then applied to find stabilizing regions in the parameter space of the remaining two parameters. By sweeping over the admissible ranges of the first parameter, the complete set of stabilizing PID controllers for this class of systems is obtained.

Stabilization being the most basic requirement in most controller design problems, determining the set of all stabilizing controllers of a given order is a first step in searching, among such controllers, those that satisfy further performance criteria, such as those imposed on the unit step response of the closed loop system. Once this first step is done, genetic algorithms are used to minimize several performance measures of the closed loop system. Genetic algorithms (GAs) [13-18] are stochastic optimization methods. Unlike classical optimization methods, they are not gradient based which makes GAs suitable to minimize performance measures such as maximum percent overshoot, rise time, settling time and integral square error. Moreover, genetic algorithms explore the entire admissible space to search the optimal solution. This is another reason for using GAs after finding the complete set of stabilizing PID controllers which form the set of admissible solutions. In this work, the ranges of proportional derivative and integral gains are not set arbitrary but they are set within the stabilizing regions determined so that we are searching among the stabilizing values of the PID controller.

The paper is organized as follows. In Section 2, the D-decomposition method is introduced and a necessary condition is used to compute the admissible ranges of proportional and derivative gains. In Section 3, the stabilizing regions in the space of the controller's parameters are determined. Next, the genetic algorithm method is used to minimize several performance measures of the step response of the closed loop system. In Section 4, two examples are given. Finally, Section 5 contains some concluding remarks.

2. RANGES OF PROPORTIONAL AND DERIVATIVE GAINS

In this paper, we consider determining the stabilizing regions in the parameter space of a PID controller.

*Corresponding author: *E-mail:* karim.saadaoui@isa2m.rnu.tn

 ISSN: 1743-9310

$$C(s) = \frac{k_d s^2 + k_p s + k_i}{s} \tag{1}$$

Applied to an n^{th} order all poles system with delay,

$$G(s) = \frac{e^{-Ls}}{Q(s)} = \frac{e^{-Ls}}{q_n s^n + \cdots + q_0} \tag{2}$$

where $L > 0$ is the time delay. In this section, the admissible ranges of the parameters (k_p, k_d) are found, where k_p is the proportional gain and k_d is the derivative gain. The exact range of stabilizing (k_p, k_d) values is difficult to determine analytically. In fact, the problem of determining the exact range of stabilizing k_p values analytically is solved for the case of a first order plant with dead time [6]. Therefore, instead of determining the exact range of k_p (or k_d), a necessary condition will be used to get an estimate of the stabilizing range.

Let us first fix the notation used in this paper. Let $\mathbb{R}$ denote the set of real numbers and $\mathbb{C}$ denote the set of complex numbers and let $\mathbb{C}_-$, $\mathbb{C}_0$, $\mathbb{C}_+$ denote the points in the open left-half, $j\omega$-axis, and the open right-half of the complex plane, respectively. The derivative of a polynomial or a quasi-polynomial Ψ is denoted by Ψ'. The set H of stable quasi-polynomials are,

$$\mathrm{H} = \left\{ \Psi(s) \in \mathbb{R}[s] : \Psi(s) = 0 \Rightarrow s \in \mathbb{C}_- \right\}$$

The following result will be used in determining the admissible values of k_p (alternatively k_d).

Lemma 1: [10] *Consider the quasi-polynomial*,

$$\Psi(s) = \sum_{i=0}^{n} \sum_{l=1}^{r} h_{il} s^{n-i} e^{\tau_l s}$$

such that $\tau_1 < \tau_2 < \ldots < \tau_r$, *with main term* $h_{0r} \neq 0$, *and* $\tau_1 + \tau_r > 0$. *If* $\Psi(s)$ *is stable, then* $\Psi'(s)$ *is also a stable quasi-polynomial.*

The characteristic function of the closed loop system formed by the PID controller and the time delay system (2) is given by,

$$\Psi_1(s) = sQ(s) + (k_d s^2 + k_p s + k_i) e^{-Ls} \tag{3}$$

Since the term e^{-Ls} has no finite roots, the quasi-polynomial $\Psi_1(s)$ and $\Psi(s) = \Psi_1(s)e^{Ls}$ have the same roots, therefore stability of $\Psi(s)$ is equivalent to stability of $\Psi_1(s)$, see [10]. In the sequel, the quasi-polynomial,

$$\Psi(s) = sQ(s)e^{Ls} + (k_d s^2 + k_p s + k_i) \tag{4}$$

will be used to study stability of the closed loop system. Now, using **Lemma 1**, if $\Psi(s)$ is stable then $\Psi'(s)$ is also a stable quasi-polynomial, where $\Psi'(s)$ is given by,

$$\Psi'(s) = \left((Ls+1)Q(s) + sQ'(s) \right) e^{Ls} + 2k_d s + k_p \tag{5}$$

Note that only two parameters (k_p, k_d) appear in the expression of $\Psi'(s)$. By **Lemma 1**, stabilizing $\Psi'(s)$ is equivalent to calculating the admissible (k_p, k_d) values for the original problem.

The D-decomposition method [11, 12] is used to determine the stabilizing regions in the (k_p, k_d) plane. The D-decomposition method is based on the fact that roots of the quasi-polynomial (5) change continuously when the coefficients are changed continuously. Hence, a stable quasi-polynomial can become unstable if and only if at least one of its roots crosses the imaginary axis. Using this fact, the (k_p, k_d) plane can be partitioned into regions having the same number of roots of (5) in the left half plane. Stability can be checked by choosing a point inside a region and applying classical methods such as the Nyquist criterion.

Evaluating the characteristic function at the imaginary axis is equivalent to replacing s by $j\omega$, $\omega \geq 0$ in (5), we get:

$$\begin{aligned} \Psi'(j\omega) = & \left(R(\omega) - L\omega I(\omega) - \omega I'(\omega) \right) \cos(L\omega) \\ & - \left(\omega L R(\omega) + \omega R'(\omega) \right) \sin(L\omega) + k_p \\ & + j \left[\left(R(\omega) - L\omega I(\omega) - \omega I'(\omega) \right) \sin(L\omega) \right. \\ & \left. + (\omega L R(\omega) + \omega R'(\omega)) \cos(L\omega) + 2\omega k_d \right] \end{aligned} \tag{6}$$

where

$$Q(j\omega) = R(\omega) + jI(\omega) \tag{7}$$

and

$$Q'(j\omega) = R'(\omega) + jI'(\omega) \tag{8}$$

Applying the D-decomposition method implies equating the real and imaginary parts of (6) to zero. Two cases must be considered:

- **Case 1:** $\omega = 0$ which leads to the following equation,

$$k_p = -Q(0) \tag{9}$$

- **Case 2:** $\omega > 0$ in this case we get,

$$\begin{aligned} k_p = & -\left(R(\omega) - L\omega I(\omega) - \omega I'(\omega) \right) \cos(L\omega) \\ & + \left(\omega L R(\omega) + \omega R'(\omega) \right) \sin(L\omega) \end{aligned} \tag{10}$$

$$\begin{aligned} k_d = & \left[\left(R(\omega) - L\omega I(\omega) - \omega I'(\omega) \right) \sin(L\omega) \right. \\ & \left. + (\omega L R(\omega) + \omega R'(\omega)) \cos(L\omega) \right] (2\omega)^{-1} \end{aligned} \tag{11}$$

By sweeping over values of $\omega > 0$, the (k_p, k_d) plane can be partitioned into root invariant regions. Using (9), (10) and (11) stabilizing regions in the plane can de determined.

3. PID CONTROLLER DESIGN

In this section, first the set of all stabilizing PID controllers are determined, this forms the set of admissible solutions for optimization. Next, GAs are used to optimize these PID parameters.

3.1 Stabilizing Regions

The admissible (k_p, k_d) values are calculated in Section 2. Now, we go back to the original problem by considering (4). Our method consists of fixing one parameter k_p or k_d and determining the stabilizing regions in the plane of the remaining two parameters. By sweeping over the admissible values of the first parameter (k_p or k_d), the complete set of the stabilizing regions is found. Once again the D-decomposition method is used. For $\omega = 0$, we get the following equation,

$$k_i = 0 \tag{12}$$

For $\omega > 0$ two cases will be investigated. First, let us fix k_p and find the stabilizing regions in the (k_d, k_i) plane. Using (4), replacing s by $j\omega$ and equating the real and imaginary parts to zero we get,

$$\begin{bmatrix} \cos(L\omega) & -\omega^2\cos(L\omega) \\ \sin(L\omega) & -\omega^2\sin(L\omega) \end{bmatrix} \begin{bmatrix} k_i \\ k_d \end{bmatrix} = \begin{bmatrix} k_p\omega\sin(L\omega) + \omega I(\omega) \\ -k_p\omega\cos(L\omega) + \omega R(\omega) \end{bmatrix} \tag{13}$$

Note that the matrix at the left-hand of (13) is singular. The singular frequencies [11] are determined as the solutions of Eq. (14),

$$k_p + I(\omega)\sin(L\omega) - R(\omega)\cos(L\omega) = 0 \tag{14}$$

and are denoted by ω_i, $i = 1, 2$. For each singular frequency ω_i, an equation of a straight line in the (k_d, k_i) plane is defined by:

$$k_i = \omega_i^2 k_d + \omega_i R(\omega_i)\sin(L\omega_i) + \omega_i I(\omega_i)\cos(L\omega_i) \tag{15}$$

which partition the plane into root-invariant regions among which the stabilizing regions, if any, have to be determined. Alternatively, one may fix k_d first and repeat the above procedure. In this case we have,

$$\begin{bmatrix} \cos(L\omega) & -\omega\sin(L\omega) \\ \sin(L\omega) & \omega\cos(L\omega) \end{bmatrix} \begin{bmatrix} k_i \\ k_p \end{bmatrix} = \begin{bmatrix} k_d\omega^2\cos(L\omega) + \omega I(\omega) \\ k_d\omega^2\sin(L\omega) - \omega R(\omega) \end{bmatrix} \tag{16}$$

solving this system we get,

$$k_i(\omega) = \omega^2 k_d + \omega I(\omega)\cos(L\omega) - \omega R(\omega)\sin(L\omega) \tag{17}$$

$$k_p(\omega) = -I(\omega)\sin(L\omega) - R(\omega)\cos(L\omega) \tag{18}$$

For $\omega > 0$ the above two equations partition the (k_p, k_i) plane into root-invariant regions. Hence stabilizing regions, if any, can be found. It is interesting to note here that depending on which parameter we fix first, either k_p or k_d, the obtained stabilizing region is different. This can be explained by the fact that in the first case the matrix is always singular and in the second case it is always non-singular.

3.2 PID Controller Design Using GAs

Determining the total set of stabilizing PID controllers is a first step in the design process. Once this set of stabilizing PID controllers is found, it is natural to search within this set, controllers that meet extra performance specifications. Four performance measures will be considered:

- Maximum percent overshoot (OS).
- Settling time (ST).
- Rise time (RT).
- Integral square error (ISE), $ISE = \int_0^{t_f} |e(t)|^2 dt$ where $e(t)$ is the error at time t.

Optimization is done using genetic algorithms. The first step in this design procedure, which consists of determining the total set of stabilizing PID controllers, is very important. It enhances the application of the genetic algorithm by fixing the search space, unlike other works on optimizing PID controllers using GAs [16-18] where the ranges of (k_p, k_i, k_d) are set arbitrary. Moreover, it improves the optimization time and increases the chances of obtaining the global optimum. Optimization of the PID controllers is done by minimizing each of the four cost functions: maximum percent overshoot, settling time, rise time and integral square error. GAs tries to find the global optimum by evaluating many points of the solution space in each generation. There are mainly three operations: reproduction, crossover and mutation, used to form new generations until a termination condition is reached [13-15]. In what follows, we briefly describe the parameters and tools used in the implementation of the genetic algorithm:

1. Since stability is an essential property for any control system, the search space consists of the stabilizing values of the PID controller which are determined in Section 3.1. Population size is chosen to be 150 individuals per population. In the beginning the initial population is randomly chosen within the stabilizing values of the PID controller. These individuals are candidate solutions to the problem. The number of generations is chosen as 100.
2. Evaluation of a generation is done by calculating the cost function for each individual. Since minimization problems are considered, the fitness function will be the inverse of the cost function.
3. Genetic operators: reproduction, crossover and mutation are used to form new generations. Individuals are chosen for reproduction according to their fitness value. Fittest ones have larger probability of selection. The Roulette Wheel selection method is used.
4. In order to improve next generations, crossover which is a process of combining parts of the parent individuals to produce new offsprings is done. Crossover value used is 0.8.
5. To avoid local minimum and explore new parts of the search space, mutation process is applied. It consists of randomly modifying individuals in the generation. Mutation probability is always set to a small value so that the search algorithm is not turned to a random search algorithm. The value chosen in our case is 0.01.
6. Steps 2-5 are repeated until a termination condition is reached. The maximum generation termination condition is adopted.

4. ILLUSTRATIVE EXAMPLES

In this section two illustrative examples are given.

4.1 Example 1

Consider stabilizing the second order integrating system,

$$G(s) = \frac{11.32}{s^2 + 11.32s} e^{-s} \tag{19}$$

by a PID controller. This transfer function represents a system composed of master-slave parts. The slave part is a model of a mobile robot which can move in one direction [19]. This robot is controlled through a communication network which introduces delays in the control loop. See [19] for more details about this system. First, the admissible values of (k_p, k_d) are calculated, see Fig. 1.

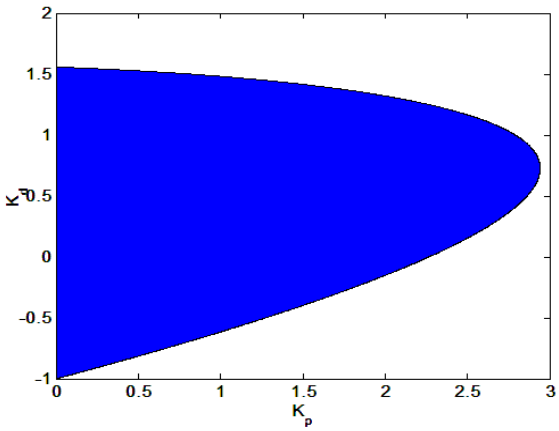

Figure 1. Admissible values of (k_p, k_d)

The first approach proposed, consists of fixing k_p and using (12), (14) and (15) to determine stabilizing regions in the plane of the remaining two parameters. By sweeping over the admissible values of k_p, the complete stabilizing regions of (k_p, k_i, k_d) values are found as shown in Fig. 2.

Alternatively, we can fix k_d and use (12), (17) and (18) to find the stabilizing regions of (k_p, k_i, k_d) values as shown in Fig. 3.

Fixing $k_d = 0$ is equivalent to using a PI controller. For $k_d = 0$, we obtain the stabilizing region of (k_p, k_i) values as given in Fig. 4.

Using this stabilizing region of (k_p, k_i) values and applying the genetic algorithm described in Section 3.2, to minimize each of the performance indices: maximum percent overshoot (Opt1), settling time (Opt2), rise time (Opt3) and integral square error (Opt4). We obtain the step responses of the closed loop system as shown in Fig. 5.

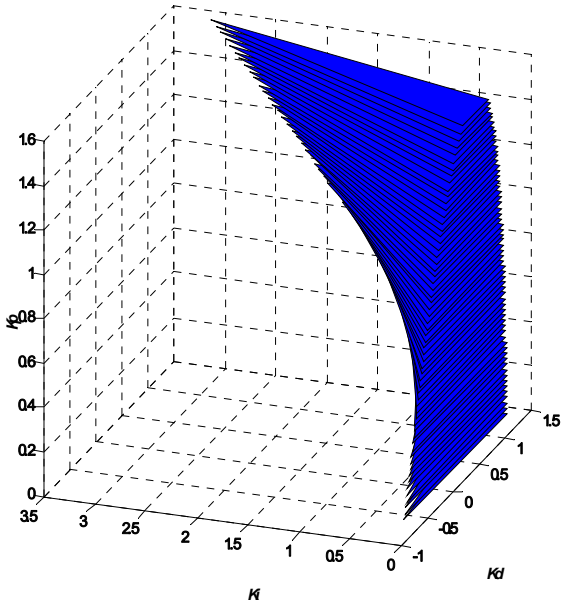

Figure 2. Complete set of stabilizing PID controllers for Example 1

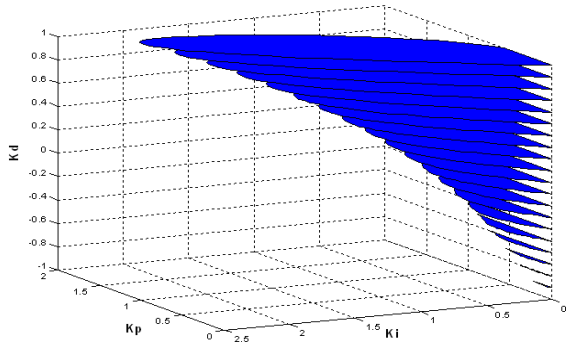

Figure 3. Complete set of stabilizing PID controllers for Example 1

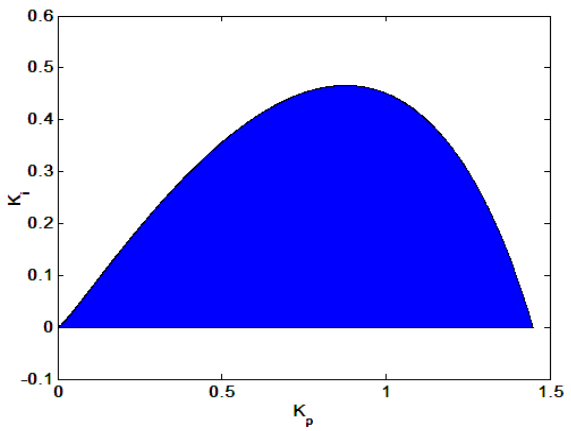

Figure 4. Complete set of stabilizing PI controllers for Example 1

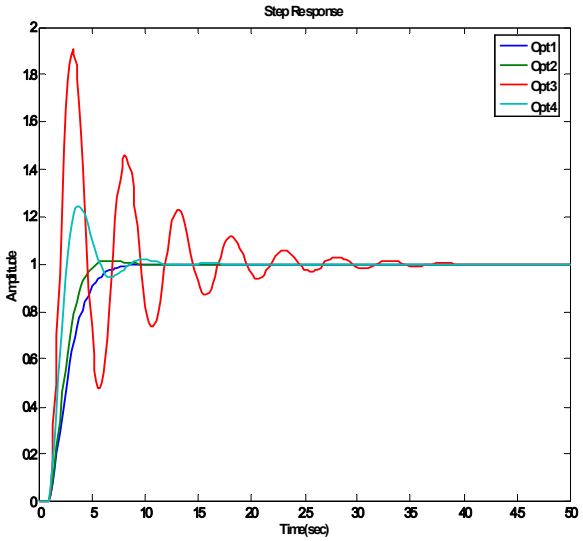

Figure 5. Step responses of the closed loop system

4.2 Example 2

Consider stabilizing the first order system given in [7],

$$G(s) = \frac{1}{3s+1} e^{-2.8s} \tag{20}$$

by a PID controller. For comparison reasons, we apply three classical methods. These methods are: Ziegler-Nichols method (ZN), Chien Hornes & Reswich method (CHR) and finally Cohen-Coon method (CC). After obtaining the stabilizing regions of (k_p, k_i, k_d) values, we apply the genetic algorithm to minimize the four performance indices described in section 3.2. Step responses of the closed loop system obtained with classical methods are given in Fig. 6.

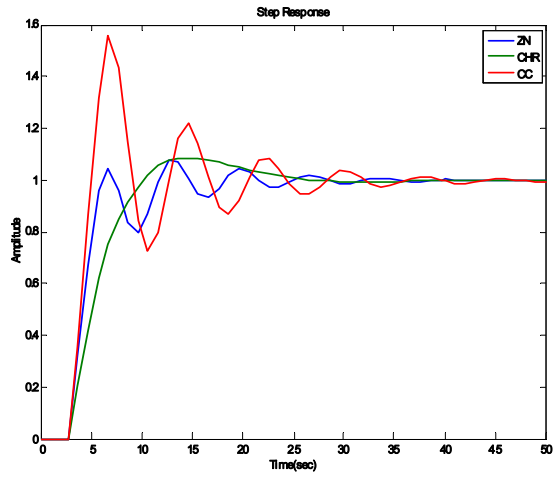

Figure 6. Step responses of the closed loop system for Example 2

Determining the set of stabilizing controllers and using GAs to optimize these stabilizing values, gives the step responses shown in Fig. 7.

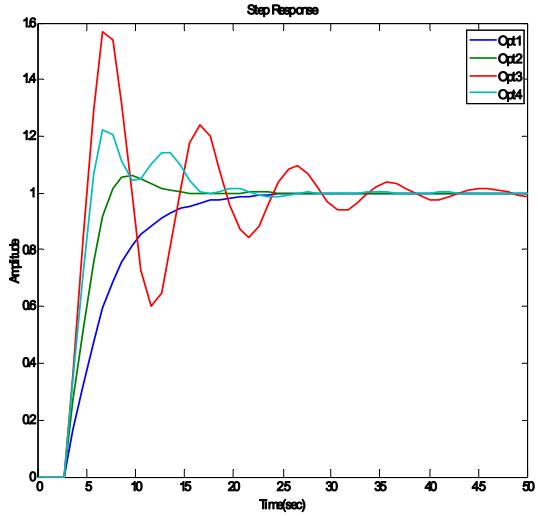

Figure 7. Step responses of the closed loop system for Example 2

Table 1. Results obtained by different methods

Method	(k_p,k_i,k_d)	OS (%)	ST (sec)	RT (sec)	ISE
ZN	(1.28, 0.22, 1.8)	7.9	24.9	5.9	3.17
CHR	(0.64, 0.21, 0.9)	9.1	24	8	3.75
CC	(1.69, 0.39, 1.49)	51	32.9	5.8	3.33
Opt 1	(0.52, 0.14, 0.28)	0	19	9	4.77
Opt 2	(0.84, 0.22, 0.39)	4.9	13	7	3.73
Opt 3	(1.69, 0.35, 0.55)	58	48	6	4.32
Opt 4	(1.22, 0.35, 1.67)	21.7	21.9	5.9	2.95

As can be seen from the results in Table 1, our method which consists of determining the total set of stabilizing PID parameters first and then applying genetic algorithms to minimize certain measures of the step response of the closed loop systems, gives better results when compared to classical empirical methods

5. CONCLUSIONS

In this paper, a new method is given for calculating all stabilizing values of a PID controller which is applied to a special class of time delay systems. The proposed approach is based on the application of the D-decomposition method. The genetic algorithm optimization method is then applied to find among those stabilizing controllers those that satisfy further performance specifications. Four time domain measures, which are maximum percent overshoot, settling time, rise time and integral square error, were minimized. Application of the proposed method to uncertain time delay system is under investigation.

REFERENCES

[1] Q. C. Zhong, "Robust control of time delay systems", Springer-Verlag, 2006, ISBN: 1846282640.

[2] K. Saadaoui, A. B. Ozguler, "A new method for the computation of all stabilizing controllers of a given order", International Journal of Control, Vol. 78, No. 1, 2005, pp. 14-28.

[3] A. Datta, M. T. Ho, S. P. Bhattacharyya, "Structure and synthesis of PID controllers", Springer-Verlag, 2000, ISBN: 1852336145.

[4] K. Saadaoui, A. B. Ozguler, "On the set of all stabilizing first order controllers", Proc. American Control Conference, Denver, CO, USA, 2003, pp. 5064-5065.

[5] G. J. Silva, A. Datta, S. P. Bhattacharyya, "PI stabilization of first order systems with time delay", Automatica, Vol. 37, No. 12, 2001, pp. 2025-2031 .

[6] G. J. Silva, A. Datta, S. P. Bhattacharyya, "New results on the synthesis of PID controllers", IEEE Transactions on Automatic Control, Vol. 47, No. 2, 2002, pp. 241-252.

[7] G. J. Silva, A. Datta, S. P. Bhattacharyya, "PID controllers for time delay systems", Birkhauser, 2005, ISBN: 0817642668.

[8] D. J. Wang, "Further results on the synthesis of PID controllers", IEEE Transactions on Automatic Control, Vol. 52, No. 6, 2007, pp. 1127-1132.

[9] D. J. Wang, "Stabilizing regions of PID controllers for n-th order all pole plants with dead time", IET Control Theory & Applications, Vol. 1, No. 4, 2007, pp. 1068-1074.

[10] V. L. Kharitonov, S. Niculescu, J. Moreno, W. Michiels, "Static output stabilization: Necessary conditions for multiple delay controllers", IEEE Transactions on Automatic Control, Vol. 50, No. 1, 2005, pp. 82-86.

[11] N. Hohenbicher, J. Ackermann, "Computing stable regions in parameter spaces for a class of quasi-polynomials", Proc. 4th IFAC Workshop on Time Delay Systems TDS'03, Recquencourt, France, 2003.

[12] E. N. Gryaznia, B. T. Polyak, "Stability regions in the parameter space: D-decomposition revisited", Automatica, Vol. 42, No. 1, 2006, pp. 13-26.

[13] D. E. Goldberg, "Genetic algorithms in search, optimization and machine learning", Addison-Wesley, 1989, ISBN: 0201157675.

[14] M. Melanie, "An introduction to genetic algorithms", MIT Press, 1998, ISBN: 0262631857.

[15] R. L. Haupt, S. E. Haupt, "Practical genetic algorithms", John Wiley & Sons, 2004, ISBN: 0471188735.

[16] R. M. Jan, C. S. Tseng, R. J. Lin, "Robust PID control design for permanent magnet synchronous motor: A genetic approach", Electric Power Systems Research, Vol. 78, No. 7, 2008, pp. 1161-1168.

[17] C. K. Chen, H. H. Koo, J. J. Yan, T. L. Liao, "GA-based PID active queue management control design for a class of TCP communication networks", Expert Systems with Applications , Vol. 36, No. 2, 2009, pp. 1903-1913.

[18] H. C. Chen, S. H. Chang, "Genetic algorithms based optimization design of a PID controller for an active magnetic bearing", International Journal of Computer Science and Network , Vol. 6, No. 18, 2006, pp. 95-99.

[19] A. Seuret, F. Michaut, J. P. Richard, T. Divoux, "Network control using GPS synchronization", Proc. American Control Conference, Minneapolis, Minnesota, USA, 2006, pp. 4195-4200.

Biographies

Karim Saadaoui received his Ph.D. at the Electrical and Electronics Engineering Department of the University of Bilkent of Ankara in 2003. He is a researcher at the Research unit LA.R.A. Automatique of the National Engineering School of Tunis (ENIT), Tunisia. Dr. Saadaoui's research interests are in the areas of time delay systems, stability robustness, and applications of robust control to process control problems.

Ayoub Moussa was born in 1983. He received the Diplome D'Ingenieur (Engineer's degree) in Electrical Engineering and the Masters' degree in Control and Signal Processing from the National Engineering School of Tunis (ENIT) in 2007 and 2008, respectively. His research interests include analysis and control of time delay systems.

Mohamed Benrejeb was born in 1950. He received the Engineering diploma in 1973 from the North Industrial (IDN currently Central School of Lille), France. In 1976 he received the Engineering Doctor diploma in Automatic from Technology and Science University of Lille and the Doctorate es Physics Sciences from the same university in 1980. He is currently professor in higher education in the National Engineering School of Tunis (ENIT) and the Central School of Lille. His fields of research include system control, modeling, analysis and synthesis of certain and uncertain continuous systems by conventional and nonconventional approaches and recently discrete event systems.

A NOVEL TECHNIQUE FOR THE DESIGN OF LOCALLY TUNEABLE DECENTRALISED ROBUST CONTROLLERS

L. F. Yeung [1], G. Lu [1], A. Nobakhti [2, *], D. W. C. Ho [3], H. Wang [2]

[1] Department of Electronic Engineering, City University of Hong Kong

[2] Control Systems Centre, School of Electrical Engineering and Electronics, University of Manchester

[3] Department of Mathematics, City University of Hong Kong

ABSTRACT

This paper proposes a decentralised controller design procedure for weakly coupled systems. A key feature of the design method is that the problem of designing a complete decentralised controller is replaced by several simpler local design problems. This is achieved by introducing a decomposition condition, which imposes local design constraints. This means that the design of each local controller is completely decoupled from other controllers. This has both design, and computational benefits. For the design, as long as each local controller satisfies the local decomposition condition, its design will be independent of the other controllers. In turn, this facilitates tuning and commissioning of the controller and the various design stages such as the choice of weighting functions. Most importantly this means that each of the loop-controllers is locally tunable. To achieve this, the decomposition condition is combined into a set of linear matrix inequalities (LMIs), then a sub-optimal robust solution for this type of control problem is obtained. The approach has been applied to several numerical examples and used for a case study of a gas turbine engine controller design.

Keywords

Decentralised Controller, Large Scale Systems, System Decomposition, Assignment Problem.

1. INTRODUCTION

Despite great advances in the design of centralised controllers for multiple-input multiple output (MIMO) systems, the predominant preferred choice of controller strutted in the industry has remained decentralised. Decentralised controllers are composed of several sub-controller with each of those being responsible for a portion of the MIMO system being controlled [1-3]. Traditionally, these controllers where attractive due to their reduced computational requirements. These days, computational power is a secondary issue, nevertheless, decentralised control still remains the preferred choice of control structure in the industry for other reasons such as maintenances, operation, modeling costs, installation and commissioning (see [39] for an excellent discussion on this issue).

A system which is particularly suited for decentralised control consists of a number of interconnected subsystems. When the couplings between these subsystems are "weak", this special decentralised structure can be approximated by a dominant block-diagonal structure plus an error or perturbation term that consists of all the coupling parts of the system [2, 6, 10]. The stabilisation of the overall system can then be replaced by the stabilisation of the dominant block structured system subject to a decomposition condition [6, 18, 20, 21].

Owing to the difficulty of enforcing a decentralised structure on a control system which includes an observer/estimator, the majority of decentralised control techniques are frequency based methods [3, 10, 11, 19]. However, during the last three decades two distinct groups of decentralised control techniques have emerged within the frequency domain techniques. One group are the more classical methods such as the sequential loop closing or the Nyquist array methods [38]. The primary advantage of these are their simplicity and the fact that each sub-controller is designed separately. This makes these controllers locally tunable. However, these classical techniques have the downside the results were not optimal and it was difficult to impose important system characteristics such as robustness.

The other family of decentralised control techniques are based on the more modern optimal control theory. In general, they have higher performance and can be made to be robust against system uncertainties [11, 16, 19, 37]. The downside is that, although the structure of these controllers is decentralised, the controller design process is still centralised and the controller is treated as a single entity. It is therefore designed as a whole, and individual sub-controllers cannot be redesigned or tuned according to specifications. This is not desirable since industrial user often require in-situ tuning of their controllers after they have been designed and installed. Moreover in many process applications the control systems are usually tuned and commissioned in a loop-by-loop manner [17].

This work draws inspiration from these two families of techniques by proposing a method which uses advanced optimal control theory to design decentralised controllers which are locally designed and tunable. This means that each local controller can be designed without knowledge of the other controllers in the decentralised controller, but the overall decentralised controller is guaranteed to be stabilising. It is shown here that in this context each local controller may be designed by solving a convex optimisation problem formulated using linear matrix inequality. Efficient interior-point algorithms are now available to solve the generic LMI problems [4, 9].

*Corresponding author: *E-mail:* nobakhti@iee.org

 ISSN: 1743-9310

The remainder of this paper is organized as follows. In Section 2, a frequency domain sufficiency condition is used to decompose a system into a number of decentralised subsystems (see **Theorem 2.1**). By **Lemma 2.1**, this decomposition condition can be transformed into infinity-norm constraints where each constraint involves only the corresponding local controller local nominal subsystem respectively. In Sections 3 and 4, this infinity-norm constraint together with the optimal criteria are integrated into a single LMI problem, which allows each local controller to be designed and implemented separately together with its local sensors and actuators. Finally in Section 5, the developed formulation is demonstrated by presenting step by step solution of 3 examples which include a spring mass friction system and a twin-spool gas turbine engine.

2. SYSTEM DECOMPOSITION

In this section, first, a decomposition condition is presented which shows when the stability of a large system can be inferred directly from the stability of its diagonal (local) systems. Then, an upper bound is found for this condition using the infinity norm which allows for this to be integrated into the subsequent LMI problems.

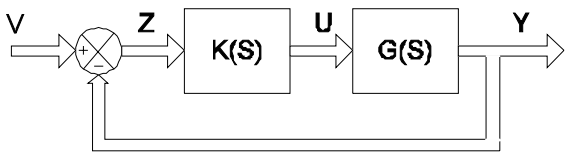

Figure 1. Closed-loop system

Consider a linear feedback system as shown in Fig. 1, for $G(s) \in \mathcal{R}_p^{n\times n}(s)$ where $\mathcal{R}_p^{n\times m}(s)$ is the set of $n \times m$ rational proper transfer function matrices. $G(s)$ has p_0 unstable poles and can be described in the following form,

$$G(s) := \begin{pmatrix} G_{11}(s) & G_{12}(s) & \cdots & G_{1N}(s) \\ G_{21}(s) & G_{22}(s) & \cdots & G_{2N}(s) \\ \vdots & \vdots & \ddots & \vdots \\ G_{N1}(s) & G_{N2}(s) & \cdots & G_{NN}(s) \end{pmatrix} \quad (1)$$

Let

$$G(s) = \overline{G}(s) + \Delta(s)$$

where

$$\overline{G}(s) := blkdiag\{G_{11}(s), G_{22}(s), \cdots, G_{NN}(s)\}$$
$$\Delta(s) = G(s) - \overline{G}(s) := \left(\Delta_1^o(s) \,|\, \Delta_2^o(s) \,|\, \cdots \,|\, \Delta_N^o(s)\right), \quad (2)$$

where

$$\Delta_i^o(s) \in \mathcal{R}_p^{n\times n_i}(s);\ G_{ij}(s) \in \mathcal{R}_p^{n_i\times n_j}(s);$$
$$N > 1;\ i, j = 1, 2, \cdots, N;\ \sum_{i=1}^{N} n_i = n.$$

The nominal system is $\overline{G}(s)$ with p_0 unstable poles and $\Delta(s) \in RH_\infty$ represents the inter-connection between sub-systems. $\Delta(s)$ is partitioned vertically into N block matrices $\Delta_i^0(s)$ and it is noted that it can also be regarded as the uncertainties of a system [14, 18], where the uncertainties are always assumed to be in RH_∞. Let $K(s)$ be a decentralised pre-compensator with the following structure,

$$K(s) := blkdiag\{K_{11}(s), K_{22}(s), \cdots, K_{NN}(s)\},$$

where $K_{ii}(s) \in \mathcal{R}_p^{n_i\times n_i}(s)$, $i = 1, 2$. In Fig. 1, $Y(s)$ and $V(s)$ are vectors representing the output and input of the this closed-loop system, respectively. The transfer function matrix $H(s)$ of the overall closed-loop system is:

$$Y(s) = H(s)V(s) = G(s)K(s)[I + G(s)K(s)]^{-1}V(s) \quad (4)$$

The return difference matrix is:

$$I + G(s)K(s) = R(s) + Q_\Delta(s) \quad (5)$$

where

$$R(s) := I + \overline{G}(s)K(s)$$
$$Q_\Delta(s) := \Delta(s)K(s)$$

Note that $R(s)$ is a block diagonal matrix. The following theorem provides the condition that if the interconnection $Q_\Delta(s)$ is "weak" relative to $R(s)$, then the stabilisation problem is reduced to the stabilisation problem of the nominal system $\overline{G}(s)$ only.

Theorem 2.1 [6, 7] *Let $I + G(s)K(s)$ have a regular splitting (Regular splitting of a matrix means $Z = A + B$ where A is invertible) $I + G(s)K(s) = R(s) + Q_\Delta(s)$, where $G(s)$ and $\overline{G}(s)$ have p_0 unstable poles. The closed-loop system as shown in* Fig. 1 *is asymptotically stable if*

$$\text{C1)}: K(s) \text{ stabilises the nominal system } \overline{G}(s), \text{ and}$$
$$\text{C2)}: \rho(Q_\Delta(s)R^{-1}(s)) < 1, \quad \text{for all } s \in \mathcal{D}, \quad (6)$$

where $\mathcal{D}$ is the usual Nyquist contour.

If $\overline{G}(s)$ is chosen to be a block-diagonal system matrix, then the above decomposition theorem enables us to approximate a block-structured system by a block-diagonal nominal system. The error of this approximation will be $\Delta(s)$. The positive quantity $\rho(Q_\Delta(s)R^{-1}(s))$ is a measure of the size of the inter-coupling between sub-systems. If condition (6) is satisfied, then the system (1) is called a *weakly coupled system*.

Theorem 2.1 enables a system to be decomposed into N subsystems, each with its own local controllers $K_{jj}(s)$, which can be designed, tuned and commissioned separately. However, the decomposition condition (6) involves $K(s)$ which consists of all the local controller $K_{jj}(s)$. The consequence is that this condition is not "local", i.e. at the j^{th} local design, condition (6) depends on all other local controllers $K_{jj}(s)$, $j = 1 \ldots N$. Therefore a full decomposed design structure cannot be realised. The following section will show how this problem can be ratified by relaxing this measure to arrive at a full decomposition condition.

Proposition 2.1 [7, 14, 18] *The system (1) is weakly coupled and can be decomposed if*

$$\text{C3}): \rho(Q_\Delta(s)R^{-1}(s)) \le \| Q_\Delta(s)R^{-1}(s) \|_\infty < 1, \quad (7)$$

Note that (7) ensure (6) to be satisfied. The following lemma is needed to obtain the full decomposition condition.

Lemma 2.1 Let $A(s) \in \mathcal{R}_p^{n\times n}(s)$, *then*

$$\| A(s) \|_\infty \le \sqrt{N} \cdot \max_{1\le j\le N} \| A_j(s) \|_\infty;$$

where

$$A(s) \in RH_\infty, \text{ and } A(s) = \left(A_1(s) \mid A_2(s) \mid \cdots \mid A_N(s) \right),$$
$$A_j(s) \in \mathcal{R}_p^{n\times n_j}(s), \sum_{j=1}^{N} n_j = n.$$

Proof: It can be shown that

$$\begin{aligned} \| A(s) \|_\infty^2 &= \sup_{0\le\omega<\infty} \sigma_{\max}[A^*(j\omega)A(j\omega)] \\ &= \sup_{0\le\omega<\infty} \sigma_{\max}[\sum_{i=1}^{N} A_i(j\omega)A_i^*(j\omega)] \\ &\le \sum_{i=1}^{N} \sup_{0\le\omega<\infty} \sigma_{\max}[A_i(j\omega)A_i^*(j\omega)] \\ &\le N \cdot \max_{1\le i\le N} \| A_i(s) \|_\infty^2 . \end{aligned} \quad (8)$$

Taking the square root on both sides yields the result.

Note that the matrix

$$\Delta_j^o(s) = \left(G_{1j}'(s) \mid \cdots \mid G_{j-1\,j}'(s) \mid 0 \mid G_{j+1\,j}'(s) \mid \cdots \mid G_{Nj}'(s)' \right)$$

is a sub-matrix of $\Delta(s)$ and,

$$Q_\Delta(s)R^{-1}(s) = \left(\Delta_1 K_{11} R_{11}^{-1}(s) \mid \Delta_2 K_{22} R_{22}^{-1}(s) \mid \cdots \mid \Delta_N K_{NN} R_{NN}^{-1}(s) \right), \quad (9)$$

where

$$R_{jj}(s) := I + G_{jj}(s)K_{jj}(s), \quad j = 1, 2, \cdots, N$$

The j^{th}-column of $Q_\Delta(s)R^{-1}(s)$ depends on $K_{jj}(s)$ only.

Corollary 2.1 *System (1) is weakly coupled and can be fully decomposed if any one of the following conditions are satisfied*

$$\text{C4}): \| Q_\Delta(s)R^{-1}(s) \|_\infty \le c \cdot \max_j \| \Delta_j^o(s)K_{jj}(s)R_{jj}^{-1}(s) \|_\infty < 1, \quad (10)$$

where $c = \sqrt{N}$.

$$\text{C5}): \| \Delta(s) \|_\infty \cdot \max_j \| K_{jj}(s)R_{jj}^{-1}(s) \|_\infty < 1 \quad (11)$$

Proof: If $Q_\Delta(s)R^{-1}(s) \in RH_\infty$, then C4) follows from **Lemma 2.1** and (9). Condition C5) is due to the observation that

$$\begin{aligned} \| Q_\Delta(s)R^{-1}(s) \|_\infty &= \| \Delta(s) \cdot blkdiag \left\{ K_{jj}(s)R_{jj}^{-1}(s) \right\} \|_\infty \\ &= \| \Delta(s) \|_\infty \cdot \max_j \| K_{jj}(s)R_{jj}^{-1}(s) \|_\infty \end{aligned}$$

By using (10), the decomposition condition (C3) can be satisfied if

$$c \cdot \| \Delta_j^o(s)K_{jj}(s)R_{jj}^{-1}(s) \|_\infty < 1, \quad \forall j = 1, 2, \cdots, N \quad (12)$$

or

$$\| \Delta(s) \|_\infty \cdot \| K_{jj}(s)R_{jj}^{-1}(s) \|_\infty \le 1, \quad \forall j = 1, 2, \cdots, N \quad (13)$$

Conditions (12) and (13) have an important property: they are dependent on $K_{jj}(s)$ and $G_{jj}(s)$ only. As long as this is satisfied for all $j = 1, 2, \ldots, N$, the decomposition condition (6) can be satisfied. This feature is useful in the decomposed design framework since it allows one to concentrate on the design of the j^{th} local controller and it can guarantee that the local design will not destabilise other subsystems. In condition (12) both the phase and magnitude of $\Delta_s^o(s)$ are available to be used by $K_{jj}(s)$ to reduce $\| \Delta_s^o(s)K_{jj}(s)R_{jj}^{-1}(s) \|$. However, in condition (13), the phase information is lost due to the factorisation of $\| \Delta(s) \|$ which could make the inequality more conservative. On the other hand, condition (13) only requires state-space realisations of $K_{jj}(s)$ and $R_{jj}^{-1}(s)$, thus making the resulting LMIs simpler and smaller. Since $\Delta(s)$ has a zero diagonal, it can be reduced into a new matrix $\Delta_s^o(s)$ as follows,

$$\begin{aligned} \Delta_j(s) &:= \left(G_{1\,j}'(s) \mid \cdots \mid G_{j-1\,j}'(s) \mid G_{j+1\,j}'(s) \mid \cdots \mid G_{Nj}'(s) \right)' \\ &\in \mathcal{R}_p^{(n-n_j)\times n_j}(s) \end{aligned} \quad (14)$$

With this alternative representation and since

$$\| \Delta_j(s)K_{jj}(s)R_{jj}^{-1}(s) \|_\infty = \| \Delta_j^o(s)K_{jj}(s)R_{jj}^{-1}(s) \|_\infty,$$

the dimension of the realisation can be reduced.

3. DECENTRALISED STABILISATION

In this section, we will first give some sufficient conditions for stability of decentralised systems, and then present a design algorithm for these decentralised controllers. Let the state space realisations of $G_{jj}(s)$ and $K_{jj}(s)$ be,

$$G_{jj}(s) = \left(\begin{array}{c|c} A_{jj} & B_{jj} \\ \hline C_{jj} & 0 \end{array} \right), \quad K_{jj}(s) = \left(\begin{array}{c|c} A_{K_{jj}} & B_{K_{jj}} \\ \hline C_{K_{jj}} & D_{K_{jj}} \end{array} \right) \quad (15)$$

Then from [13] it follows that,

$$(I+G_{jj}(s)K_{jj}(s))^{-1}= \left(\begin{bmatrix} A_{jj}-B_{jj}D_{K_{jj}}C_{jj} & B_{jj}C_{K_{jj}} \\ -B_{K_{jj}}C_{jj} & A_{K_{jj}} \end{bmatrix} \begin{bmatrix} B_{jj}D_{K_{jj}} \\ B_{K_{jj}} \end{bmatrix} \begin{bmatrix} -C_{jj} & 0 \end{bmatrix} \quad I \right) \tag{16}$$

and

$$\Delta_j(s)=\left(\begin{array}{c|c} A_j & B_j \\ \hline C_j & 0 \end{array}\right) \tag{17}$$

Similarly,

$$\Delta_j(s)K_{jj}(s)(I+G_{jj}(s)K_{jj}(s))^{-1}=\left(\begin{array}{c|c} \hat{A}_j & \hat{B}_j \\ \hline \hat{C}_j & \hat{D}_j \end{array}\right) \tag{18}$$

where

$$\hat{A}_j=\begin{pmatrix} A_j & -B_jD_{K_{jj}}C_{jj} & B_jC_{K_{jj}} \\ 0 & A_{jj}-B_{jj}D_{K_{jj}}C_{jj} & B_{jj}C_{K_{jj}} \\ 0 & -B_{K_{jj}}C_{jj} & A_{K_{jj}} \end{pmatrix} \tag{19}$$

$$\hat{B}_j=\begin{pmatrix} B_jD_{K_{jj}} \\ B_{jj}D_{K_{jj}} \\ B_{K_{jj}} \end{pmatrix}, \hat{C}_j=C_j 00,\ \hat{D}_j=0 \tag{20}$$

Theorem 2.1 and **Proposition 2.1** imply that condition C1) is satisfied if the transfer function matrices

$$G_{jj}(s)K_{jj}(s)(I+G_{jj}(s)K_{jj}(s))^{-1}$$

is stable for $j = 1, 2, \ldots, N$. Thus, the following decentralised stability condition is obtained.

Theorem 3.1 *There exists a controller (3) such that the closed-loop system shown in* Fig. 1 *is asymptotically stable if there exist two positive definite matrices X_j and Y_j of appropriate dimensions such that the following linear matrix inequalities (LMIs) hold:*

$$\tilde{A}_j'X_j+X_j\tilde{A}_j+\tilde{C}_j<0 \tag{21}$$

$$\begin{pmatrix} (\tilde{B}_{j\perp})' & 0 \\ 0 & I \end{pmatrix}\begin{pmatrix} \tilde{A}_jY_j+Y_j\tilde{A}_{j'} & Y_jC_{0j}' \\ C_{0j}Y_j & -I \end{pmatrix}\begin{pmatrix} \tilde{B}_{j\perp} & 0 \\ 0 & I \end{pmatrix}<0 \tag{22}$$

$$\begin{pmatrix} X_j & I \\ I & Y_j \end{pmatrix}\geq 0 \tag{23}$$

where

$$\tilde{A}_j = \begin{pmatrix} A_j & 0 \\ 0 & A_{jj} \end{pmatrix}, \tilde{C}_j=\begin{pmatrix} c^2C_j'C_j & 0 \\ 0 & -C_{jj}'C_{jj} \end{pmatrix}, \tag{24}$$

$$\tilde{B}_j = \begin{pmatrix} B_j' & B_{jj}' \end{pmatrix},\quad C_{0j}=\begin{pmatrix} cC_j & 0 \end{pmatrix},\quad j=1,2,\cdots,N$$

and $\mathcal{N}(X)$ denotes the null space of X, and $X_\perp$ denotes a matrix whose columns span $\mathcal{N}(X)$

Proof: Using the Bounded Real Lemma (see [4, 14]), it can be shown that

$$\Delta_j(s)K_{jj}(s)(I+G_{jj}(s)K_{jj}(s))^{-1},$$

is stable and

$$c\,\|\Delta_j(s)K_{jj}(s)(I+G_{jj}(s)K_{jj}(s))^{-1}\|_\infty<1$$

if there exists a positive definite matrix P_j such that

$$\begin{pmatrix} P_j\hat{A}_j+\hat{A}_j'P_j & P_j\hat{B}_j & c\hat{C}_j' \\ \hat{B}_j'P_j & -I & c\hat{D}_j' \\ c\hat{C}_j & c\hat{D}_j & -I \end{pmatrix}<0 \tag{25}$$

Therefore it follows from **Theorem 2.1** that **Theorem 3.1** holds if (25) holds. Let

$$\hat{A}_{0j}:=\begin{pmatrix} A_j & 0 & 0 \\ 0 & A_{jj} & 0 \\ 0 & 0 & 0 \end{pmatrix}, \Phi_j:=\begin{pmatrix} P_j\hat{A}_{0j}+\hat{A}_{0j}'P_j & 0 & c\hat{C}_j' \\ 0 & -I & 0 \\ c\hat{C}_j & 0 & -I \end{pmatrix},$$

$$\Lambda_j:=\begin{pmatrix} P_j & 0 & 0 \\ 0 & I & 0 \\ 0 & 0 & I \end{pmatrix}, \Pi_j:=\left(\begin{bmatrix} B_j' & B_{jj}' & 0 \\ 0 & 0 & I \end{bmatrix} \begin{bmatrix} 0 \\ 0 \end{bmatrix} \begin{bmatrix} 0 \\ 0 \end{bmatrix}\right), \tag{26}$$

$$\Psi_j := \left(\begin{bmatrix} 0 & 0 & 0 \\ 0 & -C_{jj} & I \end{bmatrix} \begin{bmatrix} 0 \\ I \end{bmatrix} \begin{bmatrix} 0 \\ 0 \end{bmatrix} \right),$$
$$\Xi_j = \begin{pmatrix} C_{K_{jj}} & D_{K_{jj}} \\ A_{K_{jj}} & B_{K_{jj}} \end{pmatrix}, j = 1, 2, \cdots, N. \quad (26)$$

Then, (25) is equivalent to

$$\Phi_j + \Lambda_j \Pi_j' \Xi_j \Psi_j + (\Lambda_j \Pi_j' \Xi_j \Psi_j)' < 0 \quad (27)$$

From [12], it can be seen that (27) is equivalent to

$$\Psi_{j\perp}' \Phi_j \Psi_{j\perp} < 0, \quad (28)$$

$$\Pi_{j\perp}' \Lambda_j^{-1} \Phi_j \Lambda_j^{-1} \Pi_{j\perp} < 0 \quad (29)$$

After some algebraic manipulations, we can show (28) and (29) are equivalent to (21)-(23).

Finally, we show that the stability of the state-space realisation (18) for $\Delta_j K_{jj}(I + G_{jj}K_{jj})^{-1}$ implies the stability of (16); that is, K_{jj} stabilises G_{jj} with j = 1, 2, …, N. From (19) and the stability of the state-space realisation (18) for $\Delta_j K_{jj}(I + G_{jj}K_{jj})^{-1}$, it follows that,

$$\lambda(\hat{A}_j) \subset C^- \quad (30)$$

where C$^-$ is the left hand complex plant. Therefore,

$$\lambda \begin{pmatrix} A_{jj} - B_{jj} D_{K_{jj}} C_{jj} & B_{jj} C_{K_{jj}} \\ -B_{K_{jj}} C_{jj} & A_{K_{jj}} \end{pmatrix} \subset C^- \quad (31)$$

and the proof is completed.

The criterion of **Theorem 3.1** is given in terms of Linear Matrix Inequalities (LMI) and thus has the following advantages: 1) it does not involve any parameter tuning and 2) it can be tested numerically efficiently using interior point algorithms that have been developed for solving linear matrix inequalities [4, 5].

The following is a design procedure for finding a stabilising K_{jj} that satisfies the decomposition condition (12).

Step 1. Find X_j and Y_j:

Find positive definite solutions X_j and Y_j that satisfy LMI's (21), (22) and (23).

Step 2. Determine matrix P_j:

Let

$$\kappa_j := rank(I - X_j Y_j) \le n_j \quad (32)$$

where n_j is the order of the given subsystem. Then, compute two full-column-rank constant matrices $M_j, N_j \in R^{n_j \times \kappa_j}$ such that,

$$M_j N_j' = I - X_j Y_j \quad (33)$$

Next, find the unique solution $P_j \in R^{(n_j + \kappa_j) \times (n_j + \kappa_j)}$ from the following linear equation,

$$P_j \begin{pmatrix} I & Y_j \\ 0 & N_{j'} \end{pmatrix} = \begin{pmatrix} X_j & I \\ M_{j'} & I \end{pmatrix} \quad (34)$$

Note that (34) is always solvable provided that $Y_j > 0$ and M_j is of full column rank [15].

Step 3. Construct a set of parameterised controllers K_{jj}:

Then, for a given P_j, a parameterisation of a set of controllers is given by

$$\mathcal{K}_j = \left\{ K_{jj}(s) = \begin{pmatrix} A_{K_{jj}} & B_{K_{jj}} \\ C_{K_{jj}} & D_{K_{jj}} \end{pmatrix} \middle| \right.$$
$$\left. \Phi_j + \Lambda_j \Pi_j' \Xi_j \Psi_j + \Psi_j' \Xi_j' \Pi_j \Lambda_j < 0 \right\} \quad (35)$$

4. DECENTRALISED H∞ OPTIMISATION PROBLEM WITH CONSTRAINTS

In previous sections a decentralised stabilisation problem is given. In this section, this problem is extended to a decentralised H_∞ optimisation problem. For the j^{th} subsystem design, the objective is to determine the j^{th} local controller K_{jj} which stabilises the subsystem G_{jj} subject to condition C4). This problem can be re-stated in a constrained H_∞ form as follows:

Let ν be the external input, $z = v - y$ be the error of control, and u is the control input to the system G. For simplicity, the additive perturbation is assumed to be zero for clarity (note that this additive perturbation can be absorbed into condition C4) or C5).

Then the optimal local controllers can be found by solving the following problem:

$$P_0 : \min \left\| F_{1j}(P_{jj}(s), K_{jj}(s)) \right\|_\infty \quad (36)$$

subject to conditions C1) with

$$\bar{G}(s) = blkdiag\left\{ G_{jj}(s) \right\}, \text{and } \bar{K}(s) = blkdiag\left\{ K_{jj}(s) \right\}$$

and condition C4) of **Corollary 2.1**

where

$$F_{1j}(P_{jj}(s), K_{jj}(s)) := (I + G_{jj}(s)K_{jj}(s))^{-1}$$
$$:= P_{11}(s) + P_{12}(s)K_{jj}(s)(I - P_{22}(s)K_{jj}(s))^{-1}P_{21}(s) \quad (37)$$

with

$$P_{11}(s) := I, \quad P_{12}(s) := -G_{jj}(s),$$
$$P_{21}(s) := I, \quad P_{22}(s) := -G_{jj}(s) \tag{38}$$

In the following, the more general case of the weighted H_∞ is considered. Let $W_j(s)$ and $\tilde{W}_j(s)$ are stable weighting factors with realisations,

$$W_j(s) = \begin{pmatrix} W_{aj} & W_{bj} \\ W_{cj} & W_{dj} \end{pmatrix}, \quad \tilde{W}_j(s) = \begin{pmatrix} \tilde{W}_{aj} & \tilde{W}_{bj} \\ \tilde{W}_{cj} & \tilde{W}_{dj} \end{pmatrix} \tag{39}$$

If there exists a controller K_{jj} such that $\hat{A}_j$, (19), is stable, then K_{jj} can be found by

$$\min_{K_{jj}} \| W_j (I + G_{jj} K_{jj})^{-1} \|_\infty$$

subject to

$$c \| \tilde{W}_j \Delta_j K_{jj} (I + G_{jj} K_{jj})^{-1} \|_\infty < 1$$

Let z_j and $\tilde{z}_j$ be two controlled output with appropriate dimensions respectively, w_j and u_j be the j^{th} disturbance and the j^{th} control input with appropriate dimensions respectively, and suppose that

$$z_j = W_j(s)(I + G_{jj}(s)K_{jj}(s))^{-1} w_j,$$
$$\tilde{z}_j = c\tilde{W}_j(s)\Delta_j(s)K_{jj}(s)(I + G_{jj}(s)K_{jj}(s))^{-1} w_j \tag{40}$$

In order to apply the results in [8], the systems need to have a common system matrix (A_j^a) and control matrix (B_j^a) ,i.e.,

$$W_j(s)(I + G_{jj}(s)K_{jj}(s))^{-1} = \begin{pmatrix} A_j^a & B_j^a \\ C_j^a & W_{dj} \end{pmatrix} \tag{41}$$

$$c\tilde{W}_j(s)\Delta_j(s)K_{jj}(s)(I + G_{jj}(s)K_{jj}(s))^{-1} = \begin{pmatrix} A_j^a & B_j^a \\ \tilde{C}_j^a & 0 \end{pmatrix}$$

where

$$A_j^a := \begin{pmatrix} W_{aj} & 0 & 0 & 0 & -W_{bj}C_{jj} \\ 0 & \tilde{W}_{aj} & c\tilde{W}_{bj}C_j & 0 & 0 \\ 0 & 0 & A_j & B_j C_{K_{jj}} & -B_j D_{K_{jj}} C_{jj} \\ 0 & 0 & 0 & A_{K_{jj}} & -B_{K_{jj}} C_{jj} \\ 0 & 0 & 0 & B_{jj} C_{K_{jj}} & A_{jj} - B_{jj} D_{K_{jj}} C_{jj} \end{pmatrix}$$

$$B_j^a := \begin{pmatrix} W_{bj} \\ 0 \\ B_j D_{K_{jj}} \\ B_{K_{jj}} \\ B_{jj} D_{K_{jj}} \end{pmatrix} \tag{42}$$

$$C_j^a := \begin{pmatrix} W_{cj} & 0 & 0 & 0 & -W_{dj}C_{jj} \end{pmatrix},$$
$$\tilde{C}_j^a := \begin{pmatrix} 0 & \tilde{W}_{cj} & c\tilde{W}_{dj}C_j & 0 & 0 \end{pmatrix}$$

Similar to the proof of **Theorem 3.1**, from the *Bounded Real Lemma* (see [4, 14]), it follows that

$$c \| \tilde{W}_j(s)\Delta_j(s)K_{jj}(s)(I + G_{jj}(s)K_{jj}(s))^{-1} \|_\infty < 1,$$
$$\| W_j(s)(I + G_{jj}(s)K_{jj}(s))^{-1} \|_\infty < \gamma$$

if there exist two positive definite matrices X_j^a and Y_j^a such that

$$\begin{pmatrix} A_j^a X_j^a + A_j^{a\prime} X_j^a & B_j^a & X_j^a \tilde{C}_j^{a\prime} \\ B_j^{a\prime} & -I & 0 \\ \tilde{C}_j^a X_j^a & 0 & -I \end{pmatrix} < 0 \tag{43}$$

$$\begin{pmatrix} A_j^a Y_j^a + A_j^{a\prime} Y_j^a & B_j^a & Y_j^a C_j^{a\prime} \\ B_j^{a\prime} & -\gamma I & W_{dj}' \\ C_j^a Y_j^a & W_{dj} & -\gamma I \end{pmatrix} < 0 \tag{44}$$

A common approach of turning an H_∞ optimisation problem into a convex problem [8] is to use a common Lyapunov matrix $X_j^a = Y_j^a$ for (43) and (44). Therefore the problem P_0 of (36) can be converted into solving the following suboptimal H_∞ synthesis:

$$P_1 : \min_{K_{jj}} \gamma \tag{45}$$

subject to conditions (43) and (44) with $X_j^a = Y_j^a$. Thus, (41) and (42) become,

$$\begin{pmatrix} \dot{x}_{j1} \\ \dot{x}_{j2} \\ \dot{x}_{j3} \\ \dot{x}_{j4} \end{pmatrix} = \begin{pmatrix} W_{aj} & 0 & 0 & -W_{bj}C_{jj} \\ 0 & \tilde{W}_{aj} & c\tilde{W}_{bj}C_j & 0 \\ 0 & 0 & A_j & 0 \\ 0 & 0 & 0 & A_{jj} \end{pmatrix} \begin{pmatrix} x_{j1} \\ x_{j2} \\ x_{j3} \\ x_{j4} \end{pmatrix}$$
$$+ \begin{pmatrix} W_{bj} \\ 0 \\ 0 \\ 0 \end{pmatrix} w_j + \begin{pmatrix} 0 \\ 0 \\ B_j \\ B_{jj} \end{pmatrix} u_j$$

$$
\begin{aligned}
z_j &= \begin{pmatrix} W_{cj} & 0 & 0 & -W_{dj}C_{jj} \end{pmatrix} \begin{pmatrix} x_{j1} \\ x_{j2} \\ x_{j3} \\ x_{j4} \end{pmatrix} + W_{dj} w_j + 0u_j, \\
\tilde{z}_j &= \begin{pmatrix} 0 & \tilde{W}_{cj} & c\tilde{W}_{dj}C_j & 0 \end{pmatrix} \begin{pmatrix} x_{j1} \\ x_{j2} \\ x_{j3} \\ x_{j4} \end{pmatrix} + 0w_j + 0u_j, \\
y_j &= -\begin{pmatrix} 0 & 0 & 0 & C_{jj} \end{pmatrix} \begin{pmatrix} x_{j1} \\ x_{j2} \\ x_{j3} \\ x_{j4} \end{pmatrix} + Iw_j, \\
\dot{\xi}_j &= A_{K_{jj}} \xi_j + B_{K_{jj}} y_j, \quad u_j = C_{K_{jj}} \xi_j + D_{K_{jj}} y_j,
\end{aligned}
\tag{46}
$$

where x_{jl} and w_j ($l = 1, 2, 3, 4$) are states and disturbance input with appropriate dimensions, respectively, ξ_j is the state of the j^{th} local compensator. For convenience (46) is rewritten in the following simple form,

$$
\begin{aligned}
\dot{x}_j &= A^{(j)} x_j + B_1^{(j)} w_j + B_2^{(j)} u_j, \\
z_j &= C_1^{(j)} x_j + D_{11}^{(j)} w_j, \\
\tilde{z}_j &= \tilde{C}_1^{(j)} x_j, \\
y_j &= C_2^{(j)} x_j + w_j,
\end{aligned}
\tag{47}
$$

where $x_j = (x'_{j1} x'_{j2} x'_{j3} x'_{j4})$, and all matrix parameters can be directly determined by (46).

Let $A^j \in \mathcal{R}^{\tilde{n}_j \times \tilde{n}_j}$ and k_j be the order of the ^{jth} subcontroller, then the positive definite matrix $X_j^a \in \mathcal{R}^{(\tilde{n}_j + k_j) \times (\tilde{n}_j + k_j)}$ and X_j^{a-1} can be partitioned as follows:

$$
\begin{aligned}
&X_j^a = \begin{pmatrix} R_j & M_j \\ M_j' & U_j \end{pmatrix}, X_j^{a-1} = \begin{pmatrix} S_j & N_j \\ N_j' & V_j \end{pmatrix}, \\
&R_j, S_j \in \mathcal{R}^{\tilde{n}_j \times \tilde{n}_j}
\end{aligned}
\tag{48}
$$

Define,

$$
\begin{aligned}
\mathcal{B}_{K_{jj}} &= N_j B_{K_{jj}} + S_j B_2^{(j)} D_{K_{jj}} \\
\mathcal{C}_{K_{jj}} &= C_{K_{jj}} M_j' + D_{K_{jj}} C_2^{(j)} R_j \\
\mathcal{A}_{K_{jj}} &= N_j A_{K_{jj}} M' + N_j B_{K_{jj}} C_2^{(j)} R_j + \\
&S_j B_2^{(j)} C_{K_{jj}} M_j' + S_j (A^{(j)} + B_2^{(j)} D_{K_{jj}} C_2^{(j)}) R_j
\end{aligned}
\tag{49}
$$

and let,

$$
\begin{aligned}
\Psi_{j11} &= \begin{pmatrix} A^{(j)} R_j + R_j A^{(j)'} + B_2^{(j)} \mathcal{C}_{K_{jj}} + \mathcal{C}_{K_{jj}}' B_2^{(j)'} & * \\ \mathcal{A}_{K_{jj}} + (A^{(j)} + B_2^{(j)} D_{K_{jj}} C_2^{(j)})' & A^{(j)} S_j + S_j A^{(j)'} + \mathcal{B}_{K_{jj}} C_2^{(j)} + C_2^{(j)'} \mathcal{B}_{K_{jj}}' \end{pmatrix} \\
\Psi_{j21} &= \begin{pmatrix} (B_1^{(j)} + B_2^{(j)} D_{K_{jj}})' & (S_j B_1^{(j)} + B_{K_{jj}})' \\ C_1^{(j)} R_j & C_1^{(j)} \end{pmatrix} \\
\Psi_{j22} &= \begin{pmatrix} -\gamma I & * \\ D_{11}^{(j)} & -\gamma I \end{pmatrix} \\
\Phi_{j11} &= \begin{pmatrix} A^{(j)} R_j + R_j A^{(j)'} + B_2^{(j)} \mathcal{C}_{K_{jj}} + \mathcal{C}_{K_{jj}}' B_2^{(j)'} & * \\ \mathcal{A}_{K_{jj}} + (A^{(j)} + B_2^{(j)} D_{K_{jj}} C_2^{(j)})' & A^{(j)} S_j + S_j A^{(j)'} + \mathcal{B}_{K_{jj}} C_2^{(j)} + C_2^{(j)'} \mathcal{B}_{K_{jj}}' \end{pmatrix} \\
\Phi_{j21} &= \begin{pmatrix} (B_1^{(j)} + B_2^{(j)} D_{K_{jj}})' & (S_j B_1^{(j)} + B_{K_{jj}})' \\ \tilde{C}_1^{(j)} R_j & \tilde{C}_1^{(j)} \end{pmatrix} \\
\Phi_{j22} &= \begin{pmatrix} -\gamma I & * \\ 0 & -\gamma I \end{pmatrix}
\end{aligned}
\tag{50}
$$

Then the following results can be obtained.

Theorem 4.1 *The modified suboptimal problem P_1 of (45) is solvable if and only if the following convex optimisation problem P_c is solvable:*

$$
P_c : \min_{\mathcal{A}_{K_{jj}}, \mathcal{B}_{K_{jj}}, \mathcal{C}_{K_{jj}}, D_{K_{jj}}, R_j' = R_j, S_j' = S_j} \gamma
\tag{51}
$$

subject to

$$
\begin{pmatrix} R_j & I \\ I & S_j \end{pmatrix} > 0
\tag{52}
$$

$$\begin{pmatrix} \Psi_{j11} & * \\ \Psi_{j21} & \Psi_{j22} \end{pmatrix} < 0, \tag{53}$$

$$\begin{pmatrix} \Phi_{j11} & * \\ \Phi_{j21} & \Phi_{j22} \end{pmatrix} < 0 \tag{54}$$

Proof: The proof is similar to [8].

From **Theorem 4.1** and [8], we can determine the j^{th} subcontroller as follows:

Step 1: Determine $\mathcal{A}_{K_{jj}}$, $\mathcal{B}_{K_{jj}}$, $\mathcal{C}_{K_{jj}}$, $D_{K_{jj}}$, $R_j = R'_j$, $S_j = S'_j$ and $\gamma > 0$ from convex optimisation problem (51).

Step 2: Find full-rank M_j and N_j such that $M_j N'_j = I - R_j S_j$.

Step 3: Compute $B_{K_{jj}}$, $C_{K_{jj}}$ and $A_{K_{jj}}$.

Step 4: Set $K_{jj}(s) = D_{K_{jj}} + C_{K_{jj}}(SI - A_{K_{jj}})^{-1} B_{K_{jj}}$.

In this case, $K_{jj}(s)$ is the smallest γ such that (45) holds.

5. EXAMPLES

In this section three examples will be considered. **Example 1** demonstrates the effectiveness of the algorithm in Section 3 where only a decentralised stabilising controller is designed. **Example 2** solves the optimisation problem via the H_∞ method, where weighting functions are introduced to emphasize the low frequency effect on the H_∞-norm in order to obtain good step responses and in **Example 3** the procedure is used to design a decentralised H_∞ controller for a benchmark gas turbine engine problem [36].

5.1 Example 1

Consider the following two-block system,

$$G(s) = \left(\begin{array}{c|c} G_{11}(s) & G_{12}(s) \\ \hline G_{21}(s) & G_{22}(s) \end{array}\right) = \tag{55}$$

$$\left(\begin{array}{cc|cc} \dfrac{-s+2}{s^2-3s+3} & \dfrac{-1}{s^2-3s+3} & \dfrac{0.125s}{s^2+3s+3} & \dfrac{0.125s+0.375}{s^2+3s+3} \\ \dfrac{1}{s^2-3s+3} & \dfrac{-s+1}{s^2-3s+3} & \dfrac{0.125}{s^2+3s+3} & \dfrac{-0.125s-0.25}{s^2+3s+3} \\ \hline \dfrac{0.3s+0.6}{s^2+3s+3} & \dfrac{-0.6}{s^2+3s+3} & \dfrac{-s+2}{s^2-3s+3} & \dfrac{s-1}{s^2-3s+3} \\ \dfrac{0.15}{s^2+3s+3} & \dfrac{0.3s+0.3}{s^2+3s+3} & \dfrac{-2s+2}{s^2-3s+3} & \dfrac{2}{s^2-3s+3} \end{array}\right)$$

with decentralised controller:

$$K(s) = BLKdiag\{K_{11}(s), K_{22}(s)\}$$

where K_{11} and K_{22} are two 2×2 sub-controllers. The minimal realisation of G_{ij} can be obtained as follows:

$$G_{11}(s) = \left(\begin{array}{cc|cc} 1 & 1 & 1 & 0 \\ -1 & 2 & 0 & 1 \\ \hline -1 & 0 & 0 & 0 \\ 0 & -1 & 0 & 0 \end{array}\right),$$

$$G_{12}(s) = \left(\begin{array}{cc|cc} -2 & 1 & 0.25 & 0 \\ -1 & -1 & 0 & 0.25 \\ \hline 0.5 & 0.5 & 0 & 0 \\ 0 & -0.5 & 0 & 0 \end{array}\right),$$

$$G_{21}(s) = \left(\begin{array}{cc|cc} -1 & -2 & 3 & 0 \\ 0.5 & -2 & 0 & 3 \\ \hline 0.1 & 0 & 0 & 0 \\ 0 & 0.1 & 0 & 0 \end{array}\right), \tag{56}$$

$$G_{22}(s) = \left(\begin{array}{cc|cc} 2 & -1 & 1 & 0 \\ 1 & 1 & 0 & 1 \\ \hline -1 & 1 & 0 & 0 \\ -2 & 0 & 0 & 0 \end{array}\right)$$

Step 1: Two pairs of the solutions from (21)-(23) are found as follows,

$$X_1 = \begin{pmatrix} 0.055 & -0.112 & 0.001 & -0.009 \\ -0.105 & 0.327 & 0.019 & 0.013 \\ 0.009 & 0.017 & 0.443 & -0.056 \\ -0.009 & 0.013 & -0.056 & 0.276 \end{pmatrix}$$

$$Y_1 = \begin{pmatrix} 150 & 17.32 & 1.084 & -6.639 \\ 12.12 & 69.74 & 2.607 & -1.74 \\ 0.99 & 2.597 & 2.517 & 0.224 \\ -6.432 & -1.812 & 0.223 & 4.387 \end{pmatrix}$$

$$X_2 = \begin{pmatrix} 52.29 & -43.30 & -1.824 & -0.867 \\ -43.30 & 73.88 & 0.45 & -0.098 \\ -1.824 & 0.45 & 1.226 & -0.034 \\ -0.868 & -0.098 & -0.034 & 0.379 \end{pmatrix}$$

$$Y_2 = \begin{pmatrix} 0.064 & 0.020 & 0.063 & 0.116 \\ 0.020 & 0.236 & 0.127 & -0.07 \\ 0.063 & 0.127 & 0.948 & 0.159 \\ 0.116 & -0.07 & 0.159 & 3.027 \end{pmatrix}$$

Step 2: P_1 and P_2 can be determined as,

$$P_1 = \begin{pmatrix} 0.056 & -0.113 & 1.011 & -1.65 & 0.001 & -0.01 \\ -0.106 & 0.327 & -1.803 & 4.586 & 0.019 & 0.013 \\ 1 & -1.9 & 23.465 & -28.39 & 0.316 & -0.643 \\ -1.565 & 4.6 & -27.24 & 67.7 & 0.483 & 0.137 \\ 0.001 & 0.017 & 0.322 & 0.468 & 0.443 & -0.056 \\ -0.01 & 0.014 & -0.644 & 0.146 & -0.056 & 0.276 \end{pmatrix}$$

$$p_2 = \begin{pmatrix} 52.3 & -43.3 & 26.05 & 17.76 & -1.82 & -0.867 \\ * & 73.9 & -46.87 & -17.67 & 0.45 & -0.098 \\ * & * & 32.46 & 9.97 & -0.62 & 0.298 \\ * & * & * & 10.25 & -0.48 & -0.229 \\ * & * & * & * & 1.23 & -0.034 \\ * & * & * & * & * & 0.379 \end{pmatrix}$$

Step 3: A pair of matrices Ξ_j, $(j = 1, 2)$ can be computed using (27),

$$\Xi_1 = \begin{pmatrix} 0.1426 & 0.3785 & -2.4882 & -0.9835 \\ -2.4403 & -1.9501 & 0.1644 & -3.2555 \\ -2.8200 & -0.9386 & 0.3997 & 0.2509 \\ 0.6080 & -1.5432 & -0.0404 & 0.7400 \end{pmatrix}$$

$$\Xi_2 = \begin{pmatrix} 0.8583 & -1.3772 & -0.4658 & -1.9299 \\ -0.7750 & -1.8917 & 2.3547 & -0.3850 \\ -1.8705 & 1.6675 & 0.7403 & -0.1986 \\ -1.2562 & -5.2979 & 0.7596 & 1.2599 \end{pmatrix}$$

which finally yield a pair of decentralised controllers $K_{jj}(s)$, $(j = 1, 2)$ as follows,

$$K_{11}(s) = \left(\begin{array}{cc|cc} -2.8200 & -0.9386 & 0.3997 & 0.2509 \\ 0.6080 & -1.5432 & -0.0404 & 0.7400 \\ \hline 0.1426 & 0.3785 & -2.4882 & -0.9835 \\ -2.4403 & -1.9501 & 0.1644 & -3.2555 \end{array}\right), \tag{57}$$

$$K_{22}(s) = \left(\begin{array}{cc|cc} -1.8705 & 1.6675 & 0.7403 & -0.1986 \\ -1.2562 & -5.2979 & 0.7596 & 1.2599 \\ \hline 0.8583 & -1.3772 & -0.4658 & -1.9299 \\ -0.7750 & -1.8917 & 2.3547 & -0.3850 \end{array}\right). \tag{58}$$

The poles of the closed-loop systems are shown in Fig. 2, which implies that all poles of the resulting closed-loop systems are located on the left-half plane and the system is stable.

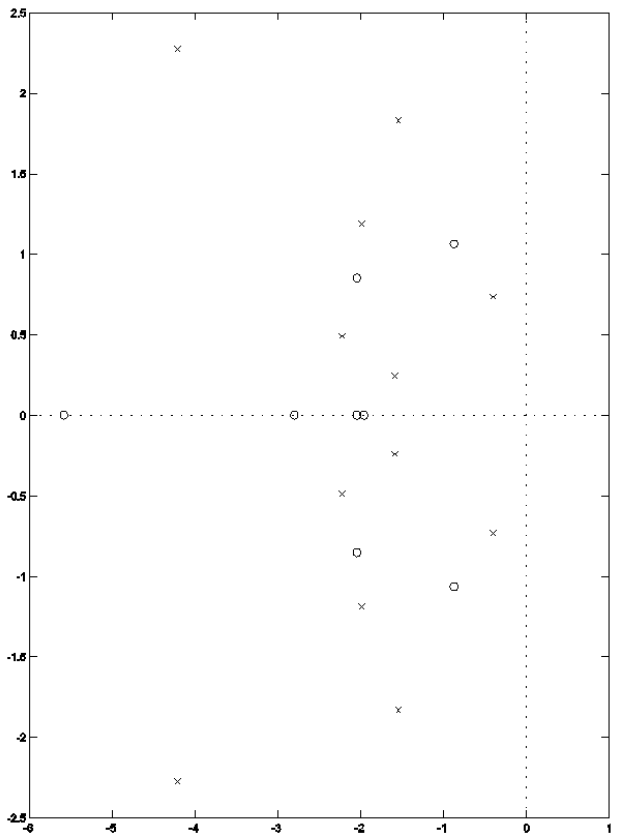

Figure 2. Poles of the closed-loop systems of Example 1

5.2 Example 2

Consider a mass-spring-friction system as shown in Fig. 3. Suppose that the linear motion concerned is in the horizontal direction with the reference directions of two displacements y_1 and y_2. The dynamical system can be represented as follows,

$$\begin{aligned} u_1(t) &= m_1 \frac{d^2 y_1(t)}{dt^2} + B_1 \frac{dy_1(t)}{dt} + k_1 y_1(t) + \\ & m_1 g + B_3 \frac{d(y_1 - y_2)(t)}{dt} \\ u_2(t) &= m_2 \frac{d^2 y_2(t)}{dt^2} + B_2 \frac{dy_2(t)}{dt} + k_2 y_2(t) + \\ & m_2 g - B_3 \frac{d(y_1 - y_2)(t)}{dt} \end{aligned} \tag{59}$$

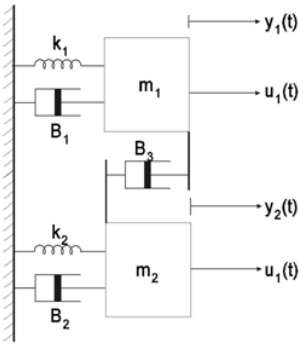

Figure 3. Mass-spring-friction system

For simplicity let $m_1 = 1\,\text{kg}$, $m_2 = 2\,\text{kg}$,

$k_1 = k_2 = B_1 = B_2 = B_3 = 1\,\text{N/m}$, then the transfer function matrix $G(s)$ between $Y(s) = \begin{bmatrix} Y_1(s) \\ Y_2(s) \end{bmatrix}$ and the control input $U(s) = \begin{bmatrix} U_1(s) \\ U_2(s) \end{bmatrix}$ is obtained to be,

$$Y(s) = \left(\begin{array}{c|c} \dfrac{2s^2+2s+1}{2s^4+6s^3+6s^2+4s+1} & \dfrac{s}{2s^4+6s^3+6s^2+4s+1} \\ \hline \dfrac{s}{2s^4+6s^3+6s^2+4s+1} & \dfrac{s^2+2s+1}{2s^4+6s^3+6s^2+4s+1} \end{array}\right) U(s) \tag{60}$$

We can consider this mass-spring-friction system as a two-block system with weak interaction; where $G_{11}(s)$ and $G_{22}(s)$ are the main blocks (here they are 1×1 systems), while $G_{12}(s)$ and $G_{21}(s)$ are cross coupling blocks. The state space realisations of these blocks are,

$$G_{11}(s) = \left(\begin{array}{cccc|c} -3 & -3 & -2 & -0.5 & 1 \\ 1 & 0 & 0 & 0 & 0 \\ 0 & 1 & 0 & 0 & 0 \\ 0 & 0 & 1 & 0 & 0 \\ \hline 0 & 1 & 1 & 0.5 & 0 \end{array}\right),$$

$$G_{22}(s) = \left(\begin{array}{cccc|c} -3 & -3 & -2 & -0.5 & 1 \\ 1 & 0 & 0 & 0 & 0 \\ 0 & 1 & 0 & 0 & 0 \\ 0 & 0 & 1 & 0 & 0 \\ \hline 0 & 0.5 & 1 & 0.5 & 0 \end{array}\right), \tag{61}$$

$$G_{12}(s) = G_{21}(s) = \left(\begin{array}{cccc|c} -3 & -3 & -2 & -0.5 & 1 \\ 1 & 0 & 0 & 0 & 0 \\ 0 & 1 & 0 & 0 & 0 \\ 0 & 0 & 1 & 0 & 0 \\ \hline 0 & 0 & 0.5 & 0 & 0 \end{array}\right)$$

In order to ensure good step responses, the weighting functions are chosen to emphasize the low frequency part;

$$W_1(s) = W_2(s) = \frac{s+1}{s+0.01}, \text{ and } \tilde{W}_1(s) = \tilde{W}_2(s) = 1$$

which implies equal weighting for the decoupling condition at all frequencies. The optimal decentralised controllers is found to be,

$$K(s) = \begin{pmatrix} \dfrac{f_1(s)}{g_1(s)} & 0 \\ 0 & \dfrac{f_1(s)}{g_2(s)} \end{pmatrix} \tag{62}$$

where

$$f_1(s) = -9.844s^5 + 2.684 \cdot 10^7 s^4 + 8.051 \cdot 10^7 s^3 + 8.051 \cdot 10^7 s^2 + 5.367 \cdot 10^7 s + 1.342 \cdot 10^7,$$

$$g_1(s) = s^5 + 4.202 \cdot 10^4 s^4 + 2.524 \cdot 10^7 s^3 + 2.576 \cdot 10^7 s^2 + 1.375 \cdot 10^7 s + 1.342 \cdot 10^5,$$

$$f_2(s) = -4.955s^5 + 7.883 \cdot 10^6 s^4 + 2.365 \cdot 10^7 s^3 + 2.365 \cdot 10^7 s^2 + 1.577 \cdot 10^7 s + 3.942 \cdot 10^6,$$

$$g_2(s) = s^5 + 9661s^4 + 3.539 \cdot 10^6 s^3 + 7.389 \cdot 10^6 s^2 + 4.042 \cdot 10^6 s + 3.956 \cdot 10^4.$$

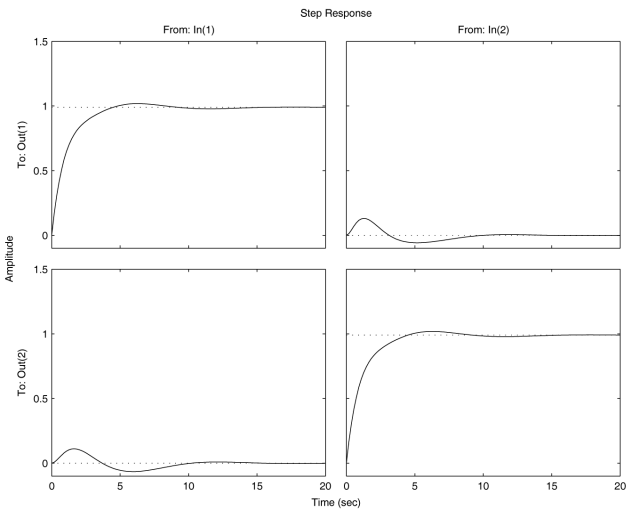

Figure 4. Step responses of mass-spring-friction system

5.3 Example 3

The composite model (engine+actuator) of this twin-spool jet engine has 21 states, three inputs and three outputs. The inputs are the Fuel Flow (FF), the Inlet Guide Vanes (IGVs) and the Nozzle Area (NA), and the outputs are the Low Pressure Spool speed (NL), the High Pressure Spool Speed (NH) and the Surge Margin (SM). The schematic of the engine is shown in Fig. 5.

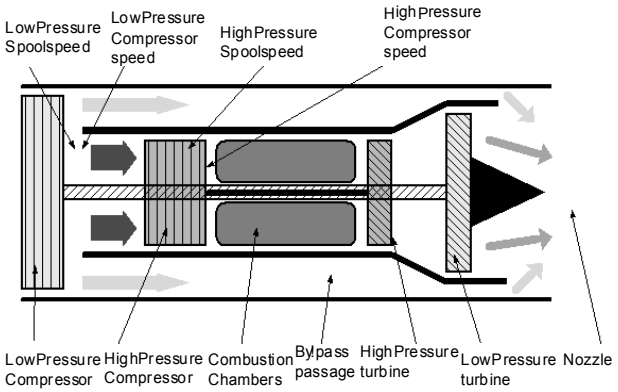

Figure 5. The schematics of the twin-spool get engine

All the inputs and output variables are normalised based on their operating points. The method outlined in [35] is used to pair the inputs and outputs. Subsequently, W is computed as follows,

$$W = \begin{array}{c} \begin{matrix} NA & FF & IGV \end{matrix} \\ \begin{bmatrix} 9.1226 & 0.39616 & 0.0057 \\ 0.4002 & 0.1282 & 0.0248 \\ 1.5014 & 0.8043 & 0.2622 \end{bmatrix} \end{array} \begin{matrix} SM \\ NL \\ NH \end{matrix} \qquad (63)$$

The optimal input and output permutations are $\{3,1,2\}$ and $\{3,1,2\}$ respectively [35]. This yields the following decomposition structure,

$$\overline{W} = \begin{array}{c} \begin{matrix} FF & IGVs & NA \end{matrix} \\ \begin{bmatrix} 0.1282 & 0.024772 & 0 \\ 0.80433 & 0.26216 & 0 \\ 0 & 0 & 9.1226 \end{bmatrix} \end{array} \begin{matrix} NL \\ NH \\ SM \end{matrix} , \qquad (64)$$

$$V = \begin{array}{c} \begin{matrix} NA & FF & IGV \end{matrix} \\ \begin{bmatrix} 0 & & 0.40023 \\ 0 & 0 & 1.5014 \\ 0.39616 & 0.0057099 & 0 \end{bmatrix} \end{array} \begin{matrix} NL \\ NH \\ SM \end{matrix} \qquad (65)$$

This suggests that the system can be decomposed into a 2×2 and a 1×1 subsystem. The decomposition also agrees with engineering intuition. The two compressors are strongly coupled because although the low pressure compressor can bleed compressed air through the bypass, the high pressure one has to be fed by the low pressure compressor. This implies that the two compressors make a strongly coupled 2×2 system. On the other hand, Surge margin is heavily dependant on the air pressure inside the engine which is greatly affected by the open nozzle area. The resulting controls system structure is shown in Fig. 6 and 7. The weighting functions for the design of $K_{11}(s)$ and $K_{22}(s)$ were determined as follows,

$$W_{11}(s) = 0.65\frac{s+1}{s+0.001} I^{2\times 2} \qquad (66)$$

$$W_{22}(s) = 0.97\frac{s+3}{s+0.007} \qquad (67)$$

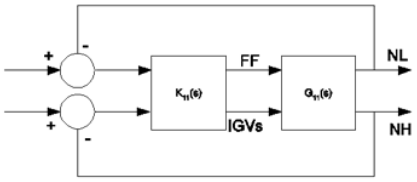

Figure 6. Compressor control systems

Figure 7. Surge margin control system

The open loop responses of the engine are shown in Fig. 8 while Fig. 9 shows the response of the compressor pair subsystem, which shows that the interactions have been reduced considerably and the overshoot is also within satisfactory limits. Fig. 10 shows the response of the Surge margin loop, where it is observed that the overshoot is very small. This was achieved by a setting the gain of $W_{22}(s)$ close to 1 because an overshoot in the surge loop could lead to fatal damage to the engine (due to the air direction reversing and pulsating in the engine). Fig. 11 shows the response of the overall closed loop system with the decentralised controller.

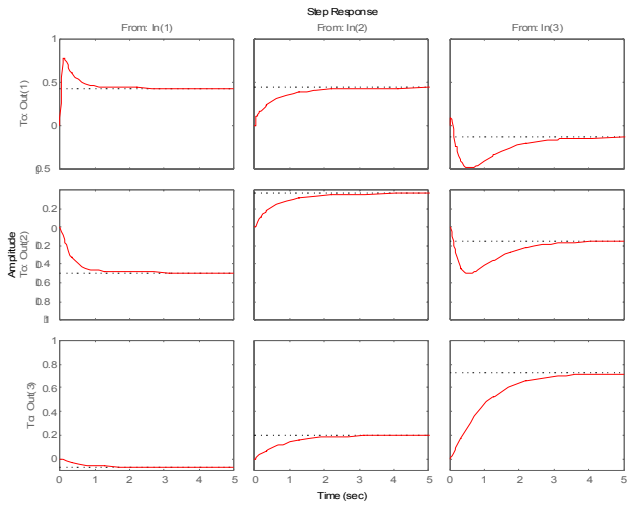

Figure 8. Open loop responses of the engine

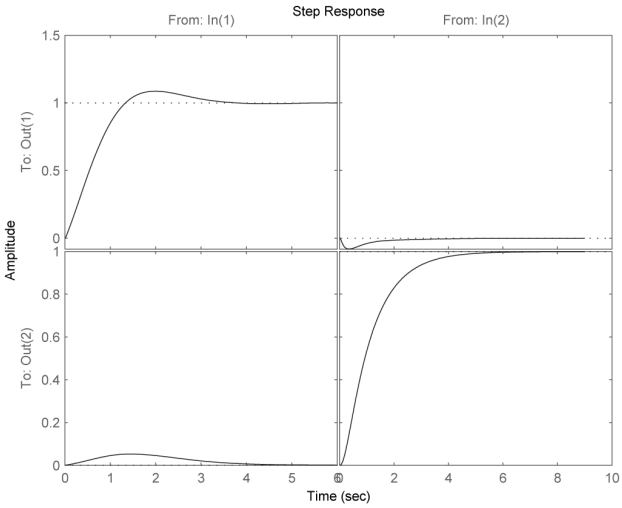

Figure 9. Closed loop response of the compressor pair

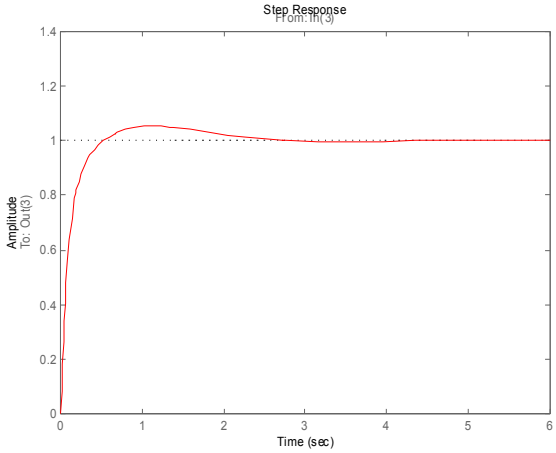

Figure 10. Surge margin response

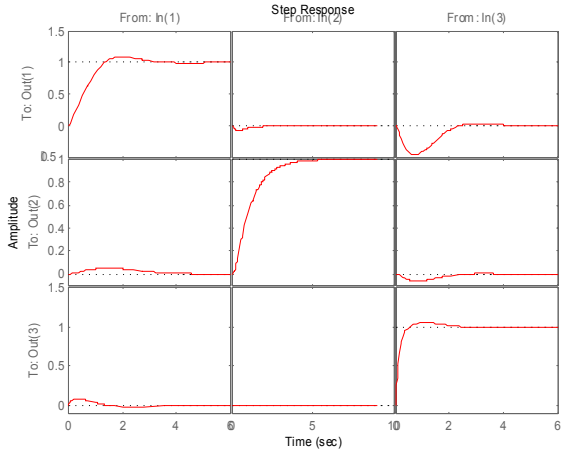

Figure 11. Closed loop response of the overall system

6. CONCLUSIONS

This paper proposed a decentralised controller design procedure for weakly coupled systems. A key feature of the design method is that the problem of designing a complete decentralised controller is replaced by several simpler local design problems. This is the key feature of this approach and is achieved by introducing a decomposition condition, which imposes local design constrains. This means that the design of each $K_{jj}(s)$ controller is completely decoupled from other controller. This has both design, and computational benefits. For the design, as long as each local controller satisfies the local decomposition condition, its design will be independent of the other controllers. In turn, this facilitates the various design stages such as the choice of weighting functions. This is because normally the entire weighting function matrix has to be determined at once, but here it may be determined element by element. In other approaches where the decentralised controller is designed as a single multivariate controller (see for example [37]), if the responses are not satisfactory, it is difficult to know how and which weighting function have to be modified. In the proposed technique however, since each sub-system has its own associated weighting functions, it is straight forward to adjust the weighting functions of the concerned subsystem. In this sense each of the loop-controllers is locally tunable.

Naturally, the decomposition conditions will introduce some levels of conservatism, nonetheless the advantages are that the decomposition condition and the H_∞ design criteria are combined into a single LMI optimisation which yields local controllers that only use local actuators and sensor information. The formulation can also deal with additive uncertainty, as this can be absorbed into the term Δ_j and then be factorised out similar to (13). Therefore the same produce can be used to include this type of system uncertainty. The derivation is a straightforward extension and is thus omitted here for clarity.

ACKNOWLEDGMENT

This work is supported by Hong Kong CERG Grant No. CityU122305/9041041 (1225) and City University of Hong Kong. The authors would like to thank Mr. W. K. Yang for his contributions in this work, and the Engineering and Physical Sciences Research Council (EPSRC) in the UK for supporting this research (grant number GR/S91741/01).

REFERENCES

[1] J. Lunze, “Feedback Control of Large-scale Systems”, Prentice-Hall, 1992, ISBN: 013318353X.

[2] D. D. Siljak, “Decentralized Control of Complex Systems”, Academic Press, Boston, 1991, ISBN: 0126434301.

[3] D. D. Siljak, “Large-Scale Dynamic Systems: Stability and Structure”, North-Holland, New York, 1978, ISBN: 044400264.

[4] S. P. Boyd, L. El Ghaoui, E. Feron, V. Balakrishnam, “Linear Matrix Inequalities in System and Control Theory”, Vol. 15. Philadelphia, PA: SIAM, 1994, ISBN: 089871334X.

[5] Y. Nesterov, A. Nemirovsky, “Interior Point Polynomial Methods in Convex Programming”, Vol. 13. Philadelphia, PA: SIAM, 1994, ISBN: 0898713196.

[6] G. F. Bryant, L. F. Yeung, "Multivariable Control System Design Techniques: Dominance and Direct Methods", Jon Wiley & Sons, 1996, ISBN: 0471958662.

[7] L. F. Yeung, G. F. Bryant, "New dominance concepts for multivariable control systems design", Int. J. Control, Vol. 44, No. 4, 1992, pp. 969-988.

[8] M. Chilali, P. Gahinet, "H_∞ design with pole placement constraints: an LMI approach", IEEE Transactions on Automatic Control, Vol. 41, 1996, pp. 358-367.

[9] P. Gahinet, A. Nemirovski, A. J. Laub, M. Chilali, LMI Control Toolbox, The Math Works Inc., 1995.

[10] M. Ikeda, "Decentralized control of large-scale systems, Three Decades of Mathematical System Theory", Springer-Verlag, New York, 1989, ISBN: 0387516050.

[11] M. Ikeda, G. Zhai, Y. Fujisaki, "Decentralized H_∞ controller design for large-scale systems: A matrix inequality approach using a homotopy method", Proc. 35th IEEE CDC, Kobe, Japan, Vol. 9, 1996, pp. 1-6.

[12] T. Iwasaki, R. E. Skelton, ``All controllers for the general H_∞ control problem: LMI existence conditions and state space formulas", Automatica, Vol. 30, 1994, pp. 1307-1317.

[13] H. Kimura, "Chain-Scattering Approach to H_∞-Control", Birkhauser, 1996, ISBN: 0817637877.

[14] M. Green, D. N. Limbeer, "Linear Robust Control", Prentice Hall, Englewood Cliffs, New Jersey, 1995, ISBN: 0131022784.

[15] A. Packard, K. Zhou, P. Pandey, G. Becker, "A collection of robust control problems leading to LMIs", Proc. 30th IEEE CDC, Brighton, UK, 1991, pp. 1245-1250.

[16] S. Richter, R. DeCarlo, "A homotopy method for eigenvalue assignment using decentralized state feedback", IEEE Transactions on Automatic Control, Vol. 29, 1984, pp. 148-158.

[17] H. H. Rosenbrock, "Computer Aided Control System Design", Academic Press, London, 1974, ISBN: 0125974507.

[18] A. Weinmann, "Uncertain Models and Robust Control", Springer-Verlag/Wien, New York, 1991, ISBN: 9783211822999.

[19] G. Zhai, M. Ikeda, "Decentralized H_∞ control of large-scale systems via output feedback", Proc. 32nd IEEE CDC, 1993, pp. 1652-1653.

[20] L. F. Yeung, G. F. Bryant, "Robust stability of diagonally dominant systems", IEE Proc., Part D, Vol. 131, No. 6, November 1984, pp. 253-260.

[21] P. Grosdidier, M. Morari, "Interaction measures for systems under decentralized control", Automatica, Vol. 22, No. 3, 1986, pp. 309-319.

[22] E. H. Bristol, "On a new measure of interaction for multivariable process control", IEEE Transactions on Automatic Control, Vol. 11, 1966, pp. 133-134.

[23] G. F. Bryant, L. F. Yeung, "Multivariable control system design techniques: dominance and direct methods", John Wiley and Sons, 1996, ISBN: 0471958662.

[24] G. F. Bryant, L. F. Yeung, "Method and concepts of dominance optimization", IEE Proceedings of Control Theory and Application, Part D, Vol. 130, No. 2, 1983.

[25] A. Conley, M. E. Salgado, "Gramian based interaction measure", In IEEE CDC, 2000, Vol. 5, pp. 5020-5026.

[26] E. Gagnon, A. Desbiens, A. Pomerleau, "Selection of pairing and constrained robust decentralized PI controllers", In Proceedings of the American Control Conference, Vol. 6, 1999, pp. 4343-4347.

[27] J. G. Michaels, K. H. Rosen, "Applications of discrete mathematics", McGraw-Hill International Editions, 1991, ISBN: 0070418233.

[28] N. Munro, "Multivariable design using the inverse Nyquist array", Computer Aided Design, Vol. 4, No. 4, 1972, pp. 222-227.

[29] H. H. Rosenbrock, "State space and multivariable theory", Nelson, London, ISBN: 0177810025.

[30] M. F. Witcher, T. J. McAvoy, "Interacting control systems: Steady-state dynamic measurement of interaction", ISA Transactions, Vol. 16, No. 3, 1977, pp. 35-41.

[31] L. F. Yeung, "Optimal input-output variable assignment for multivariable systems", Automatica, Vol. 27, No. 4, 1991, pp. 733-738.

[32] M. Zhang, "Optimal input/output structure selection for multivariable control system", MPhil thesis, City University of Hong Kong, 2000.

[33] M. Zhang, L. F. Yeung, "Optimization algorithm for input/output structure selection of large multivariable control systems", IFAC Workshop on Algorithms and Architecture for Real-time Control, 2000.

[34] Z. X. Zhu, "Variable pairing selection based on individual and overall interaction measure", Industrial Engineering in Chemical Research, Vol. 35, 1996, pp. 4091-4099.

[35] L. F. Yeung, K. Y. Chan, A. Wu, "Experimental Design Theoretic Genetic Algorithm for Input-Output Block Assignment Problem", Proc. of the 40th IEEE CDC, Orlando, Florida, USA, December 2001, pp. 4049-4050.

[36] S. A. Forshaw, "The Rolls-Royce Spey Gas-Turbine Engine: A Multivariable Case Study", Masters thesis, UMIST, 1978.

[37] J. Bao, J. F. Forbes, P. J. McLellan, "Robust Multiloop PID Controller Design: A Successive Semidefinite Programming Approach", Ind. Eng. Chem. Res. Vol. 38, 1999, pp. 3407-3419.

[38] J. M. Maciejowski, "Multivariable feedback design", Addison Wesley, 1989, ISBN: 0201182432.

[39] Sigurd Skogestad, Ian Postlethwaite, "Multivariable feedback control", Wiley, 2001, ISBN: 047194277.

Biographies

L. F. Yeung received the BSc in Electronic and Electrical Engineering from Portsmouth University, UK in 1978; and Ph.D. in Control Engineering from Imperial College of Science and Technology and Medicine in 1990. From 1978 to 1979, he was a Medical Physicist in the ENT Centre, North Riding Infirmary, UK. From 1979 to 1986, he jointed the Industrial Automation Group, Department of Computing and Control,

Imperial College as a Research Engineer, and then from 1986 to 1990 he worked with the Industrial System Group, Centre for Process Systems Engineering, Department of Electrical Engineering, Imperial College, and then Research Fellow in 1990. He joined the Department of Electronic Engineering, City University of Hong Kong in 1992; he is now Associate Professor and Director of the Automatic Control and Power Electronics laboratory, Director of the Underwater System Laboratory, member of the Hoi Ha Wan Marine Park Management Committee and Laboratory. He is now the convenor of the IET Pearl River Delta Development Committee He was also awarded the IEE Heaviside Prize for his paper in 1983 on dominance optimisations.

Gouping Lu received the B.S. degree from the Department of Applied Mathematics, Chengdu University of Science and Technology, China, in 1984, and the M.S. and Ph.D. degrees from the Department of Mathematics, East China Normal University, China, in 1989 and 1998, respectively. He is currently a Professor at the College of Electrical Engineering, Nantong University, Jiangsu, China. His current research interests include nonlinear control, robust control and networked control.

Amin Nobakhti was born in Tehran, Iran. He received his B.Eng in Electrical and Electronics Engineering from University College London (UCL) in 2000. He subsequently obtained M.Sc and Ph.D. degrees in advanced control systems from the University of Manchester Institute of Science and Technology (UMIST) under the supervision of the late Professor Neil Munro in multivariable control systems in 2001 and 2004 respectively. Since 2004 he has been a Research Associate at the University of Manchester, Control Systems Centre working on multivariable system design. He has recently completed one year industrial secondment with Sappi Fine Paper Europe, Blackburn mill, under an EPSRC Research Associate Industrial Secondment scheme (RAIS).

Daniel W. C. Ho received a first class B.Sc., M.Sc. and Ph.D. degrees in mathematics from the University of Salford (UK) in 1980, 1982 and 1986, respectively. From 1985 to 1988, he was a Research Fellow in Industrial Control Unit, University of Strathclyde (Glasgow, Scotland). In 1989, he joined the Department of Mathematics, City University of Hong Kong, where he is currently a Professor. He is an Associate Editor of Asian Journal of Control and a senior member of IEEE. His research interests include H-infinity control theory, nonlinear control theory, estimation and filtering theory and complex network.

Hong Wang received the BSc, MEng and Ph.D. degrees from Huainan University of Mining Engineering (AHUST) and Huazhong University of Science and Technology (HUST) in P. R. China 1982, 1984 and 1987, respectively. He then worked as a postdoc at Salford, Brunel and Southampton Universities between 1988 and 1992. He joined UMIST in 1992. Professor Wang received the outstanding overseas scholarship award from the Chinese NSF in 2002, and outstanding overseas academics award from the Chinese Academy of Sciences in 2004. Professor Wang is a Fellow of IET and InstMC, he is the editorial board member for seven international journals and member of three IFAC Technical Cttees.

Table of Contents

Volume 5 / Number 1 / 2009

INSTRUCTIONS FOR AUTHORS (Title is Helvetica size 18)

Author 1[a,*], Author 2[b], Author 3[c] (Helvetica size 12)

[a]Affiliation a (Helvetica size 10)

[b]Affiliation b (Helvetica size 10)

[c]Affiliation c (Helvetica size 10)

ABSTRACT (Times New Roman size 12)

An abstract, not exceeding 200 words, is required for all papers (font is Times New Roman size 9).

Keywords (Times New Roman size 12)

The author should provide a list of key words, up to a maximum of six (font is Times New Roman size 9).

1. INTRODUCTION (Times New Roman size 12)

(Body text is Times New Roman size 9). The introduction of the paper should explain the nature of the problem, previous work, purpose, and the contribution of the paper. It is assigned the number "1" and following sections are assigned numbers as needed. format. The paper must be (Letter) page size with margins of 1.25" for the top of first page, 0.75" for left, right, and bottom, and 0.75" for top, bottom, left, and right of ALL subsequent pages. The paper must be double column format, single line spacing with an extra line added between paragraphs. Please limit the title to a maximum length of 10 words. The author's name(s) follows and is also centered on the page. A blank line is required between the title and the author's name(s). Last names should be spelled out in full and preceded by author's initials. The author's affiliation, complete mailing address, and e-mail address are provided below. Phone and fax numbers do not appear. Do not underline any of the headings, or add dashes, colons, etc. The headings, starting with "1. INTRODUCTION", appear in upper case letters and should be set in bold and aligned flush left. All headings from the Introduction to Conclusions are numbered sequentially using 1, 2, 3, etc. Subheadings are numbered 1.1, 1.2, etc. If a subsection must be further divided, the numbers 1.1.1, 1.1.2, etc. are used and the number and associated title are set in italics instead of bolded. A colon is inserted before an equation is presented, but there is no punctuation following the equation. All equations are numbered and referred to in the text solely by a number enclosed in a round bracket (i.e. (2) reads as "equation 2"). Ensure that any miscellaneous numbering system you use in your paper cannot be confused with a reference [3] or an equation (2) designation.

*Corresponding author: *E-mail:*

For more details, please visit

www.medjmc.com

1.1 Initial Submission

The manuscript must be a single file (including tables, figures, etc.) using either an Adobe-compatible portable document format (*.pdf) or an MS Word (*.doc) or Adobe FrameMaker (*.fm). Submit the manuscript without the authors' names, affiliation, and biographies. Along with it, submit a cover page that includes the manuscript title, authors' names and affiliation, and the corresponding author's name and contact information (full postal and e-mail addresses, phone and fax numbers), and biographies. The corresponding author will be given a reference number assigned to the paper and it is to be used in all future correspondence. Formatting your paper correctly saves a great deal of editing time, which in turn ensures publication of papers in a timely manner. Authors submit electronic versions of their manuscript to:

isubmission@medjmc.com

1.1.1 Figures

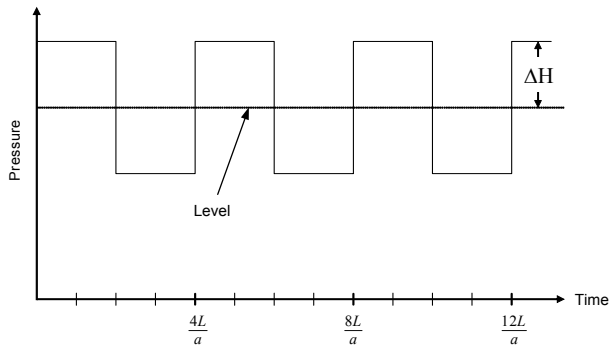

Figure 1. Sample graph

A reference list must be included. Only cited text references are included. Each reference is referred to in the text by a number enclosed in a square bracket (i.e., [3]). References must be numbered and ordered according to where they are first mentioned in the paper, not alphabetically.

REFERENCES

[1] Anderson, B. O. D. and D. J. Clements, "Algebraic Characterization", Vol. 17, 1981, pp. 703-712.

The Mediterranean Journal of Measurement and Control
www.medjmc.com

Published by SoftMotor Ltd. ISSN: 1743-9310

For complete information regarding
subscription and ordering,
please contact

SoftMotor Ltd
Provincial House, Solly Street, Sheffield S1 4BA
United Kingdom

Tel: (+44) 0114 201 4916
Fax: (+44) 0114 201 3524
E-mail: order@medjmc.com
Website: www.medjmc.com
Website: www.softmotor.co.uk

Volume 5 / Number 1 / 2009